Modelling slab age and crustal thickness: numerical approaches to drivers of compressive stresses in the overriding plate in Andean style subduction zone systems.

WITHERS, CRAIG

Modelling slab age and crustal thickness: numerical approaches to drivers of compressive stresses in the overriding plate in Andean style subduction zone systems.

Craig Withers

Department of Earth Sciences

A thesis submitted for the degree of:
Master of Science (MScR)
June 2020

Table of Contents

Abstract

The Andes Mountains are formed at a destructive plate margin, where dense oceanic crust descends beneath relatively buoyant continental crust. There are regions of the Andes where the range is narrow, but there is also the high plateau of the Central Andes. The reasons for this variation in structure of the overriding plate are not clear. Previous numerical modelling shows that slabs typically roll back, so that continents are stretched, causing tension and potentially back-arc extension. This model does not fit the Andes. Instead, the formation of a thick crust and sustained elevation of the Andes has been hypothesized to be due to a range of different processes, including anchoring of the slab in the lower mantle, subduction of buoyant features in the Nazca plate, or compression driven by large-scale convection cells underneath South America. The enigmatic formation of the Andes is the central theme of this thesis.

Previous research suggests a clear correlation between slab age and overriding plate crustal thickness, globally, but in particular for South America. In this project, we hypothesize that this age variation plays a significant role in the formation of the Andes. As subducting slabs descend into the mantle, their properties differ in conjunction with their age affecting their buoyancy and strength, thereby generating different dynamics, surface tectonics, and slab morphologies. Using numerical modelling code ASPECT, we examined the role of slab properties and related dynamics on the state of stress in the overriding plate.

We quantify how much compression occurs in the overriding plate, and use this as a proxy for topographic growth. Typically, older slabs cause more rollback and therefore extension. The models in this study however, predict that the stronger pull force from older slabs causes more vigorous subduction, in which mantle convection contributes to corner flow in the mantle wedge, thereby increasing compression.

An increase in overriding plate thickness from 50 to 100km increases its overall density and therefore the amount of compression in the overriding plate by 10 MPa, while an increase in slab age from 40 to 80 Myr generates a similar increase in compression. Finally, slab morphology affects the geometry and vigour of convection cells beneath the overriding plate, which, in turn, affects the compressional state of the plate. This is affected by variation of parameters such as mantle viscosity and changes to frictional coupling, which is in qualitative agreement with previous work.

In summary, our modelling shows that varying slab age is a viable mechanism for producing significant compression in the overriding plate, consistent with the positive correlation between slab age and crustal thickness of the Central Andes.

Declaration.

I, Craig Withers, declare that this thesis, presented for the degree of Master of Science at Durham University, is a result of my own original research and has not been previously submitted to Durham University or any other institution.

I have clearly indicated, when appropriate, the contributions of colleagues and have made every effort to acknowledge all collaborative work.

Craig Withers
Durham University

June 2020

Acknowledgements.

First and foremost, for his patience and incredible guidance, my sincere thanks to Jeroen van Hunen. Without him this study and the advancement of my academic, professional and personal life would be nowhere near what it may now amount to be. Also, for having some quite incredible patience for someone who – at times – felt as if they were totally lost. Thank you Jeroen.

Second, and no less importantly for his influence in shaping this study and his incredible knowledge of this planet which swayed me into taking up this project, my sincere thanks to Mark Allen. Thanks for always having time for me hassling you and for hinting at suitable PhDs for the future. I cannot underestimate the influence these two had. Thank you both very much.

Major thanks to Gerald Roberts, who without having faith in my abilities I may not have chosen to pursue further study. Thanks Gerald. Also to Steve Hirons of Birkbeck who provided a great reference which helped get me into Durham.

Thanks to everyone I met in the department who made my life moving miles away from Brighton much more enjoyable. Special mention to Nico Schliffke for getting me out of many a jam with coding, same goes for CJ. Also, big thanks to frankly the nicest man in the office if not the world, Phil Heron. I still owe you lunch from my first week.

Huge thanks to Dimitirios and Josh from the department, as well as Aksel who I played in a band with. I won't mention the name of the band, but thanks for keeping me sane with all that.

Massive thanks to Jake Brooker, with whom I had the pleasure to play at several gigs and open mic nights hosted by the wonderful Jim Cockerill with. I will miss you both dearly. And Diane for coming to watch too! To all the MScR students that started at (roughly) the same time as me. You know who you are. Special mention to Jenny and Annabelle for being great desk neighbours.

Everyone who played alongside me for Ustinov AFC. I still can't believe we didn't get promoted this season. Hopefully get to play with you all sometime soon. Maybe not Jimmy.

All my friends that actually bothered visiting. It's a long way so thanks to those that made the trek. Also, to Rebecca Kirkbride for always having faith in me. All that you did is still on my mind. Thanks.

Thanks to Luke, Max, Mel and Matt who I currently live with. You helped lots when I was writing this up. Also to Lauren Hands, who was a wonderful person and friend to live with during my time in Durham.

Without the support of my Mum and Dad none of this would have ever been possible. Thanks for helping me do all this. I'll pay you back what I owe eventually. Also, thanks to my siblings Polly, Imogen and Leo. None of you have any idea what I do, but thanks for being around nonetheless.

Thanks also to Christina for being so supportive during this time. Good luck in whatever you do next.

Dedicated to my dear friend Paddy Charleton.

I hope you're still resting in peace. I thought you might like to have your name on something.

Chapter 1. Introduction

The Andean subduction margin is regularly debated in terms of its origin, initiation and its complex growth history; among many other features. It remains one of the few places on Earth to have developed an orogenic plateau during ongoing subduction zone processes, rather than during continent - continent collision. The oceanic Nazca plate subducts beneath the continental South American plate, producing the ~9000 km long Peru-Chile trench. This has been occurring in the region for more than 200 Myr (Scott 2018).

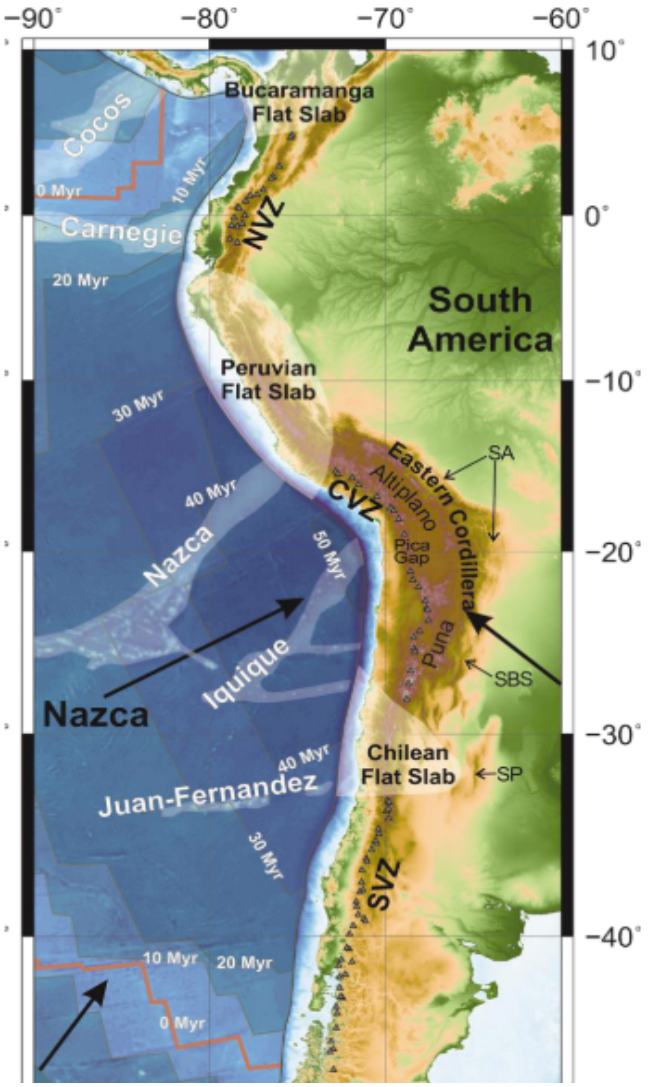

Fig. 1.1. Topographic/bathymetric overview of the Andean subduction system. Includes oceanic plate ages upon entering the trench, names of ridges and black arrows to indicate plate velocities. 3 locations of flat slab subduction regions are highlighted, with triangles to indicate active quarternary arc volcanoes in the northern, central and southern volcanic zones (NVZ,CVZ and SVZ). Includes the Sierras Pampeanas (SP), Santa Barbera System (SBS) and Sub-Andean fold and thrust belt (SA) regions of the Tectonic plateau. Black arrows represent absolute plate velocities (rate and direction), as in Sdrolius and Müller (2006). From Scott (2018).

Old cratons – large thick regions of lithosphere that have roots reaching into the asthenosphere and make up the oldest of Earth's continents – were thought to have joined as part of the ancient supercontinent Gondwana during the Neo-Proterozoic from several stages of plate reorganisation. Subsequent collisions such as between Laurentia and Gondwana forming the Pampean orogeny (Weinberg et al. 2018) in the Cambrian further reorganised the basement terranes at the western edge of Gondwana up until the Jurassic, which is thought to be where Gondwana broke apart and subduction began at its western perimeter (Scott 2018).

Initially part of the Farallon plate which now resides beneath North America, the Nazca plate is relatively young at < 60 Myr today (Scott 2018, Chen et al. 2019). Subduction beneath South America has occurred since the Jurassic, but

Nazca plate subduction independent from the Farallon plate started at different estimates. Some estimate the break off from the Farallon plate to have been at ~80 Ma (Chen et al. 2019), while other studies consider it to be later in the Cretaceous period or even as recently as 23 Ma (Scott 2018, Espurt et al. 2008).

The early Cretaceous period (~140 Ma) marked the period of spreading in the South Atlantic, creating South America's current morphology and separation from the African continent. As the South American plate moved west under influences of continued spreading in both the Atlantic and Pacific Ocean from slab roll back and mantle convection, the subduction margin was interpreted to be in a stage of generating extension in the overriding plate.

It is thought that an extensional phase of deformation style at the Andean margin continued until compressive stresses in the overriding plate (OP) are thought to have begun between 50 – 70 Ma at the earliest, at which point the Andes began to form (Scott 2018). This has been compiled using paleao-elevation datasets indicating the onset of shortening creating this recent stage of uplift (Scott et al. 2018). Studies conducted around the structures of the Neuquén Basin – which lies between 32 - 42˚S in central Argentina, bordering Chile to the west - and tomographic profiling suggest a complex growth history between extension, compression and neutral conditions since subduction initiation (Horton 2018, Chen et al. 2019). The basin exhibits extended periods of extension for most of the Western edge of South America during the Mesozoic, with anomalous periods of regional shortening and mixed-mode deformation during the early Cretaceous and Paleogene. Both of these periods show upper crustal fold thrust deformation, foreland basin formation and regional flexure (Horton 2018). It is also suggested that significant shortening occurred during the Neogene (Allmendinger et al. 1997).

Subduction of young slabs and flat slab morphologies are said to induce compressive stresses, with neutral conditions at the margin thought to be controlled by a slab dip somewhere between these two (Turcotte and Schubert 2014). Given the current slab age distribution of the Nazca plate (Fig. 1.1), a plateau forming over the last ~50 Myr would be unlikely if following previous models (Turcotte and Schubert 2014), despite recent geochemical evidence suggesting the Andes are currently in a stage of compressive stress and uplift (Scott et al. 2018). Slab age at the trench is thought to have been younger than 80 Myr over the last 50 Myr, while also remaining in roughly the same configuration of younging to both the south and north from the central Andes over the same time period (Scott et al. 2018).

There are 3 distinct regions of active volcanism in the Andes, known as the northern, central and southern volcanic zones (Fig. 1.1). Beneath the active arc segments, slabs descend beneath the OP at ~30˚slab dip angle. This allows for hydrous minerals and volatile rich oceanic crust to melt mantle rocks, creating magma that forms the volcanoes. This melting takes place in the mantle wedge, which is the triangular shaped region beneath the OP and above the slab closest to the trench.

In most of Peru and at ~30˚ south, there are no volcanoes present. This is in part due to flat slab subduction geometry created by the thicker – and therefore more buoyant - oceanic crust, which covers these sections of the oceanic plate, such as at the Nazca and Juan-Fernandez ridges (Espurt et al. 2008, Scott 2018). This morphology allows for reduced melting of mantle rocks, and so no volcanoes are present here (Fig. 1.1).

In the central Andes, a region of thickened crust is developed and is split into 3 distinct units. The Western Cordillera includes active volcanoes in the central volcanic zone (CVZ) (Fig. 1.1) forming the western margin, while a high and wide plateau forms the central topographic high. This plateau region reaches over 4 km from sea-level and is divided into the Altiplano and Puna, respectively. The plateau is then joined by narrow ranges to both the north and south.

Further east into the South American Plate, the Eastern Cordillera makes up the eastern margin of the central Andes. Both of the cordillera makes up the drainage divide for the plateau, composed of the morphologically separate Puna and Altiplano sections. These regions of continental crust may reach over 70 km thickness in the CVZ (Tassara and Echaurren 2012, Scott 2018), which is considerably thicker than any other crust formed at an oceanic - continental plate boundary. Only crust formed in continental collision settings such as the Himalayas would we expect to see a crust of similar thickness.

Crustal generation in the underlying subduction zone would, on its own, be insufficient to build a high and wide plateau like the Central Andes (Sobolev and Babeyko 2005, Allmendinger et al. 1997). Large-scale delamination of the lower continental crust from a gabbroic to eclogitic phase when in contact with a convecting mantle has been suggested as additional component to uplift the remaining buoyant crustal material, via isostasy (DeCelles 2009). But in order to avoid gravitational collapse, compression across the entire Andes is needed, and associated shortening could provide additional crustal thickness. This means westward motion of the OP, heading towards the trench inducing compressive stresses. Mantle melting in conjunction with this shortening of lithosphere is thought to generate

around 70 - 80% of the crustal volume in the central Andes (Allmendinger et al. 1997, Sobolev and Babeyko 2005).

The tectonic configuration seen in the modern Andes is rare in current continents, as most other major plateaus have been formed by continental collision. The western USA may contain the relics of another orogenic plateau formed without continental collision – known as the "Nevadaplano" – which is being dissected at present in Utah and Nevada (Scott 2018). Mexico may be a third example in the Americas of a similar plateau formed from subduction (Espurt et al. 2008), but east Asia and SE Asia lack such features at present. This leaves the question: why is the central Andes so unusual, and what are the dynamics driving the sustaining of such a plateau?

The Central Andes mark the same region as the Atacama Desert, which contains an area of reduced rainfall and sedimentation. This has been established as causing more coupling at this region of the Andes (Lamb and Davis 2003) and possibly being responsible for onset of shortening. However, this current climatic period is predated by the shortening events recorded in the Neuquén Basin studies (Horton 2018).

One feature that appears to align with the thickened crust in the Central Andes, is the age of the subducting slab. Current slab age at the trench around the thickest part of the crust at the Bolivian Orocline (~20˚ south) is the oldest at the margin with younging seen to both the north and south (~ 50 Myr, Fig. 1.1). Slab age has also been reasonably consistent, with ages younger than 80 Myr over the same 50 – 60 Myr period of shortening and uplift (Scott et al. 2018). This suggests that there may be a causal relationship between slab age and crustal thickness, which asks the question: do older subducting slabs at the trench lead to thicker continental crust? The current slab age arrangement and the suspected onset of tectonic shortening with the development of the Altiplano/Puna plateau, suggests that this may be the case.

This thesis uses numerical modelling to understand the effects and interactions between important parameters at subduction zones such as slab age, mantle viscosity and plate coupling. The emphasis is on understanding what increases compressional stress in the overriding plate, as this is argued to be necessary to produce crustal shortening, thickening, and hence growth of a plateau like the Central Andes.

The rest of this chapter reviews the relevant aspects of the mantle, properties of the subducting slab, and summarises the character of the overriding plate. A short section regarding subduction zone processes will then be detailed, with the chapter finishing on a statement of the hypotheses and aims of this thesis, then outlining of the remaining chapters.

1.1 Mantle conditions

Earth's mantle is composed of layers increasing with temperature together with depth, which also exhibit different viscosities (section 2.4.2). Solid lithosphere resides above asthenosphere, as part of the low viscosity upper mantle, in which temperatures are at variable estimates between 1300˚C and 1500˚C (Goes et al. 2017).

There are clear seismic velocity changes at 410 km, 520 km and 660 km depth within the upper mantle, indicating density contrasts as well as an inferred viscosity jump. This region of the upper mantle marks what is known as a mantle transition zone (MTZ). At its base is the solid-solid phase transition from ringwoodite (a high-pressure phase of olivine) to bridgmanite and periclase. Its exact depth depends on the temperature, but under typical mantle temperature occurs at around 660 km.

These phase transitions don't occur at uniform depth as indicated by tomographic studies showing different slab profiles (Goes et al. 2017, Chen et al. 2019). Endothermic phase transitions are negatively correlated between pressure and temperature, so a lower temperature phase transition occurs at greater depth (or higher pressure), therefore a colder slab (relative to its surroundings) will depress the phase transition deeper into the mantle. The lighter phase transition above the MTZ will also be forced lower directly beneath the slab, which will create positive buoyancy pushing the slab up. This may allow for folded/piling up of material at 660 km transition (Faccenna et al. 2017). Each of these polymorphic phase changes have control over mantle interactions in the subduction system. Density, depth and temperature contrasts are all important in affecting slab motion and resulting surface evolution.

Density of the mantle material increases by ~7.3% - 9% from the upper to the lower mantle (Wolstencroft et al. 2011). From post-glacial rebound methods, viscosity also increases by a factor of 10 - 100 between the upper and lower mantle (Schellart 2017), where an increase in temperature also increases with depth (Goes et al. 2017). This is also non-uniform as exhibited by slab behaviour. Overall

mantle temperature has varied over Gyr time scales from the decay of radiogenic elements in Earth's interior among other contributory factors such as (Agrusta et al 2018). Where temperature, density and viscosity change, this also has an effect on the way in which the mantle convects over geological time periods.

The present Earth mantle is thought to be in a transitional phase; it is likely to be in a state between either layered or whole mantle convection (Agrusta et al 2018). The proposed formation of Earth's early continents reflected what state the mantle was in at that time, before cooling to the mantle of today (Agrusta et al. 2018). Mantle conditions determine whether slabs subduct easily and descend past the MTZ, or if they stagnate at the same depth of 660km (Agrusta et al. 2018, Marquardt et al. 2015, Holt et al. 2015, Goes et al. 2017), meaning that they also have control over slab dip angles, which in turn controls crustal processes via the stress transmitted into the overriding plate.
As seen in recent models, slabs will descend into the lower mantle if temperature is higher, or by reducing the viscosity/strength of the lower mantle (Agrusta et al. 2018). Current slab geometries, and whether they descend or stagnate at the MTZ, show examples of both types and are seen globally (Fig. 1.2). This indicates we may be in a layered or transitional mantle convecting state, given the mix of slab profiles.

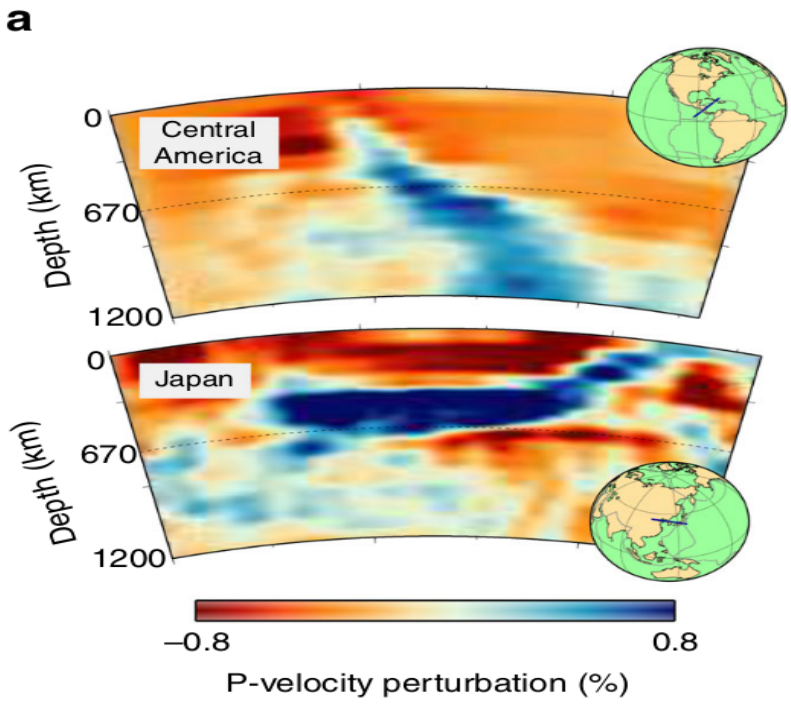

Fig. 1.2. Seismic tomography of 2 slabs. Top slab descending into the lower mantle beneath central America (~10 Ma), the other stagnating at the MTZ beneath Japan (~100 Ma). Taken using 3D MIT-PO8 seismic velocity model. (Li et al. 2008).

For this study, I will be modelling the 660 km mantle phase transition only. In doing so, using an accurate viscosity profile is essential to create realistic slab geometries in subduction models. Upon reaching MTZ, the downward motion of older slabs are resisted by the phase change and creates slab rollback. Younger slabs tend to pile up in one point on the transition, and the slab weight will eventually help them to descend through the MTZ with very little rollback. As will be shown later, slab-mantle interaction processes are crucial in understanding the subduction system in the Andes.

1.2 Slab properties

The slab involved at the Andean margin is sourced from the East Pacific Rise and is composed of extruded and then cool mantle material. This is overlain with a oceanic crust formed by metamorphosed sedimentary cover units, and in some cases by buoyant material forming ridges such as at the Juan Fernandes, Carnegie or Nazca ridge (Fig 1.1). Slab age at the modern trench in the Andes is at its oldest at the Central Andes, younging to both the south and north (Fig. 1.3). This configuration has been fairly consistent since the period of Andean uplift over the last ~60 Myr (Scott et al. 2018).

Due to its negative buoyancy, convecting mantle material from the asthenosphere below attaches to the underside of the plate from diffusive cooling of the plate from above. This leads to stiffening as it is driven towards the subduction zone. 90% of this driving force is due to slab pull, with slab push and convection adding the rest (Turcotte and Schubert 2014). Therefore, the older a slab is, the more opportunity it has had to become thicker and thus becomes denser with age. This in turn means that the slab becomes rigid, negatively buoyant and less flexible. This is a crucial relationship when understanding the dynamics affecting the development of the Andes.

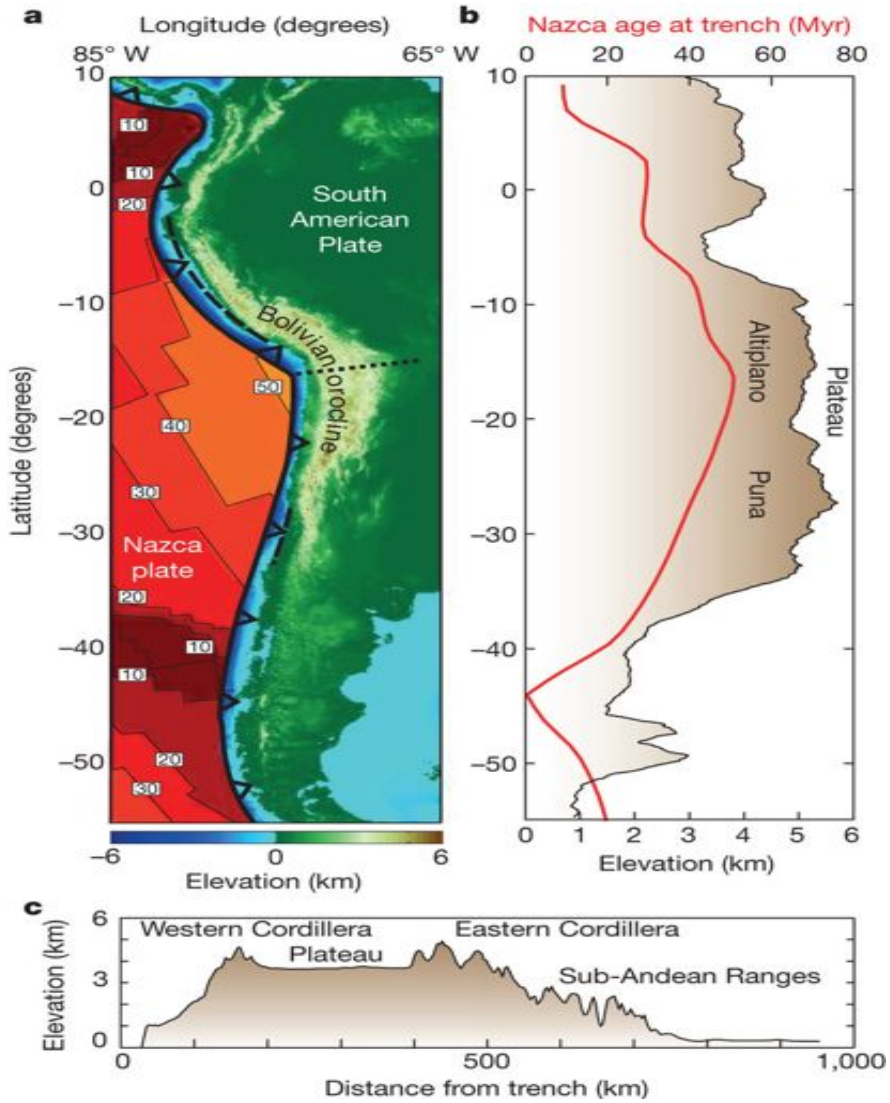

*Fig. 1.3. **a**) Slab age distribution at the trench shown in changing colour with along-margin dashed line showing areas of flat slab. Dotted line orthogonal to trench shows profile of **c**. Red line in **b** shows age of slabs at trench (top x axis) with maximum trench parallel topography (bottom x axis). **C** shows present-day topographic profile. From Capitanio et al. (2011).*

The flexibility and therefore the age of the slab either aids or hinders its descent into the lower mantle (Goes et al. 2017). Younger slabs tend to penetrate to the lower mantle, allowing for limited coupling between them and the OP, and ease of subduction increases. Little rollback or trench retreat happens,

as the margin slips by without reduced friction at the trench. They also don't have much excess weight, so that the OP isn't pulled towards them as with older slabs. This also means the trench stays fixed, allowing material to then pile up at the MTZ, and may 'avalanche' into the lower mantle (Condie 1998). The slab may then anchor relative to the lower mantle, which resists the westward motion of and generates stresses in the OP (Agrusta et al. 2018, Schellart 2017). Slab anchoring is a process identified using numerical modelling and seismic imaging to suggest that the slab reaches into the upper portion of the lower mantle, essentially slowing subduction and reducing movement in the entire system. This locks up the system and causes periods of high compressive stresses on the OP (Facenna et al. 2017).

Comparatively, older slabs tend to be less steep, partly because they don't bend as readily upon descent. This is controversial since the rigidity of older slabs competes with their high density, which would typically be associated with rapid sinking of any denser object into a medium. This leads to a lack of a clear correlation between slab age and slab dip angle (Heuret and Lallemand 2005). However, through seismic imaging methods, this is thought to allow them to arrive sub-horizontally at the mantle phase transition (660km), with limited piling up of material, and remain suspended due to near equilibrium being reached caused by mineralogical phases keeping the slab buoyant as it tries to descend. Rollback occurs, possibly along with trench retreat and extension of the OP, leading eventually to supposed anchoring along the MTZ (Faccenna et al. 2017), which in turn creates compression and tectonic shortening in the OP due to increased friction and coupling at the trench once rollback has slowed or stopped altogether. These slabs therefore are strong, dense and not flexible and tend to be much thicker than their younger counterparts.

When applying this to the Andes, orthogonal to the trench we can utilise seismic profiles to get an idea how these slabs behave as they descend (Fig.1.4). Seismic profiling shows earthquakes that occur in the brittle crust, either on top of the oceanic plate or OP. In sections of suspected steep slab subduction, earthquakes are recorded up to 300 km and ~500 km east of the trench. Flat slab subduction is thought to occur where earthquake depth is less deep at around 150 km depth, but beyond 600 km east of the trench beneath the OP. From these earthquake depths and localities, projected slab morphologies can be determined.

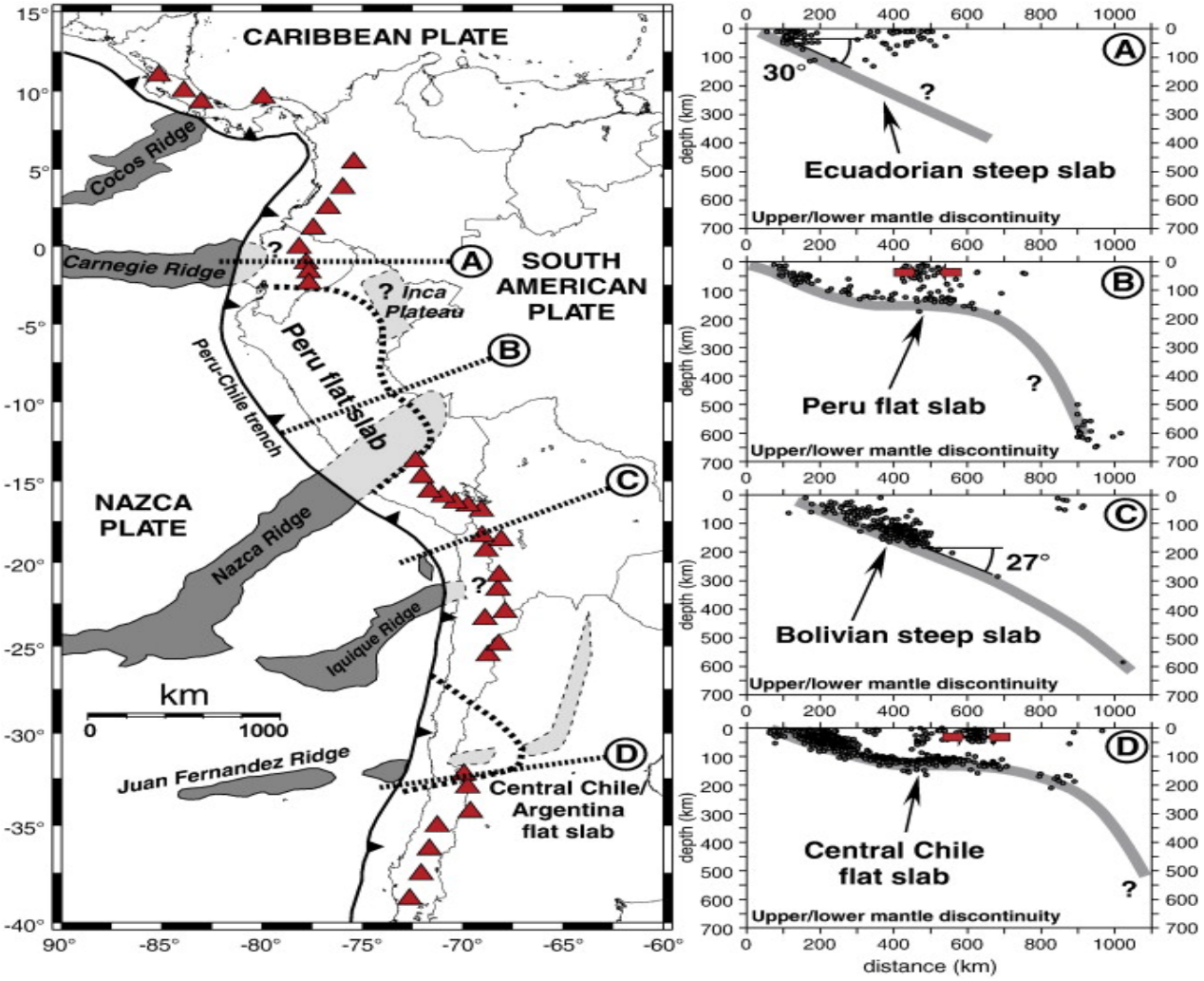

*Fig. 1.4. Slab profiles at right angles to trench. Profiles show that **B** and **D** are younger slabs (see Fig. 2), where **C** is the oldest across the Andes. At **A**, Carnegie ridge allows for required crustal material to steepen slab profile, as has increased buoyancy. Red triangles indicate areas of volcanism, which correlates to the presence of an asthenospheric wedge between the continental plate and Peruvian flat slab and Central Chile/Argentina flat slab. Black dots on profiles indicate areas of seismicity, with red arrows indicating areas of compression in the upper plate. Espurt et al. 2008.*

With the current age distribution of the Nazca plate and the resulting crustal thickness estimates (Fig. 1.3), together with seismic profiling (Fig. 1.4) inferences can be made about the formation of the orogenic plateau. Through the variation seen in the slab properties at the margin in terms of age, thicknesses and slab dip profiles, lines between them and the surface expressions seen in the South American plate hints at the importance of slab parameters. The slab variations observed support some of the main aims of this thesis, particularly their responsibility in determining stresses in the OP.

1.3 Overriding plate and generation of crust

The South American plate is the smallest of Earth's major plates, with an estimated size of 43,000,000 km^2 (Espurt et al. 2008). Stretching from the spreading ridge in the South Atlantic Ocean in the East, across to the boundary with the Nazca ridge that descends beneath it, the plate is composed of terranes of various ages. Since the formation of cratons such as the Amazonia in the Proterozoic and subsequent break-up of Gondwana in the Jurassic, the South American plate has undergone many phases of deformation. These phases have left behind relicts of events such as the Pampean orogeny in the Cambrian as Gondwana collided with Laurentia (Weinberg et al. 2018), to the more recent subduction since the Jurassic leading to the modern stage of Andean uplift over the last ~60 Myr (Scott et al. 2018). Parts of this history have carefully been recorded in areas such as the Neuquén basin, which show changing deformation style and sediment provenance variations since the Jurassic (Horton 2018).

Fig. 1.5. Shows crustal thickness and Andean topography between 23 and 39˚S. Shaded region shows area where topography exceeds 3000 m above sea level. Topography has been heightened to 10 x vertical exaggeration, with dotted region showing crustal thickness maximum in km. Ramos et al. 2005.

Since the deformation history from the Jurassic to now has been varied, it is known that significant crustal thickness variations are present, often reaching over 70 km. This occurs throughout the plate but is notably varied at the margin at the trench (Fig. 1.5).

At 23˚S (Fig. 1.5 A), the crust is at its thickest and widest, with thinning occurring to the south that matches the thinning of the ranges adjacent to the central Andean Plateau. Coupling at the trench at Fig. 1.5 A is also thought to be at its highest value, with an active arc segment of the margin also occurring here. Where this active arc is emplaced, and coupling is thought

to be high, compressive stresses occurring at this point of the margin may be sustaining the plateau at this point (Scott 2018). This creates OP crustal thickness unmatched anywhere else on Earth in the same tectonic setting.

It is said that at oceanic plate to continental plate subduction margins, horizontal compression is generated from the coming together of both plates causing coupling, while rapid slab rollback creates extension (Turcotte and Schubert 2014). If coupling between the two plates occurs causing compressive stress, this compression may also keep the OP in isostatic equilibrium. Uplift generated by hotter ascending asthenosphere (Bishop et al. 2018, Sundell et al. 2018) may have compressive stresses acting upon the active arc, sustaining equilibrium and avoiding gravitational collapse. Horizontal compression may therefore be continuous, thereby contributing to thickening of the continental crust.

With this in mind, analysing the OP crustal thickness through time could enable predictions to be made regarding compressive stresses acting on the OP. Subsequently, the relationship between crustal thickness and Andean magmatism has been analysed using radiogenic isotopic ratios (Sr and Nd) of Quaternary arc lavas, where there is a clear correlation between enriched ratios and seismically imaged crustal thicknesses, which can exceed 70 km in places (Scott et al. 2018).

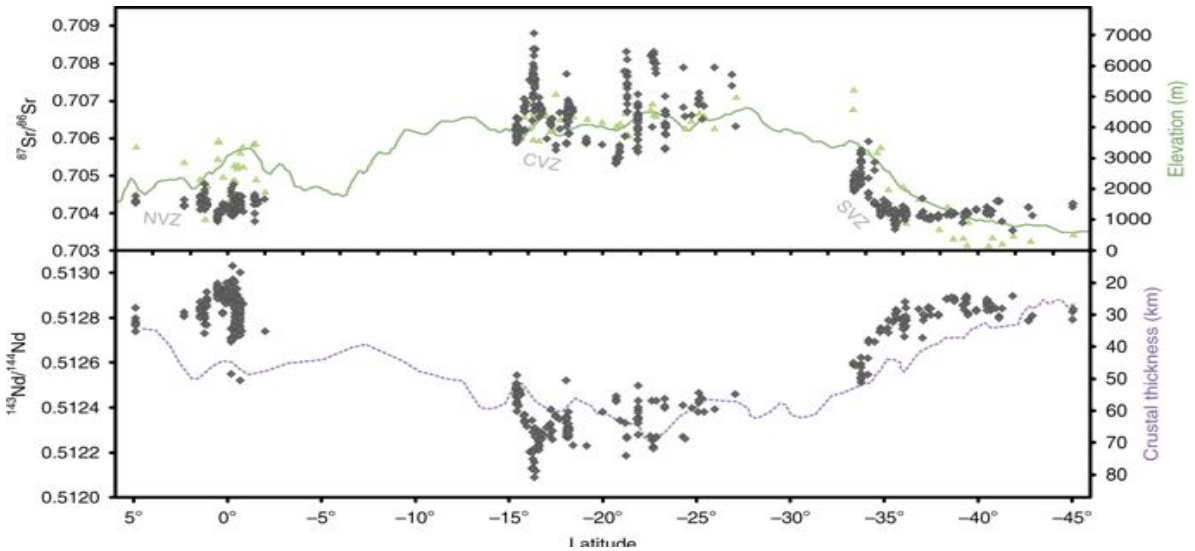

Fig. 1.6. Comparative $^{87}Sr/^{86}Sr$ and $^{143}Nd/^{144}Nd$ ratios of arc lavas. These have a clear correlation between isotopic ratio and elevation (top, compiled using digital elevation model) and against crustal thickness (bottom, five period moving average). Black diamonds indicate isotopic ratios of whole-rock Quaternary arc lavas, with green triangles giving volcano base elevation. From Scott et al. (2018).

Much of the buoyant material forming the OP crust is generated by ascending melt - around 70 – 80% (Allmendinger et al. 1997). This process along with compressive stress increases the thickness of the OP on the surface and at the base of the plate developing a buoyant lithospheric root (Allmendinger

et al. 1997, Sobolev and Babeyko 2005). The lithospheric root allows for a stable base for crustal material to develop.

In developing this root, lithospheric peeling of the underside of the arc may occur if positioned beneath the eclogite/gabbro phase transition depth (~ 50 - 60 km) of the OP, possibly via corner flow. Corner flow is simply mantle material flowing into the mantle wedge, then descending with the motion of the down-going slab. This process of denser eclogite being removed, increases buoyancy and elevation via isostasy of the OP. This scenario is what we would expect to find associated with the thickest OP crust, which can be seen in the Altiplano/Puna plateau of the central cordillera (Sobolev and Babeyko 2005, Scott 2018).

Crust generated from the current cycle of arc magmatism is only one part of what makes up the volume of the crust, as the South American plate and its along strike margin with the trench has a complex geological history Basin evolution and magmatism is related to 3 aforementioned episodes of tectonic activity at the margin (Fig. 1.7), and involving large and small-scale contact/regional metamorphism (Sundell et al. 2018).

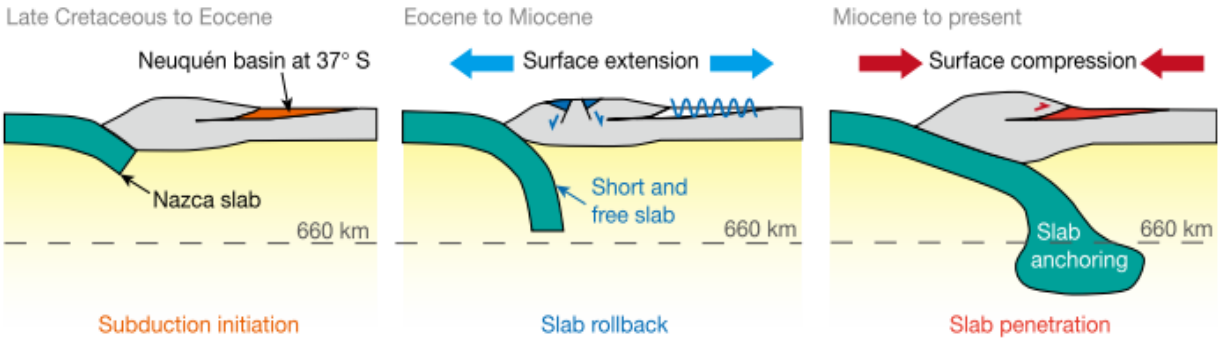

Fig. 1.7. Three tectonic regimes associated with the formation of the Neuquén Basin at 37°S. Timings of event shown at the top of each figure. Top left to indicate neutral conditions, center indicating extension caused by steep slab (seen with blue arrows, wavy blue lines showing timings of unconformities. Kinematic indicators showing half graben formation) and right indicating surface compression (red arrows, with kinematics displaying thrusting). MTZ shown with dashed black line. This interpretation has been compiled using recent tomographic studies, suggesting that slab anchoring during the Miocene caused compression. This differs from previous models, which suggested slab flattening at the MTZ rather than anchoring during the Miocene caused compression of the OP. From Chen et al. 2019, adapted from Faccenna et al. 2017.

The mantle, OP and subducting slabs that fundamentally make up the Andean subduction system are linked to form processes creating the region's complex growth history, part of which can be visualised using isotopic data back as far as the Jurassic (Fig. 1.8). Similar to Fig. 1.5, isotopic signatures have been compiled by Scott et al. (2018) to determine palaeo-elevations for the Andes.

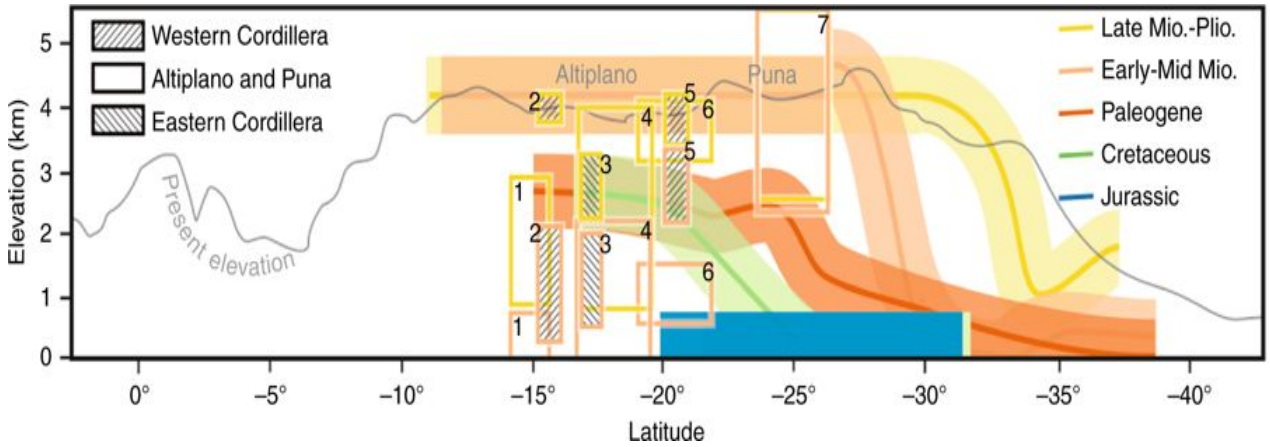

Fig. 1.8. Palaeo-elevations collated using isotopic ratios of strontium within arc lavas since the Mesozoic up to the present. These show surface uplift of the central and southern Andes, where surface elevation is related to crustal thickness via isostasy and coloured lines give elevation estimates. Correlation is thought to hold true for previous times and inferred from previous studies (largely compiled using Strontium isotopic ratios). Previous studies' estimations shown within boxes, greatly simplified to fit similar time intervals of this latest research. Scott et al. 2018.

This geochemical analysis uses the same concept of crustal signatures from lavas of different ages (Fig. 1.6), to give crustal thickness and resulting palaeo-elevations in the Andes over periods of geologic time, back to the Jurassic (Fig. 1.8). This enables a view of growth history in the Andes and shows that there has been significant development since the early-mid Miocene.

1.4 Hypotheses and approaches

The Andes have unusually thick crust and high elevations. History suggests that the phases of deformation occurring at the margin have changed over time (Horton 2018). Largely, since the break-up of Gondwana, extension at the western edge of the South American plate has thought to occur, with compressive stresses then indicating the onset of Andean growth at roughly 60 Ma (Scott 2018). This is marked by the development of the high and wide Central Andean plateau, caused by separate phases of volcanism occurring in the active arc and possibly further supported by compressive stresses preventing gravitational collapse. The plateau is tapered off by thin ridges both north and south from its thickest portion. Notably, the age of the subducting Nazca plate at this portion of the margin is 50 Myr, decreasing in age both north and south. This thesis aims to explore the reasons for this further. In order to do this, we propose the following hypothesis.

First, down going slab age is an important driver for the north-south variation of crustal thickness seen in the Andes. When assessing the many interesting aspects and possibilities as to what drives the stresses acting on the Andean margin, the strongest statistical correlation between the various parameters at the Central Andean region of the subduction zone is between slab age at the trench and overriding plate crustal thickness (Fig. 1.9).

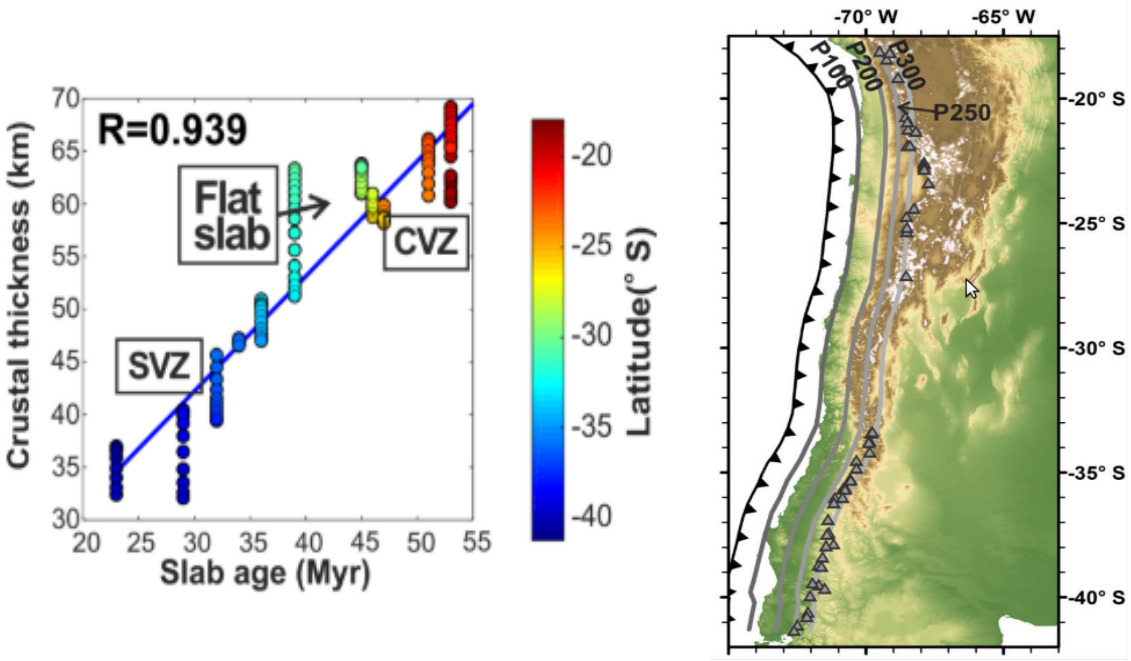

Fig. 1.9. Shows trench parallel profile P300 from top right map. Geophysical estimates between the lithosphere/asthenosphere boundary (LAB), with slab ages at the trench. Colour identifiable for latitude to highlight differences. From Scott 2018.

By changing the age of the slab - which in turns changes its physical properties in reality - we can analyse whether this correlation can be used to predict topographic changes over time. These changes could potentially be further constrained using previous research of isotopic signatures used to interpret palaeo-elevation of the Andes in relation to crustal thicknesses (Scott 2018), so as to build upon a growth history of the orogen over a broader time scale; or perhaps even further into answering ongoing questions such as the conditions under which growth may have started, and why this growth can be episodic or delayed despite subduction occurring for ~250 Myr or more.

The second hypothesis is that mantle flow associated with Nazca subduction plays a crucial role in providing the compression needed to form and maintain the high Andes. Compressive stresses have been attributed to a number of processes, however when varying the parameters associated with these processes, common to each of them is the concept of convecting currents and their contribution to plate motion. Holt et al. (2015) found that trench directed convection may play a significant role in

increased compressive stresses, so to alter parameters that would induce such an increase is a concept I will be looking to explore over the course of this project.

To enable topographic growth, compression within the OP occurs by westward motion of the South American plate, with slabs then rolling back depending on their age/buoyancy. This then requires either flattening at the MTZ, or anchoring in the shallow lower mantle (Fig. 1.7, right image) to initiate the process (Faccenna et al. 2017, Chen et al. 2019) which leads to greater coupling at the trench and expected mechanical failure of the foreland as seen in basin variation along strike (Sobolev and Babeyko 2005, Sundell et al. 2018).

I created 2D numerical models simulating the relationship between crustal thickness and age of the slab at the trench. Slab age at the trench affects slab rigidity and propensity of the slab to bend, thereby affecting the compressive stresses in the overriding plate. This in turn influences shortening and crustal thickening, which translates into Andes height. I then continued by modelling other parameters such as mantle viscosity, friction at the trench, thickness of the OP and incorporation of the 660 km mantle phase transition.

The models have also been used to investigate the interaction between slab age, slab penetration into the lower mantle, mantle convection cells, and westward South American motion. In doing so, investigation of the stress regime in the overriding plate and the role of slab dynamics on the Andes crustal thickness can be better understood.

By varying the parameters listed above allows for this study to be focused around the process of crustal thickening being generated by horizontal stresses in the overriding plate, from which we have based our models. By doing so, we are excluding magmatic processes for increasing thickness and erosion as reducing thickness. By simplifying the models in this way and using the slab age and crustal thickness correlation outlined in the work of Scott et al. (2018), the central question to this thesis is outlined: does increased slab age lead to thicker continental crust?

Typically, slabs of increased age have long thought to rollback and generate extension in the OP (Turcotte and Schubert 2014), so this correlation is against long thought slab and OP interaction. There may be other factors that affect the state of stress in the OP, which may be the case when altering parameters to see the effects generated.

In Chapter 2, I will introduce the methods used for this study including all governing equations necessary for running the models and calculations. This is followed by a presentation of the results in Chapter 3, with discussion of these results in Chapter 4. Chapter 5 highlights some of the model limitations and outline for future work. Finally, I will conclude what this study has found, ending with a full list of references.

Chapter 2. Methods

2.1 Introduction

Mantle dynamics and plate tectonics arise from the fact that the mantle exhibits a gravitationally unstable thermal situation, in which cooling takes place from above and heating from below. The result is generation of convection where cooler material nearer the surface has an increased density to material at a greater depth, which expands from heating respectively. The upper cool layer sinks, whereas the basal heated layer rises creating convection.

The main aims of this project are to explore the dynamics of subduction zone systems and the potential creation of compression in the overriding plate using numerical models. It is in this chapter where the governing equations and associated physical and model parameters such as mantle viscosity, upper weak layer strength, overriding plate thickness and the effect of incorporating phase changes are defined. The numerical models are all created using the finite element method (FEM) software tool ASPECT (or the Advanced Solver for Problems in Earth's ConvecTion). Computations were done using the ASPECT code version *2.2.0*, see \cite {KHB12,heister_aspect_methods2,aspect-doi-v2.2.0,aspectmanual,rose_freesurface,gassmoeller_particles} (Kronbichler et al. 2012, Bangerth et al. 2018)

First, I introduce the equations that govern the physics of the 2D models in this chapter. An outline of the rheology and associated flow laws will also be discussed, then followed by a description of the default model set up and an outline of the temperature and viscosity profiles used. I will then explain how I used the models to explicitly address the hypotheses and aims of this thesis, followed by an outline of the numerical methods used. All units and notations are outlined in table 1.

Symbol	**Meaning**	**Unit**
A	Prefactor (diffusion/dislocation)	$Pa^{-n}\ s^{-1}$
c_i	Compositional field	
C	Cohesion	Pa
Cp	Specific heat	$Jkg^{-1}K^{-1}$
E	Activation energy (diffusion/dislocation)	$Jmol^{-1}$
g	Gravity	ms^{-2}
H	Internal heat production	Wm^{-3}
k	Thermal conductivity	$Wm^{-1}K^{-1}$
P	Pressure	Pa

R	Gas constant	$Jkg^{-1}mol^{-1}$
T	Temperature	K
u	Velocity vector	ms^{-1}
V	Activation volume (diffusion/dislocation)	m^3mol^{-1}
$\dot{\epsilon}$	Strain rate	s^{-1}
$\dot{\epsilon}_{ii}$	2nd invariant of the strain rate tensor	s^{-1}
η	Viscosity	Pa s
κ	Thermal diffusivity	m^2s^{-1}
$\nu\rho$	Density	kgm^{-3}
σ	Stress tensor	Pa
σ'	Deviatoric stress tensor	Pa
ϕ	Angle of internal friction	°

Table 1. Listing all notations used for this chapter and throughout this thesis.

2.2 Governing equations

To uniquely determine deformation in the solid Earth, we consider the conservation of mass and momentum and incorporate Newton's second law (force = mass x acceleration). Like most geodynamical codes, ASPECT solves Stokes' equations. On the very long timescales, Earth's interior behaves as a fluid, and so the applied form of the momentum equation will be for a viscous fluid. In addition, we include conservation of energy. The reason for solving the energy equation is that density and rheology in the momentum equation are dependent on temperature. Further to this, since we are incorporating phase changes as a material property into the models, we also consider the conservation of composition to track movement of different rock types.

Where thermal differences and resultant density contrasts are very small, they can mostly be neglected, and we can apply the Boussinesq approximation (Turcotte and Schubert 2002). Essentially, the Boussinesq approximation allows the mantle and lithosphere to be treated as incompressible fluids, where density variations are ignored in all terms except for those directly driving the flow and deformation (Turcotte and Schubert 2002).

The first of the conservation equations discussed here is conservation of mass: the net amount of mass flowing in or out of any particular volume in the model domain (typically referred to as the 'control volume') must equal the resultant mass increase or decrease, or, when volume remains the same, a density increase or decrease:

$$\frac{\partial \rho}{\partial t} + \nabla \cdot (\rho u) = 0 \quad (2.1)$$

Where u is the velocity of the material (or flow in a non-Newtonian fluid), ρ = density. If density changes are ignored, then the Boussinesq approximation can be implemented to reduce Eqn. 2.1 to:

$$\nabla \cdot u = 0 \quad (2.2)$$

In two dimensions, the conservation of momentum has two unknown velocities (in horizontal or vertical direction), and we can elaborate Newton's second law to the purpose of fluid flow to describe how material flows and deforms:

$$-\nabla \cdot [\, 2\eta \, \dot{\epsilon} \,] + \nabla p = \rho g \quad (2.3)$$

where $\dot{\epsilon}$ is the shear strain rate tensor, and ρg is the density driven gravitational force. By combining this equation with the conservation of mass (2.2), we generate Stokes' equation which is central to determining how material flows in the box. Density ρ changes with T and phase transition as well as composition. In the models however, we have crust that is weak but not buoyant, in other words, we chose density to be unaffected by composition. We have therefore set density change by composition to zero. No latent heat effect from phase changes has been incorporated, which is in line with the Boussinesq approximation.

Like mass, energy must be conserved in the system. So, in the absence of heat sources or sinks, any temperature increase or decrease within a control volume must balance the heat flowing or diffusing in or out of that volume. This results in the following energy conservation equation:

$$\rho Cp \left(\frac{\partial T}{\partial t} + u \cdot \nabla T \right) - \nabla \cdot k \nabla T = 0 \quad (2.4)$$

where ρCp the heat capacity and k the thermal conductivity. In line with the Boussinesq approximations, shear heating, adiabatic heating, radiogenic heating and latent heat due to phase changes have not been incorporated in the conservation of energy equation.

Distinguishing between different rock types, or materials, that make up each model is an important factor that requires tracking. We describe such materials by giving them each a unique 'composition' value. As material moves, their composition value should move along. Mathematically, this can be described with the following composition conservation equation:

$$\frac{\partial c_i}{\partial t} + u \cdot \nabla c_i = 0 \tag{2.5}$$

Where c_i is the composition of material i.

2.3 Rheology

The numerical software tool ASPECT assumes that materials within the models can be treated as viscous fluids. Therefore, rheological laws must be defined for the different materials, so as to distinguish between the way in which the materials in the models both flow and deform. Two materials will be used in the models, crust and mantle, and each will need a complete set of equations that describes their rheology.

The models use a visco-plastic rheology, i.e. deforms in both a viscous and plastic manner. To that end, we define viscous flow laws for both dislocation and diffusion creep, which creates a 'composite' rheology. Through using a Drucker-Prager yield criterion (stress limiting rheology), we control plastic deformation.

Dislocation and diffusion creep can each be defined (Fraters 2014; Maunder 2017; Farangitakis et al. 2019):

$$\eta = 0.5A^{\frac{-1}{n}} \dot{\epsilon}_{ii}^{\frac{(1-n)}{n}} \exp\left(\frac{E+pV}{nRT}\right) \tag{2.5}$$

Where A = viscosity prefactor; n = stress exponent; ϵ_{ii} is the second invariant of the deviatoric strain rate tensor; E = activation energy; V = activation volume and R = universal gas constant (Kronbichler et al. 2012). For diffusion creep n = 1; dislocation creep n > 1 (≅ 3.5) (see Table 1).

We utilise an equivalent of a Mohr-Coulomb yield surface, which is based on the angle of internal friction and cohesion to simulate brittle behaviour, and can be defined as follows:

$$\sigma_y = Psin(\phi) + Ccos(\phi) \tag{2.6}$$

Where C = cohesion and ϕ = angle of internal friction.

We then must use these equations to define an effective viscosity using the following steps. First, we can then define an effective 'yield viscosity' (η_y) which is calculated as: $\eta_y = \sigma_y / (2\epsilon_{ii})$. This defines a form of plasticity commonly used in geodynamics. By combining this yielding viscosity (η_y) and the two viscosities derived from Eq. 2.5 for diffusion (η_{diff}) and for dislocation (η_{disl}), we can then form

an effective viscosity. Firstly however, a composite viscosity (η_{comp}) is defined as the inverse of the sum of the inverses of the diffusion and dislocation viscosities: $\eta_{comp} = \frac{(\eta_{diff} + \eta_{disl})}{(\eta_{diff} + \eta_{disl})}$.

With this final composite viscosity defined, applying the yielding viscosity then gives us the effective viscosity (η_{eff}), of which we take the minimum of the composite and yielding viscosities as follows: $\eta_{eff} = \min(\eta_{comp}, \eta_y)$. This is the effective viscosity used for combining the defined dislocation and diffusion creep, while utilising a Drucker Prager yielding criterion.

Thermal and rheological parameters and their specific values are listed in table 2 below. These correspond to equation 2.5 and represent the prefactors for diffusion/dislocation creep (A), activation energy for diffusion/dislocation creep (E) and activation volumes for diffusion/dislocation creep (V). The values for E and V remain unchanged for each of the three materials (slabs, upper weak layer of subducting slab and mantle material) in each model, though A values change when altering either the mantle viscosity or the upper weak layer (UWL) strength.

A		Material 1 (slab)	Material 2 (mantle)	Material 3 (UWL)
	wmwc	3e-17	3e-17	10e30
	mmmc	1.5e-17	1.5e-17	5e30
	smsc	0.75e-17	0.75e-17	2.5e30
E		375.e3	375.e3	0
V		1.e-6	1.3-6	0

Table 2. Where wm, mm and sm are a weak, medium or strong mantle. Wc, mc and sc are a weak medium or strong 'crust' or upper weak layer (UWL) at the plate interface. See table 3 for full listing of prefixes and suffixes denoting model names.

These are the default values used throughout this study to differentiate between each parameter when altered.

2.4 Model setup

Figure 2.1 shows the initial and boundary conditions of the model setup. The default two-dimensional model set up includes a slab of age-dependent thickness subducting beneath an overriding plate (OP) of a fixed, initial thickness set to 100 km, (although we also explore models which have an OP of 50 km thickness for comparison. The slab also includes a weak crust, presented through an upper weak layer of 6 km thickness, which can be increased or reduced in strength.

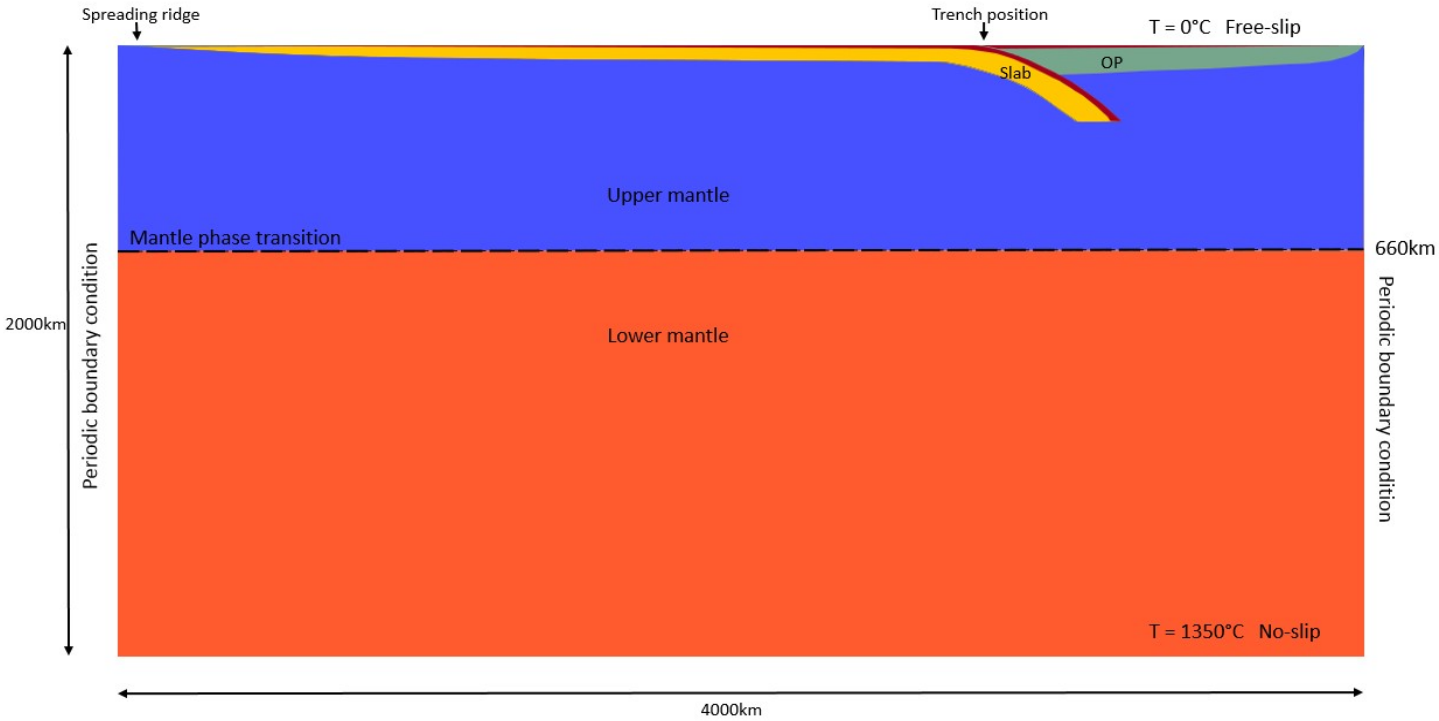

Fig. 2.1. Schematic for initial model setup. Box ratio = 2:1 for default, with the slab (yellow) and OP (green) treated as the same physical material as both the upper and lower mantle (blue and orange respectively) though they differ in viscosity and temperature (Fig 2.2 for temperature, Fig. 2.4 and 2.5 for viscosity). Upper weak layer (UWL) above the slab and OP (red) is treated as a different material with an adjustable mechanical strength.

Periodic side boundary conditions are implemented, so that what leaves on the right hand side (RHS) of the box will emerge on the left. This includes a compositionally driven buoyancy effect when slabs reach the 660km mantle phase transition boundary, as well as a free-slip upper surface and a no-slip bottom boundary condition within the box. Both the spreading ridge and trench are free to move along the frictionless upper surface, and across the periodic boundaries.

The relatively large box size ensures that the objectives for analysing the compression generated in the OP could be accurately compared across all the models.

This setup in part also reflects standards from previous studies with regard to periodic boundary conditions and free slip surfaces at the top and no slip surface at the base of the box, with 200km curvature radius of initial slab position (as in Holt et al. 2015), but exhibits different initial slab thicknesses where many other studies keep uniform thicknesses equal to default slab thicknesses (Faccenna et al. 2017, Holt et al. 2015, Agrusta et al. 2018).

Effective exploration of our aims and objectives for the correlation between slab age and crustal thickness from a numerical perspective was then possible through alteration of parameters – and resultant compression in the OP – since we could identify what were the strongest individual or combinations of factors having an effect on the system having set a balanced default.

Some of the model calculations are performed with a box of double the horizontal extent to explore the effects of the side boundaries. This has been incorporated into a section at the end of the thesis for future work, as time limitations did not allow for a full investigation.

2.4.1 Temperature profile

We use a fixed initial temperature profile, with (T) = 0˚C at the surface and a potential temperature of 1350˚C throughout the upper and lower mantle defining our initial conditions. The oceanic plate is created at a mid-ocean ridge on the top left corner of the model domain, and while migrating towards the subduction zone, is exposed to surface conditions of 0˚C. Both plates at the surface are defined using a half space cooling model (Turcotte and Schubert 2014) with an adjustable age, reaching mantle temperature at maximum plate thickness depth (50km in default model). The free moving OP is also exposed to surface conditions, with linear temperature at 0˚C reaching mantle temperature at 100km depth in default model (Fig. 2.2).

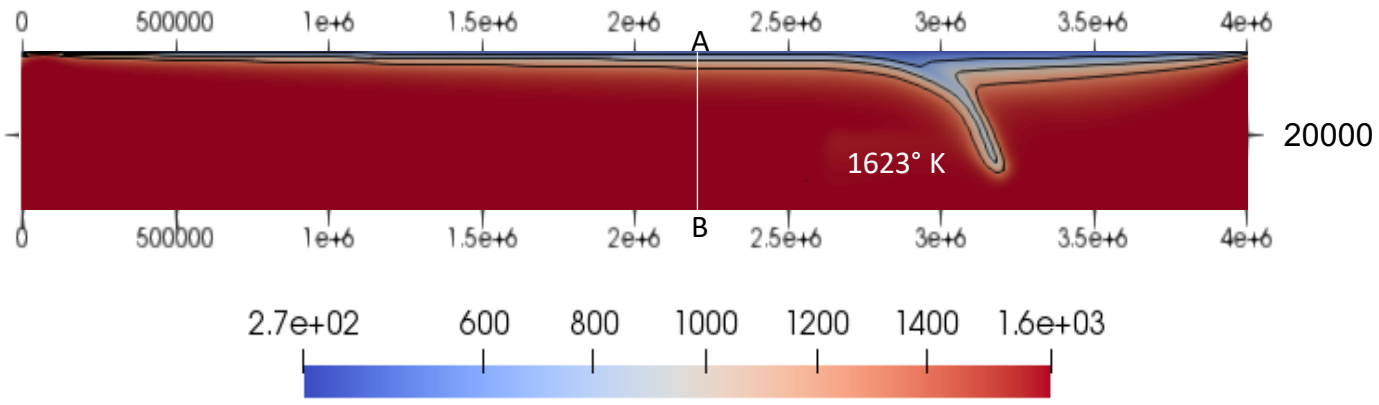

Fig. 2.2. Temperature profile used in models from cool to warm (blue to red) in °K (with conversion is 1350˚C) for mantle temperature. Line of section A-B represented to indicate contrast with depth (fig 2.3). Black lines to indicate temperature contours. Taken at t = 5 Myr and displaying up to 400km depth only.

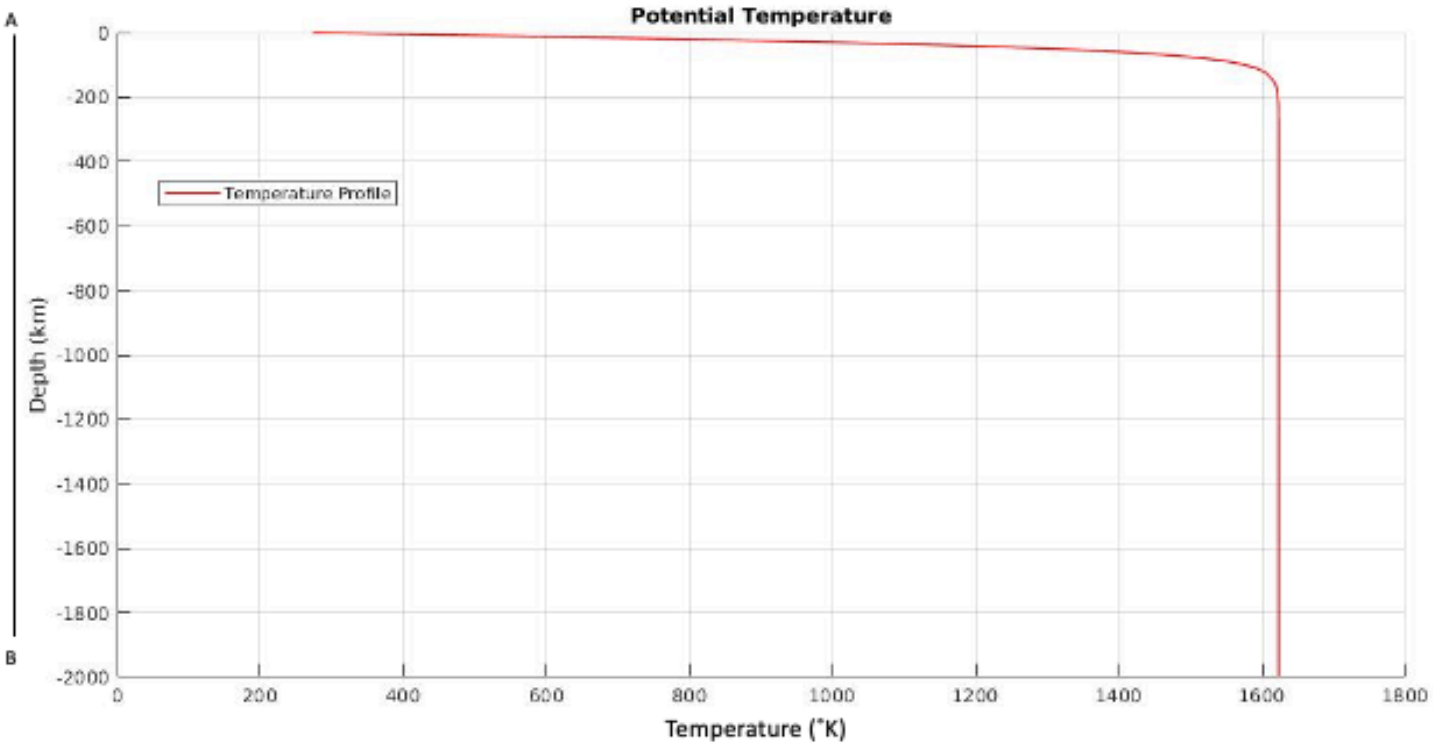

Fig. 2.3. Geotherm across line A-B from Fig. 2.2 from 273˚K – 1623˚K indicating surface temperature of 0˚C and rapid increase to 1350˚C mantle temperature upon reaching the asthenosphere.

By using this type of temperature profile, it is possible to maintain typical slab dynamics where cool slab material sinks into the warmer mantle and focus on varying other parameters so as to further explore the aims and outcomes of this study in terms of OP compression. Such outcomes are discussed in the results chapter 3 of this thesis.

2.4.2 Viscosity profile

Viscosity is a key aspect of how each model runs. Slabs are able to descend more rapidly when reducing viscosity, or less so when increasing it using the functions defined by the equations used (Eq. 2.5 and 2.6). Cool rigid slabs descend into a low viscosity upper mantle, then descend into the lower mantle which has a greater viscosity value below 660km.

The upper and lower mantle differ in viscosity and the contrast between the upper and lower mantle changes between studies based on initial seismic interpretation and post-glacial rebound estimates (Faccenna et al. 2017, Schellart 2017). For this study, I have roughly adopted a viscosity profile from Schellart (2017), where the upper and lower mantle differ by 2 orders of magnitude. We explore three different viscosity profiles: a weak, medium and strong mantle profile beneath the 660 km phase

transition zone (5 x 10^{21}, 1 x 10^{22} and 1 x 10^{22} Pa.S respectively), decreasing by a factor of 2 in each case in the upper mantle. This is also comparatively more viscous to our reference set up (Schellart 2017).

These variations in turn cause strong changes when investigating the aims of this study. For example, reducing mantle viscosity to its weakest setting at 5 x 10^{21} Pa.S creates OP compression values far higher than models in a medium or highly viscous (see Fig. 2.5 for viscosity profiles). The results surrounding the effects of altering mantle viscosity can be seen in chapter 3 of this thesis.

We also define components of our models (slab, mantle, and OP) with different viscosities. As mentioned, we apply 3 different mantle viscosities to all materials in the box (Fig 2.5), with the OP and all slab variations having a maximum viscosity of 1 x 10^{23} Pa.s in all models. These

The UWL above each slab also has an adjustable constant viscosity, defined either as weak, medium or strong (1 x 10^{20}, 2 x 10^{20} and 4 x 10^{20} Pa.s respectively), values of which are also comparable to other studies (Holt et al. 2015). This is used as a weak cold layer to act as the medium between plates, that either lubricates or hinders the slab as it descends.

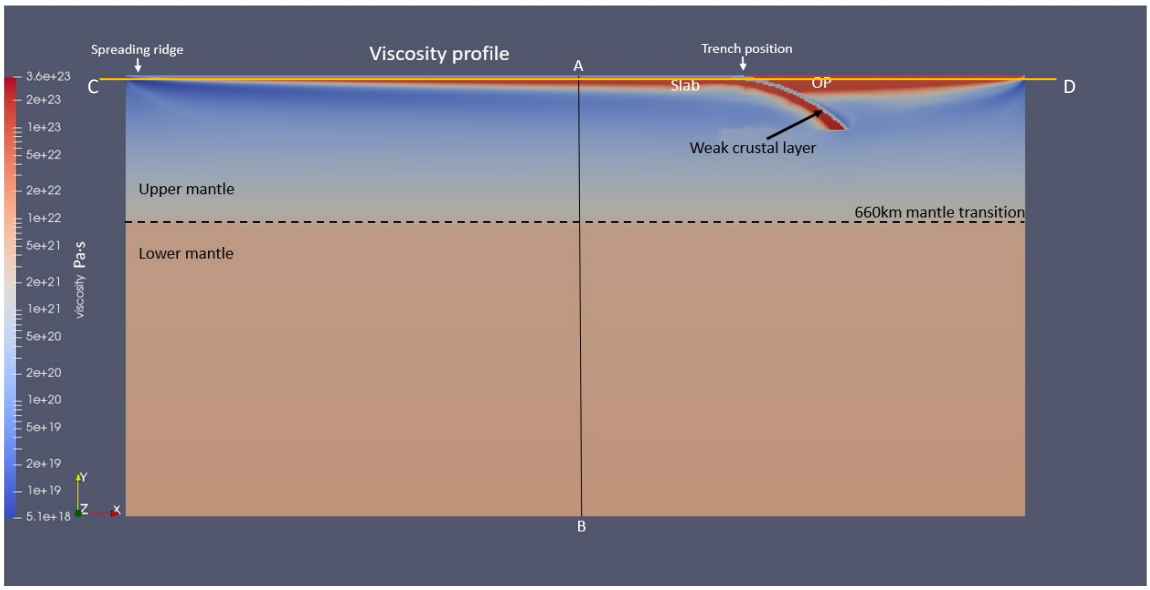

Fig. 2.4. Initial plate configuration in all models, with colours referring to the effective viscosity. This is a 'medium strength mantle', and the corresponding viscosity profile along line A-B is shown as the red line in Fig. 2.5 Line C-D is used for stress profiles in Fig 2.6 and later Figures.

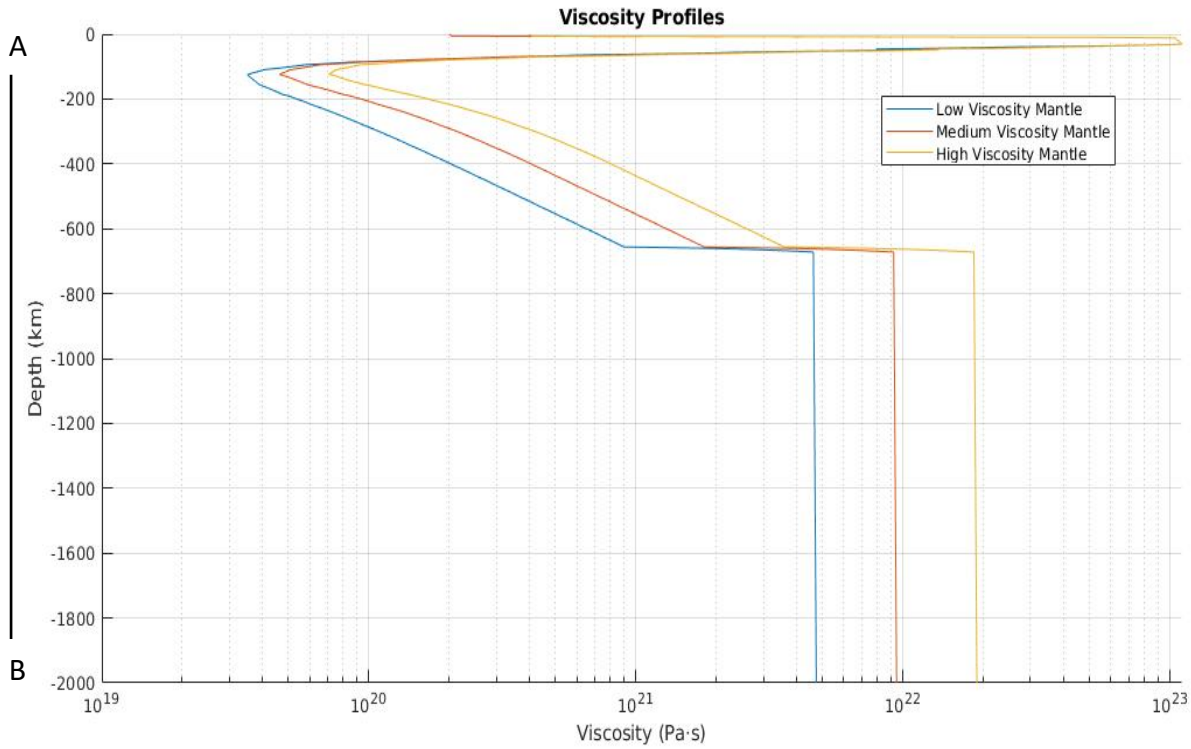

Fig. 2.5. Viscosity profiles used in this study vary by 2 orders of magnitude between the upper and lower mantle, and a factor of 2 between each other. Low viscosity = 5 x 10^{21}, medium = 1 x 10^{22}, high = 2 x 10^{22}. This exerts controls on ease or hindrance of descent into the lower mantle.

These differing default viscosity values will then affect the resistance to slab descent as gravity drives the models. As slabs descend into the mantle, buoyancy is controlled by how viscous the mantle is, where dense slabs will sink faster into the mantle if the viscosity is lower (Turcotte and Schubert 2014). The viscosity is governed initially by temperature with descent being further affected by the strength of the UWL.

2.4.3 Deviatoric stress used to identify compression or extension in the OP

Physical stress is defined as the applied force over unit area:

$$\sigma = \frac{F}{A} \qquad (2.7)$$

Where σ = total stress tensor, F = applied force (in N) and A = area (usually in M^2) so the units of stress $\sigma = N/M^2 = Pa$.

In two dimensions, this tensor can be broken down into 2 normal stress components (σ_{xx} and σ_{yy}) and 2 shear stress components (σ_{xy} and σ_{yx}) acting on a medium (and similar in a 3x3 tensor in three dimensions):

$$\sigma = \begin{pmatrix} \sigma_{xx} & \sigma_{xy} \\ \sigma_{yx} & \sigma_{yy} \end{pmatrix} \quad (2.8)$$

Embedded in this total tensor is the local pressure, *P*, which is defined as the average of the normal stress components:

$$P = \frac{1}{2}(\sigma_{xx} + \sigma_{yy}) \quad (2.9)$$

By removing this pressure term from the normal stress components, we are left with the 'deviatoric stress'. It is this deviatoric stress field that links directly to deformation through the following equation:

$$\sigma = 2\eta\dot{\varepsilon} \quad (2.10)$$

Specifically in this study, we will use σ'_{xx}, the deviatoric stress in the x axis plane deforming the OP:

$$\sigma'_{xx} = \sigma_{xx} - P \quad (2.11)$$

Convention determines that negative values of σ_{xx} denotes horizontal compression, and positive values indicate horizontal tension.

2.4.4 The deviatoric stress component σ_{xx} as a proxy for crustal thickening.

The aim is to explore the possibility of crustal thickening and thickness maintenance from horizontal compression. We do this by looking at horizontal stress profiles of σ_{xx}, thereby ignoring potential crustal thickness contributing processes such as the addition of sediments at the trench, melting of continental crust to produce additional granitic material adding to the OP or the removal of material from delamination beneath the OP into the asthenosphere causing uplift.

Isostatic equilibrium from Modelling the topographic changes at surface level given these processes is also beyond the limits of the model setup. Horizontal stresses are a major contributor to thickening of continental crust along with the aforementioned processes and as such, can be used as a proxy for topographic growth caused by tectonic shortening within the models.

In all the models, a profile at a depth of 20km was taken and the horizontal deviatoric stress was measured. In some of the models, small numerical artefacts were remaining on parts of the OP. To avoid this, stress profiles were plotted just below the surface at 20 km depth. This depth allowed for accurate values to be obtained and to record stresses in materials of the same composition.

The oceanic plate makes up the majority of the left side of the profile seen in Fig. 2.6, with flexure increasing tension at the trench margin where the slab bends (line A), where the outer edge of bending slabs extend, while the inner edge compresses.

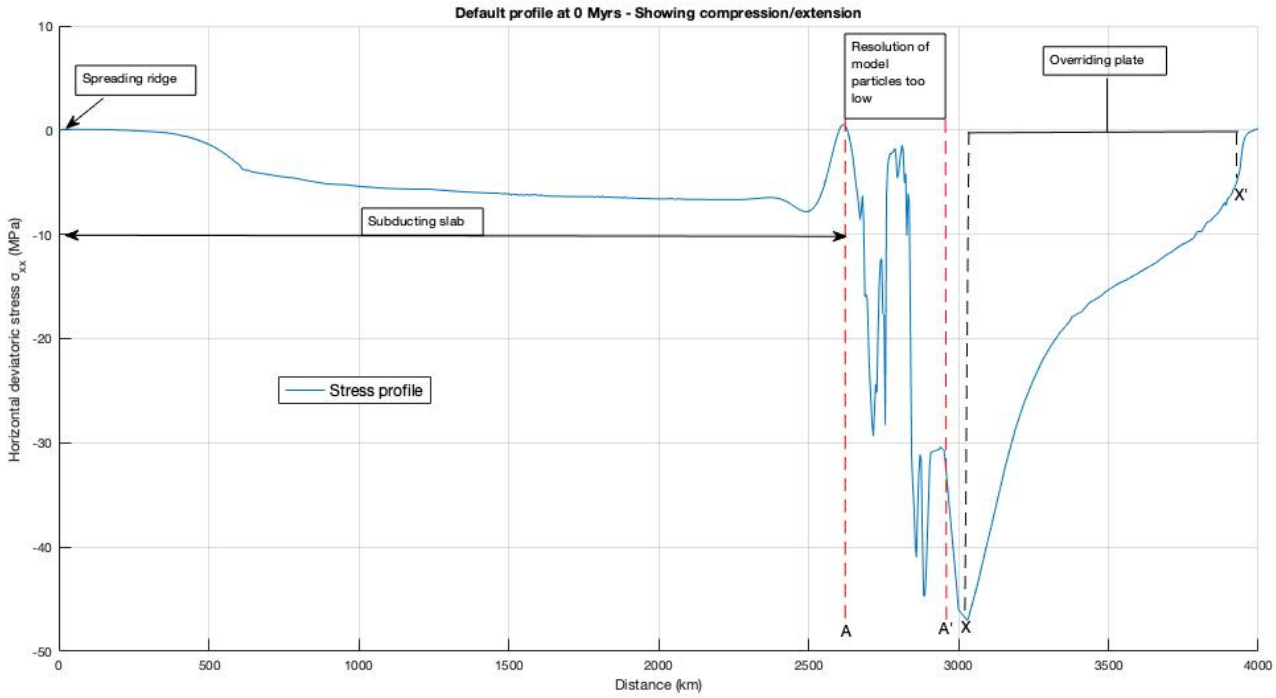

Fig. 2.6. Typical default shape of stress profile at 20 km depth at timestep 0 exhibiting initial positive and negative horizontal deviatoric stress (σ_{xx}) as indicated by line C-D in Fig. 2.4 Positive values are tensional stresses, negative ones are compressional.

Care must be taken at interpreting the resultant stress fields at sharp rheological boundaries, such as at the interface between two materials of different viscosity. In theory, such strength jumps lead to inversely proportional strain rate jumps, which should make stress (defined as the product of strain rate and viscosity) continuous across these interfaces. But in practise, this is not the case in numerical models, since strain rate does not exhibit a true jump due to interpolation procedures. Such sudden jumps in viscosity at compositional boundaries therefore lead to significant jumps in the stress field, as can be seen between A and A' in Fig.2.6 The stress field is reliable anywhere else in the model domain, including at locations of the main focus of this study, at the overriding plate's interior.

The deviatoric stress component σ_{xx} inside the overriding plate between points X and X' (Fig. 2.6) varies significantly (as denoted by the sloping profile between the two points, where compressive stress becomes less negative from X to X'). Point X marks the section of the OP where compressive stress is at its average maximum and it is this point in each of the models where we have extracted much of the data for analysis. This is the appropriate region of the overriding plate where stress is at a maximum through time.

2.5 Numerical methods

The following technical features are incorporated in the ASPECT code used in the numerical models presented in this thesis.

- *Mesh adaptation.* We use adaptive mesh refinement (AMR) in order to obtain accuracy when and where generating detail in our models, but with a reduced computational expense (Figure 2.7).

  The code uses different criteria to determine whether local mesh refinement is needed. In our models, these criteria are based on gradients in temperature, viscosity and material. When a threshold value of such a gradient is encountered, an adjustment of either coarsening/refinement is triggered given the value of the error field between the two cells. The greater the difference, the finer the cells and vice versa; the interface is defined by the user. (Fraters 2014).

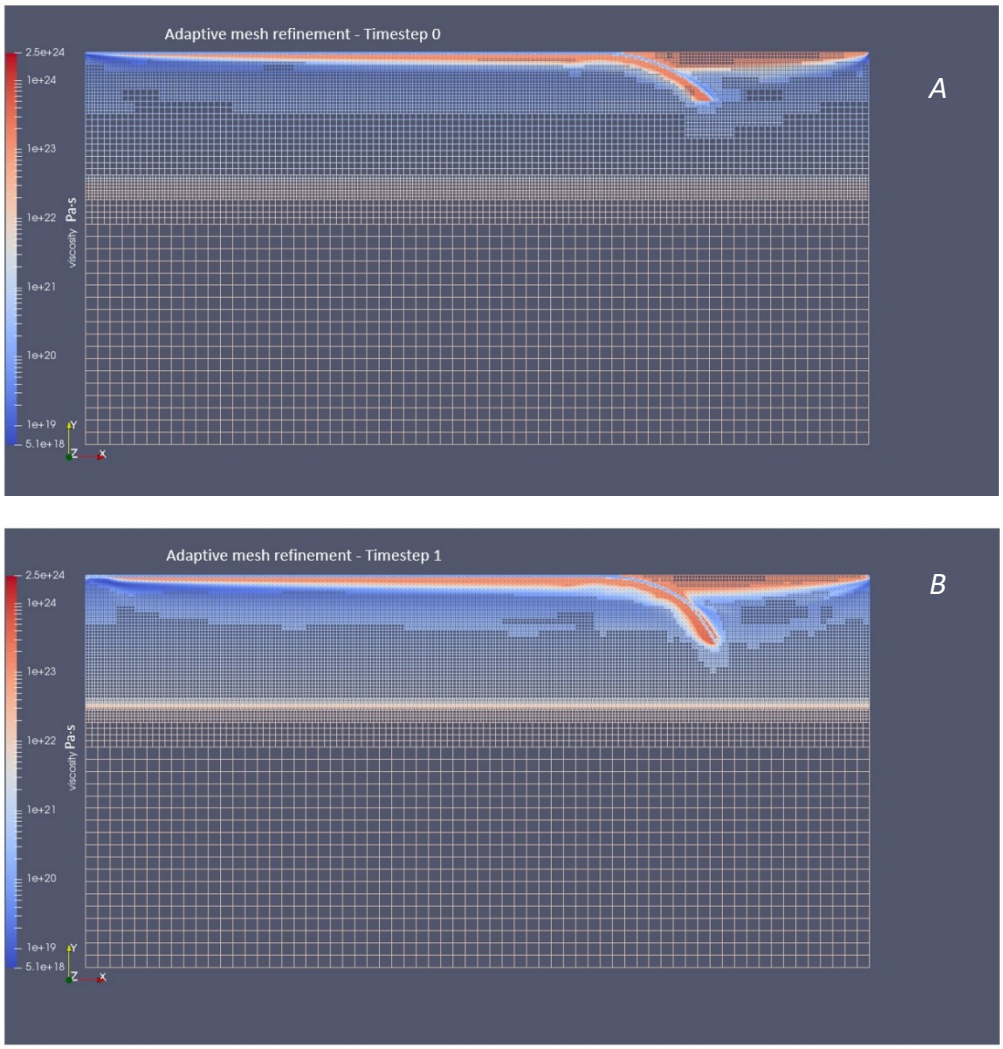

Fig. 2.7a and b. ASPECT adaptive mesh refinement feature. Timestep 0 is the initial setup of the mesh. Refinement occurs as time elapses (5 Myr) and differences between cells are encountered. Differences appear in the upper mantle, as the denser slab descends.

- *Material tracking.* To ensure a weak layer between the converging lithospheres, accurate and non-diffusive tracking of the different materials is essential, and there are several methods available for doing so. The most common method used is known as marker-in-cell. Each marker – or particle – is a physical unit within the model, onto which we can apply material properties or store information about their surroundings. These materials are advected with the flow of the system.

- *Parallel computation/Hamilton Cluster.* We use parallel computation using 96 processors in order to perform the model calculation within an acceptable amount of (wall clock) time. We use Durham's high-performance computing (HPC) system *Hamilton*.

- *Postprocessing.* Not every time step is stored, but specifying what ASPECT should do with the calculations from each timestep that is stored (known as an output time step; stored every 5

Myr) once completed is known within the code as 'postprocessing'. Many iterations occur within each of these for analysis, which are presented in different ways seen in the results chapter of this thesis. This effectively is telling ASPECT to create data so we can evaluate the solutions generated. In this study, I've listed the list our postprocessors in each input file and chose to compute velocity and temperature statistics for analysis.

When visualising our solutions, we need to have the ability to view specific criteria and ASPECT generates a graphical output set by the user. For this study, I've used use *Paraview* (Ahrens et al. 2005) as a means to visualise this output – the solutions – after calculation. This allows viewing particular aspects of the models and to generate plots for interpretation, to try to understand what is happening geologically.

Chapter 3. Results

Factors contributing to the state of stress in the lithosphere at convergent margins are widespread and diverse. Here, I explain the results for a basic model setup and explore the multi-dimensional parameter space for variation in this stress field.

The positive correlation between slab age and compressive stress in the overriding plate is then explored, enabling us to characterise how older slabs increase compressive stress in the overriding plate. The role of mantle viscosity is then investigated, firstly in relation to its variation in conjunction with altering slab age, secondly how adjustments to viscosity and the strength of the upper weak layer (UWL) also affect compressive stress.

I then show the combinations between slab age and UWL strength in a mantle of 'medium' viscosity ($1x10^{22}$ Pa.s, Fig. 2.5), to see the resulting effects on compressive stress in the OP. I then display results from the implementation of phase changes occurring at the 660 km depth mantle transition zone (MTZ) to present how slab morphology effects overriding plate stresses. Finally overriding plate thickness variations were modelled to see their effects, with a final model combining parameters so as to reach the highest OP compressive stress while preserving morphology.

3.1 General modelled subduction dynamics

The basic subduction process is highlighted using the default model which has a medium viscosity lower mantle ($1x10^{22}$ Pa.s; Fig. 2.5), a medium strength upper weak layer set at $2x10^{20}$ Pa.s and a 40 Myr old slab. The default setup description can be found in section 2.4 with schematic from Fig. 2.1 of the same section. Temperature profile of the upper and lower mantle can be found in Fig. 2.3, with mantle viscosity conditions in Fig. 2.5.

The slab tip is initially situated at 300 km depth into the upper mantle, just less than half its depth. As subduction occurs, the slab begins to descend into the lower viscosity upper mantle with gravity driven slab sinking that drags the subducting plate towards the trench at the surface while also allowing the mid ocean ridge to remain active and diverging. Slab sinking is then affected as it approaches the stiffer lower mantle at the 660 km mantle phase transition. This reduces the slab sinking velocity.

Where denser and older slabs continue to subduct, their dip angle increases. This may enable collapse into the asthenosphere and retreat towards the spreading ridge. This known as slab rollback and along

with convecting currents that diverge at the spreading ridge and converge at the mantle wedge, contributing to the forces that move plates around, thereby creating tension or compressive stresses to be discussed later. The evolution of the subduction process is shown in figure 3.1. in the default model setup.

It is from this set up that parameter sensitivity can be explored for mantle viscosity, slab age and UWL strength so as to examine the state of stresses acting on the overriding plate.

Figure 3.1. depicts a white line at 20 km depth in each image, where a profile displaying either positive or negative horizontal deviatoric normal stress is extracted from, to ascertain whether the plate is in either compressive or tensional stress.

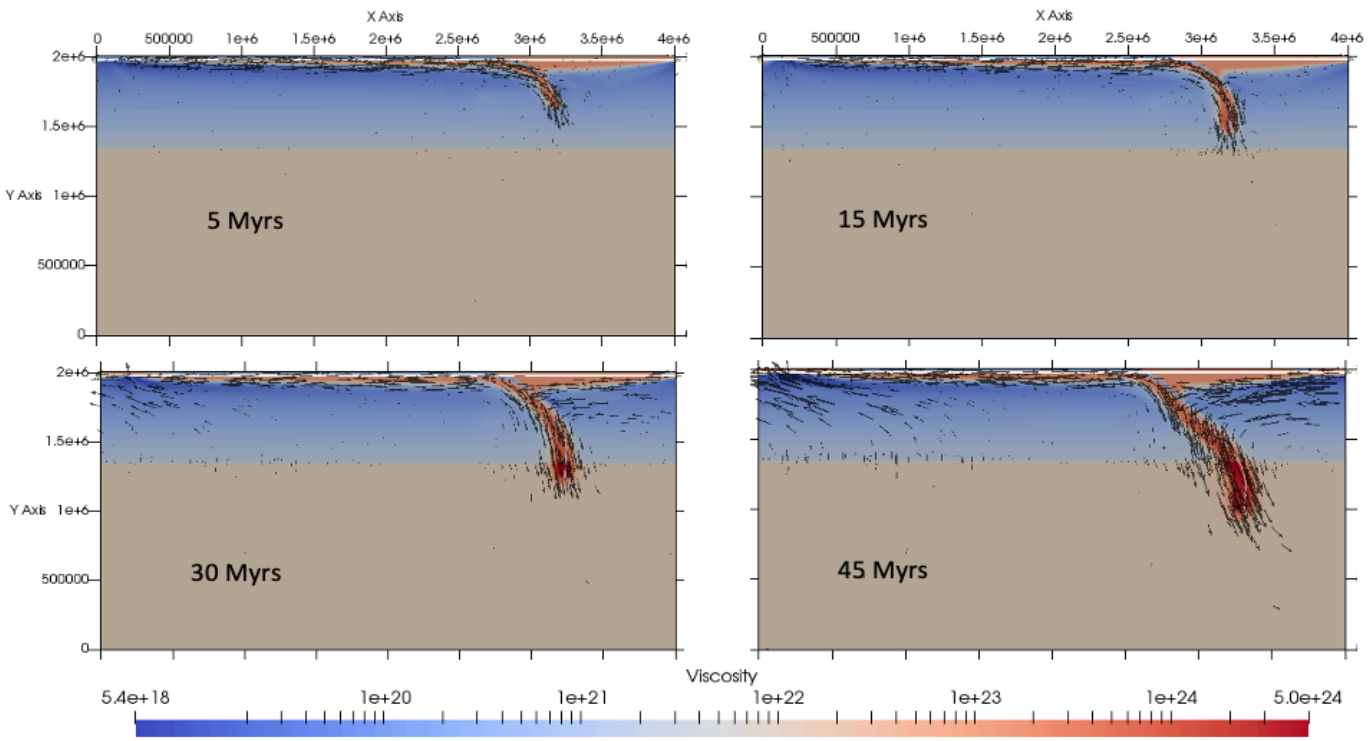

Fig. 3.1. General subduction behaviour: gravity-driven sinking of the slab and interaction with MTZ at 660 km, scale in metres. Coloured blue to red shows differing viscosity between upper and lower mantle. Arrows indicate velocity field. White line at 20 km depth indicating where profile along the x-axis data has been extracted.

Figure 3.2 displays a range of stresses on the y-axis of the plot. The left side of the plot between 0 and 500 km for each time interval shows some variation with two positive value spikes indicating the position of the spreading ridge. As material spreads out from the productive plate margin, the plate moves away from the relatively fixed position of the ridge itself due to the slab sinking, causing extension.

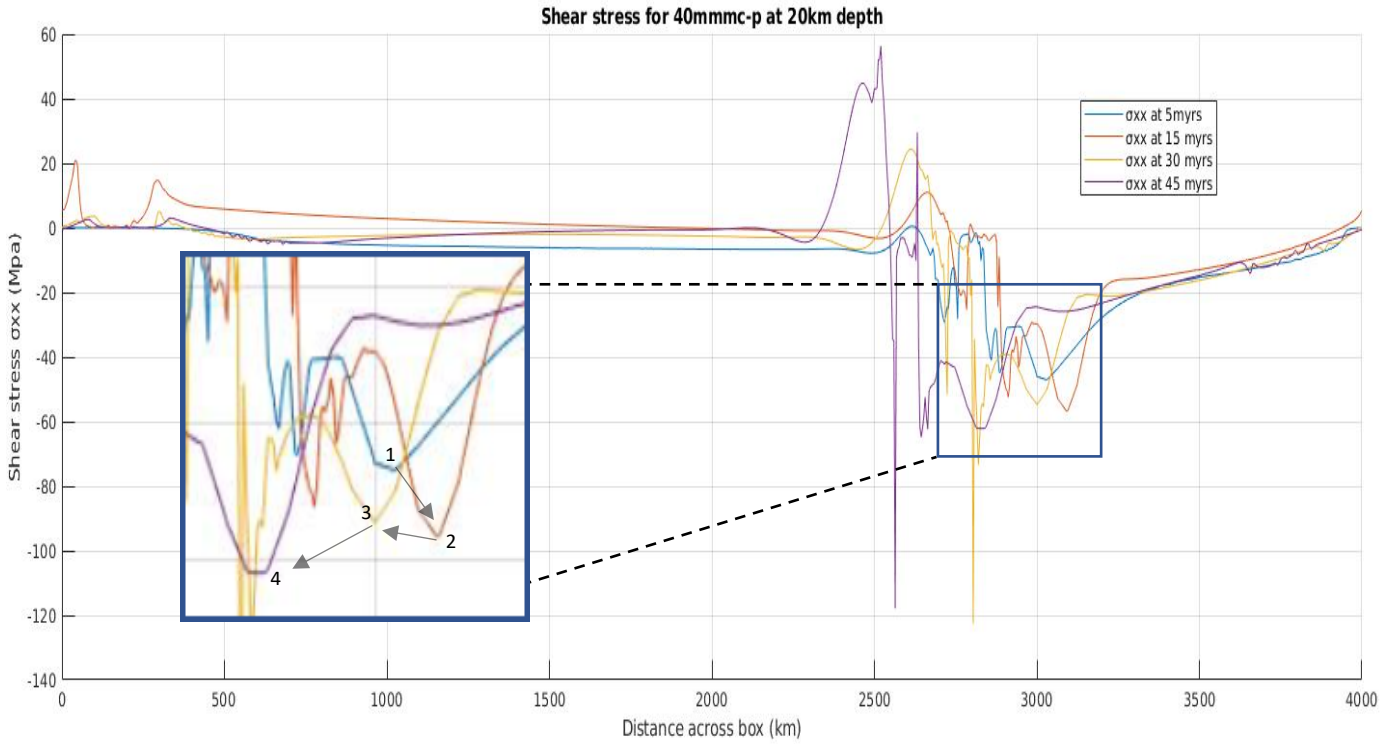

*Fig. 3.2. Deviatoric horizontal normal stress profile at 4 timesteps above in Fig. 3.1 at 20 km depth from surface (white line at top of each image). Positive shear stress readings to indicate extension, with negative to indicate compressive stress. Main focus on near curved troughs at ~300 km east of the trench in the region east of 2500 km point on x-axis within black box, showing compressive stress expressed as negative value. The slab initially shows trench advance for 15 Myr (*timestep *1 to* timestep *2 in zoomed section), then rolls back with slight decrease in compressive stress after 30Myr (point 3), finally increasing compressive stress after 45Myr at point 4.*

The flatter region between 500 and 2250 km is the subducting plate (SP), which shows little horizontal stress variation. The SP stresses remain fairly smooth given that there are little dynamics inside the plate. Variation in stress on the SP will occur however due to the rate at which the slab descends. At time 5 Myr and 15 Myr for example, the slab changes from a negative compressive value, to a positive extension value. This is minor and may be controlled by the drag of the convection acting on its underside.

As the SP starts to approach the trench, it starts to bend and dip. This 'flexure' causes the strongly extensional reading seen between 2250 and 2575 km (Fig3.2). The highest peak for each time interval can be seen within this region. Adjacent to this, there is a region where ASPECT encounters numerical artefacts where the cross section passes material interfaces. These were discussed in section 2.4.3 and in Fig. 2.6.

The points highlighted in the inset of figure 3.2. show the point of maximum compressive horizontal deviatoric stress in the OP plate. The changing position though time – indicated by the numbers – show that the slab initially rolls forwards, but then begins to move to the left of the plot. This is due to the slab rolling back as subduction continues, with the remainder of the plot showing the OP. This too moves in the direction in which rollback occurs.

It is this concept of deviatoric stress on this 20 km depth profile with which I will be investigating how parameters alter the value of this region of the overriding plate (OP).

3.2 Parameter sensitivity in default models

Next, we varied the following parameters: slab age from 30, 40, 50, 60, 70 and 80 million years, implemented 3 viscosity profiles (Fig. 2.5), 3 upper weak layer (UWL) strengths set at $1x10^{20}$ Pa.s (weak UWL) $2x10^{20}$ Pa.s (medium UWL) and $4x10^{20}$Pa.s (strong UWL) and either included/excluded phase changes. This amounted to 108 default models for interpretation that showed trends between parameters, pairing of those parameters and their effects as well as dominant causes for compressive stress in the overriding plate.

In order to categorise models by these parameters and their values, I devised a model name convention in order to distinguish between them. This convention has been used throughout this thesis and has been explained using the example below.

This simple convention highlights the age of the slab, the viscosity of the mantle, the strength of the UWL and whether the model either incorporates a mantle phase transition at 660 km depth.

$$40mmmc - p$$

In this example, the *40* at the front of the model name represents the slab age. This could be 30, 40, 50, 60, 70 or 80, with the age in Myr.

Next, the mantle conditions are described with *mm* denoting a medium mantle. This could also be *wm* or *sm* to represent a weak or strong mantle respectively. These 3 mantle viscosity profiles can be seen in Fig. 2.5.

Following this, *mc* represents the strength of the upper weak layer or the 'crust'. In this instance, the model would have a medium strength crust, but could also be weak or strong, which would be written as wc or sc respectively. Their viscosities have been listed at the beginning of this section.

Finally, *-p* indicates that this model does not have a mantle phase change incorporated into this particular model. Should one have been implemented, the notation used would be *+p* as the suffix. This notation has been listed in Table 3 below.

Slab age = 30, 40, 50, 60, 70, 80 (Myr)	
Without phase changes	With phase changes
wmwc-p	wmwc+p
wmmc-p	wmmc+p
wmsc-p	wmsc+p
mmwc-p	mmwc+p
mmmc-p	mmmc+p
mmsc-p	mmsc+p
smwc-p	smwc+p
smmc-p	smmc+p
smsc-p	smsc+p

- Prefix denoting the slab age (Myr)

- Suffix including/excluding phase changes (-p/+p)

Mantle Viscosity

wm = 'weak mantle' (5 x 10^{21} Pa.s)

mm = 'medium mantle' (1 x 10^{22} Pa.s)

sm = 'strong mantle' (2 x 10^{22} Pa.s)

UWL strength

wc = 'weak crust' (1 x 10^{20} Pa.s)

mc = 'medium crust' (2 x 10^{20} Pa.s)

sc = 'strong crust' (4 x 10^{20} Pa.s)

Table 3. Model name convention. By varying each of the models in this way, a total of 108 total default set up models have been generated, with their respective parameter values noted and used in this way for the rest of this thesis.

I will begin by describing the model results showing the effect that slab age has on OP compressive stress, so as to support the correlation from Scott (2018). This is followed by an investigation into mantle viscosity variations, as this effects how efficiently slabs are able to descend into the mantle.

Following this, the combining of slab age and mantle viscosity has been explored. This has been conducted to see how descent into the mantle is affected by introducing slab density variations from

altering the slab age. I sought to see if similar stresses in older slab models could be exerted from younger slab models if mantle viscosity was reduced.

In a similar sense, I also explored the UWL strength in conjunction with mantle viscosity. By altering the coupling at the trench rollback could be controlled, so when coupling with rate of descent into the mantle I hoped to see if coupling together with descent was an important pairing of parameters with respect to OP compressive stresses.

Slab age and UWL strength was then explored form the results. Coupling at the trench varies in reality as does slab age. By exploring these two parameters together, I was able to investigate how come similar latitudinal variations seen in reality could be better understood in terms of their formation.

A brief overview of the effects of introducing a mantle phase transition is then presented. This was not a sole focus of this thesis, so as such the effects of morphology were primarily explored. However, compressive stresses are seen in Fig. 3.16 and display small variations.

Next, the vertical distribution of stresses in an OP of either 50 km or 100 km was investigated, as well as how the density of thicker Ops altered the stresses directly.

Finally, with all parameters considered and to highlight the correlation from Scott (2018), their combined effects were analysed. This was with respect to generating a morphology suited to developing a large convection cell which is thought to further add to compressive stresses (Holt et al. 2015).

3.2.1 Slab age effect on compressive stress in the overriding plate

Here slab age has been varied in 10 Myr intervals from 30 to 80 Myr. The results show that when varying the slab age compressive stresses are affected. The rate of compressive stress as indicated by negative values ($-\sigma_{xx}$), which we interpret as contributing to tectonic shortening and therefore crustal thickness (Sections 1.3, 2.4.3).

By using a 20 km deep horizontal profile in each of the models (as in Fig. 3.2) the amount of stress across the box can be assessed, so the effect of altering slab age can be assessed. By doing so, we see a systematic shift between each of the curves presented, with the 80-Myr old slab model showing the highest negative σ_{xx} value in the OP.

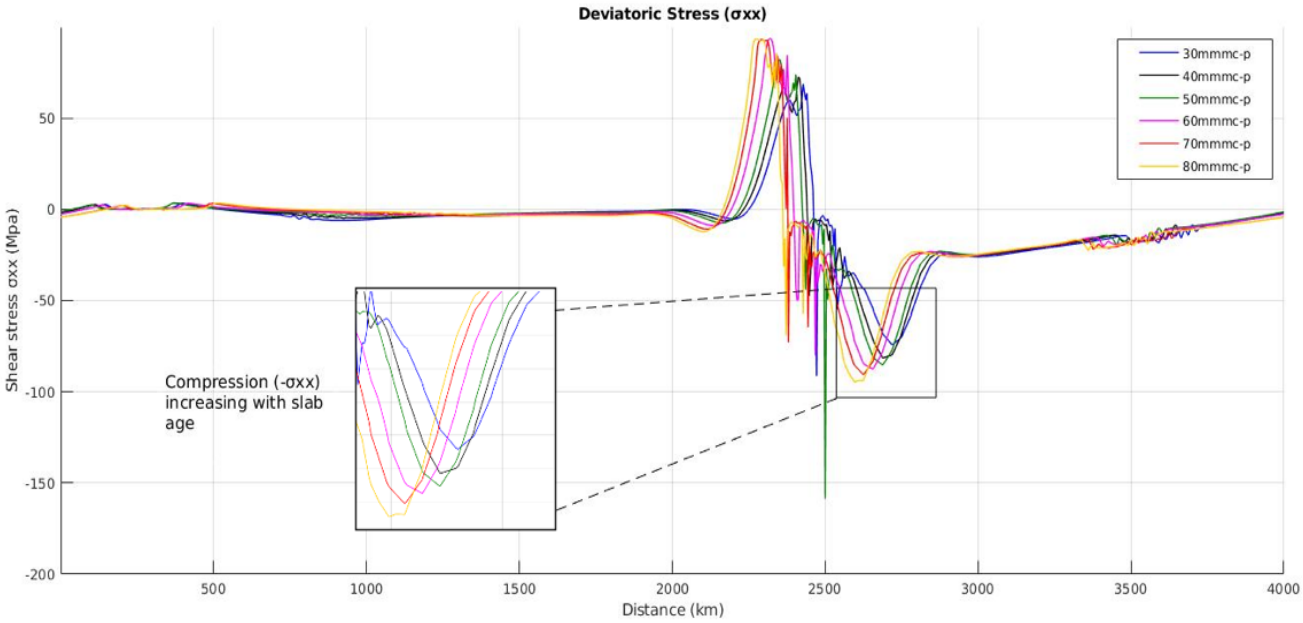

Fig. 3.3. Comparative plot of 'mmmc-p' (or medium mantle, medium crust/UWL with no phase changes, see model list in supplementary material at the end of this thesis) models with slabs of varying age between 30ma and 80ma. Major features such as viscosity, weak layer competence and phase changes all of constant value though showing age ordered negative deviatoric stress in the OP. 60 Myr of subduction elapsed, with key region in black box showing troughs arranged in age order, with greatest compressive stress generated in oldest slab. Stress profile taken at 20 km depth.

Results suggest that the older slab models exhibit higher compressive stresses in this region of the OP, as well as having physically moved this point of high compressive stress in the OP to the left of the plot. This left shift indicates slab rollback, where the OP has shifted in response to the rolling back of the denser and older slabs when compared to younger slab models.

These results indicate a positive correlation between slab age and compressive stress in this region of the overriding plate, as noted by a marked increase in the deviatoric stress or $-\sigma_{xx}$ value, while there is also an increase in convective vigour beneath the overriding plate with increasing slab age.

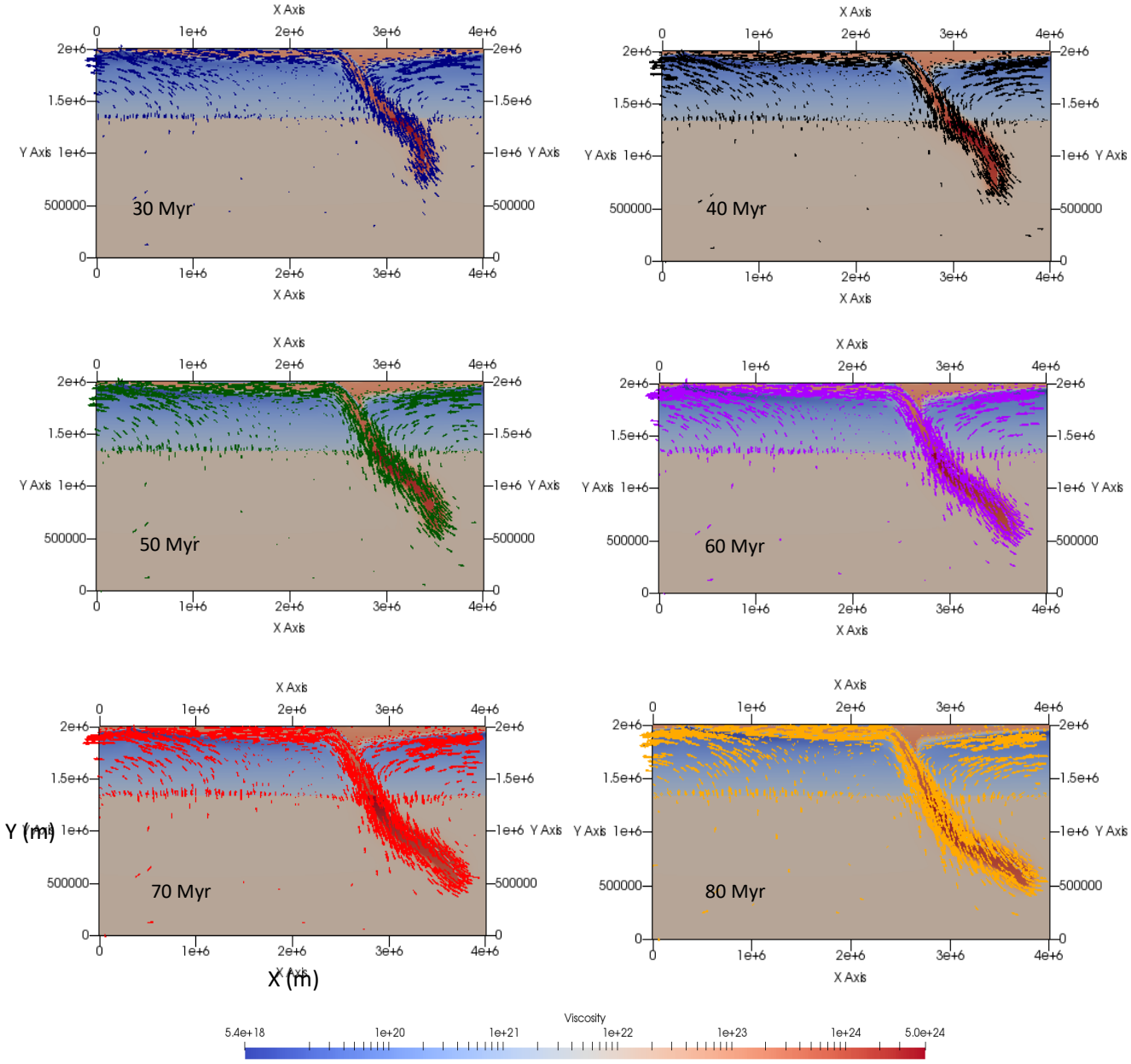

Fig. 3.4. Illustration of the increased convection driven by differing slab age after 60Myr of subduction. The greater amount of subduction past the transition zone draws in the mantle material and overriding plate in the upper 660 km increasing compressive stress. Plotted using viscosity differences to indicate the plates at higher velocity than the low velocity mantle material, in this instance with colouration to match Fig. 3.3 temperature driven vector arrows to distinguish between models and highlight convecting currents.

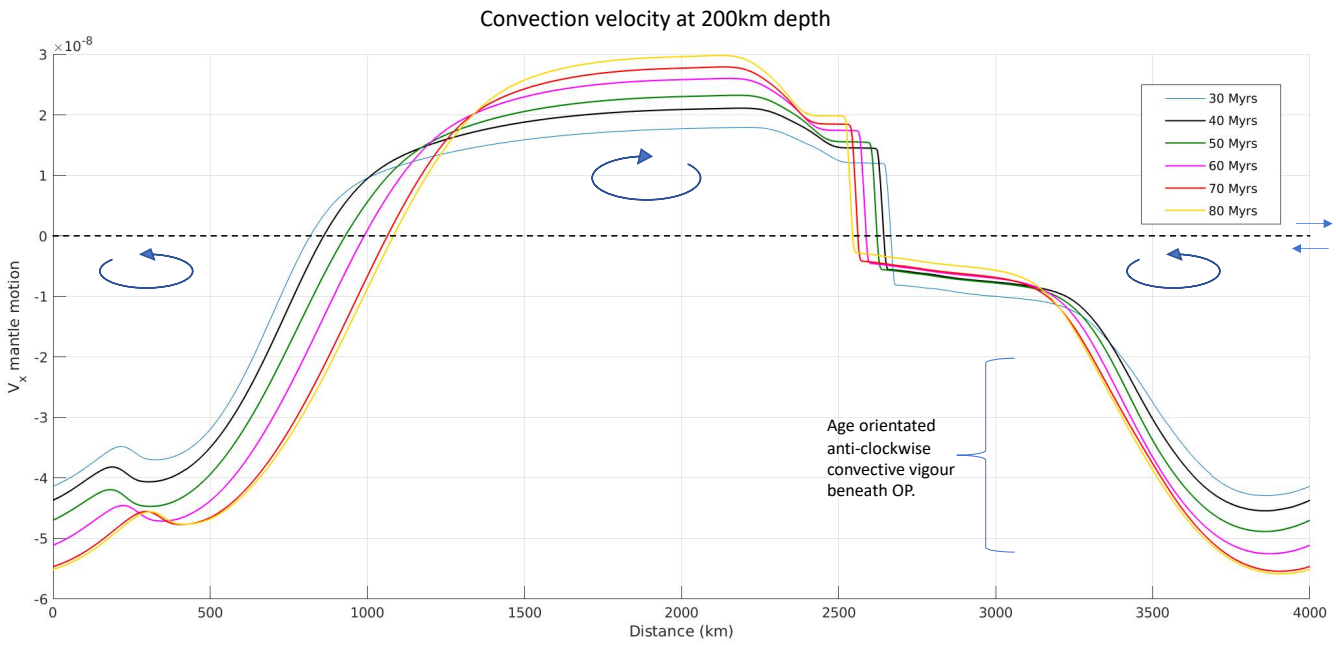

Fig. 3.5. Profile at 200 km depth showing horizontal velocity (cm/yr) of convecting currents at of 60 Myr. Negative numbers correlate to left directed convection, positive numbers are right directed on horizontal axis (dashed line). Comparison between models differing in slab age with colours to match each model (as in 3.4). Age determined anti-clockwise convection increase at 2500 km (trench location).

Each of these models shows a different depth of slabs at the same 60 Myr interval (Fig. 3.3 and 3.4), while also exhibiting aged ordered convective vigour increase east of the trench at ~3250 km on the x axis (Fig 3.5.). While compressive stress is also higher in the older slab models (Fig 3.3.) the increased convective vigour and bulk density dependent slab sinking rates must contribute in concert to deliver higher OP compressive stress.

This correlation between convective vigour and slab age remains near constant throughout the models, with results from other models being offset in some instances where slab morphology affects the vigour of the convecting current. Flexibility of younger slabs appears greater in that their rheology allows them to be shaped by the surrounding mantle and its dynamics. Older and less flexible slabs appear to resist as much physical change, and as such remain rigid upon descent (Fig. 3.4). The latter of these two causes more roll back, which may be symptomatic of greater OP compressive stress.

These results illustrate that increased total rollback corresponds to higher compressive stress in the OP. Descent into the lower mantle as controlled by the slab's age dependent bulk density, subsequently results in an increase in convective vigour as seen in figure 3.5. This increase in roll back and greater slab depth appear across all models where OP compressive stress is higher.

3.2.2 The role of mantle viscosity on the dynamics of the subduction process

Altering mantle viscosity exerts the strongest control over stresses in the overriding plate in the models (Fig. 3.6). By reducing mantle viscosity to its weakest configuration (see methods Fig. 2.5), compressive stress comparatively increases in the OP. Reducing mantle viscosity reduces resistance

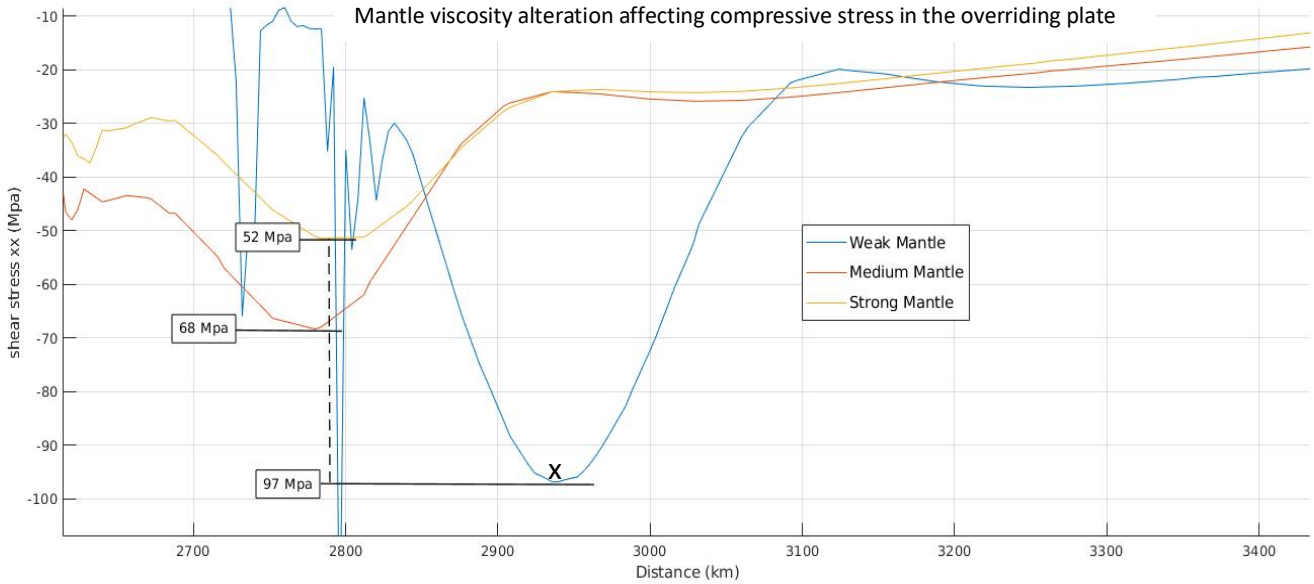

Fig. 3.6. Profile at 20 km depth showing differing amounts of compressive stresses acting on the overriding plate as dictated by mantle viscosity. OP Compressive stress doubles between a strong and weak mantle viscosity. Models used are 40 Myr old slabs and a medium strength upper weak layer and no phase changes. This feature is consistent across all models. Average trench position at 2600 km. Captured after 50 Myr of subduction, with point x marking point of maximum compressive stress.

to slab descent. If coupled with an older/denser slab, slabs will sink faster. This appears to have an effect on the subsequent stresses. The faster a slab descends the higher the compressive stress in the overriding plate, which may be controlled by the convective vigour and shear drag beneath the OP.

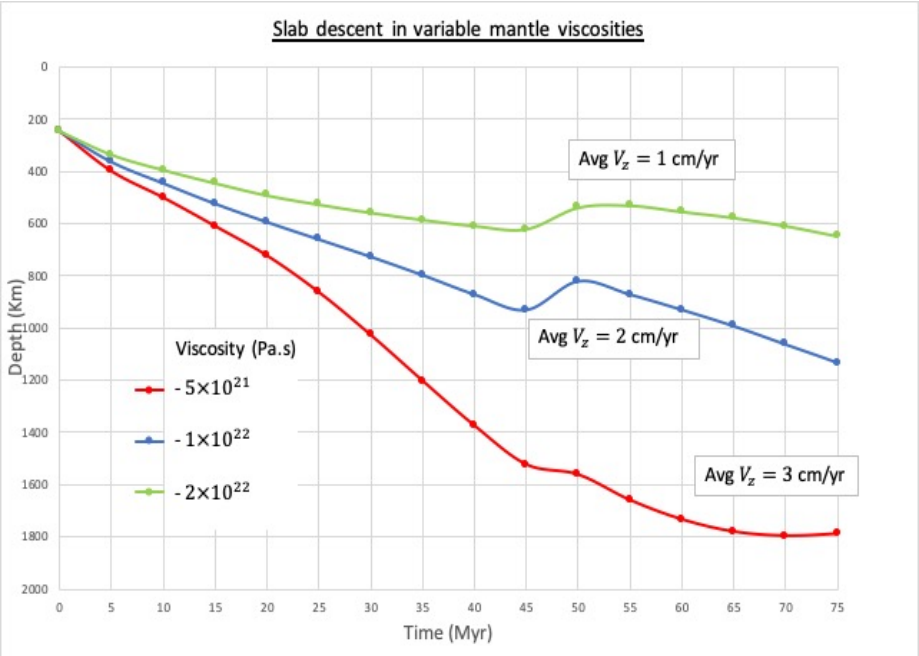

Fig. 3.7. Slab tip depth through time giving a rate of descent (average vertical velocity). Slabs 40 Myr old and have same bulk density, descending into varied mantle viscosities (from Fig.2.5.) and equal upper weak layer strength.

It is this rapidity of slab descent into a less viscous mantle that leads to the greatest compressive stress in the overriding plate in the models. When creating a greater density contrast with older slabs in a less viscous surrounding mantle, this descent becomes more rapid, increasing compressive stress up to 90 Mpa within 15Myr.

3.2.2.1 Control of slab age in conjunction with mantle viscosity

In this section, I will explore the combination of mantle viscosity and slab age, in order to see how slabs descend and the resulting effects to the OP compressive stresses. The models show the strongest compressive stresses in the OP when slab age is set to its maximum at 80 Myr, descending into a reduced viscosity or weak mantle configuration (Fig. 2.5). Slabs at 40 Myr of age show relatively lower compressive stress in the same mantle setting.

The models set in a low viscosity mantle exhibit high OP stress at early stages of subduction, in this case exhibited in the 80 Myr slab model reaching 104 MPa within 35 Myr, after which compressive stress continues to rise up until 50 Myr where it reduces more rapidly than the 40 Myr slab model (Fig. 3.8.). This point of highest compressive stress arrives later for slabs of reduced ages, which is reflected in the slab sinking velocities.

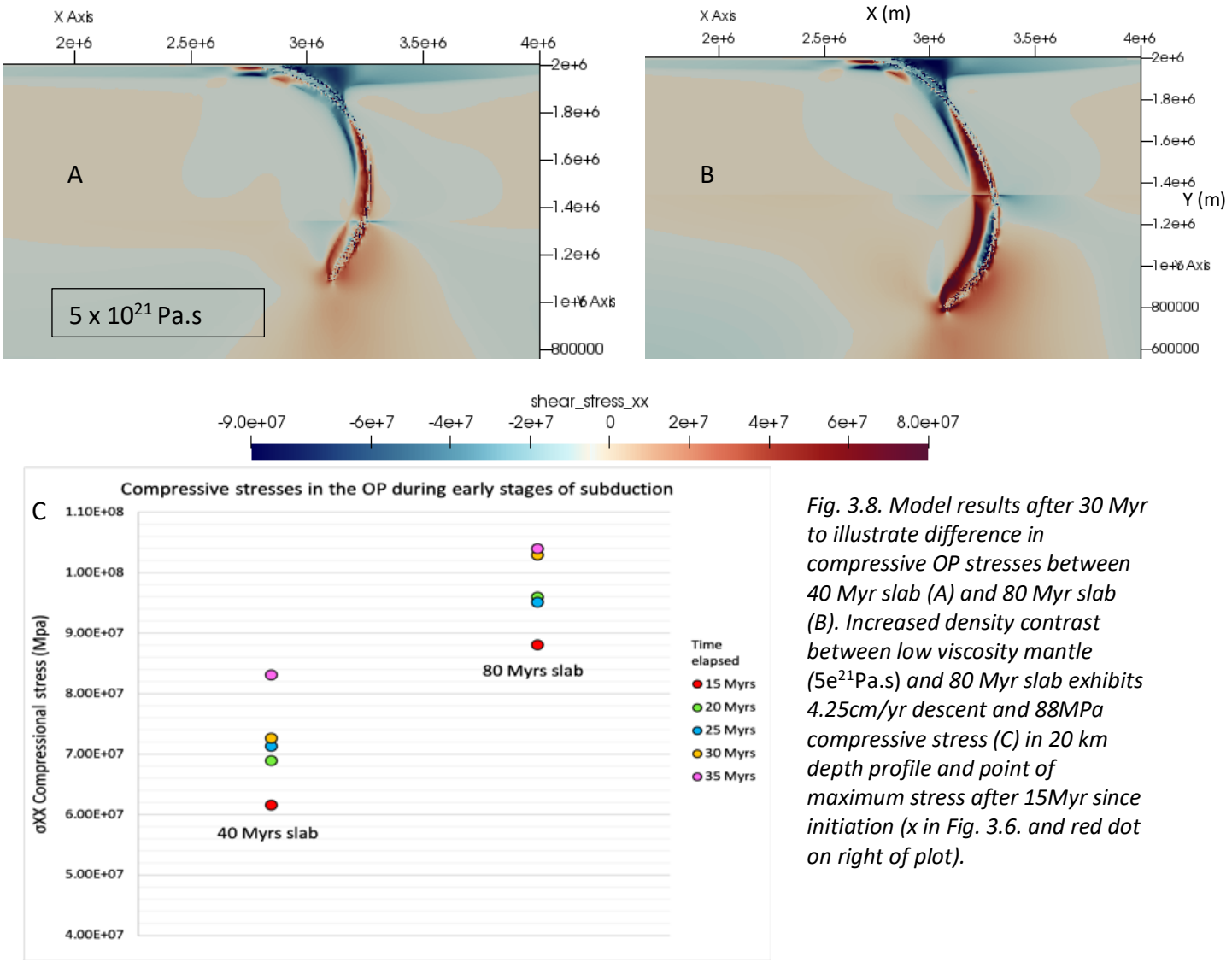

Fig. 3.8. Model results after 30 Myr to illustrate difference in compressive OP stresses between 40 Myr slab (A) and 80 Myr slab (B). Increased density contrast between low viscosity mantle (5e^{21}Pa.s) and 80 Myr slab exhibits 4.25cm/yr descent and 88MPa compressive stress (C) in 20 km depth profile and point of maximum stress after 15Myr since initiation (x in Fig. 3.6. and red dot on right of plot).

In general, the sinking velocity of older slabs is greater compared to younger slabs in any mantle viscosity. In this weak mantle setting, 80 Myr slabs exhibit up to 5.5 cm/yr within 35 Myr, while the 60 Myr slab model reaches a maximum just over 5 cm/yr, but 5 Myr later. Reducing slab age to 40 Myr reduces further still to 4.4 cm/yr at 40 Myr (Fig 3.9.). This matches the initially high OP compressive stress in figure 3.8, highlighting sinking velocity as a key component to high OP compressive stress.

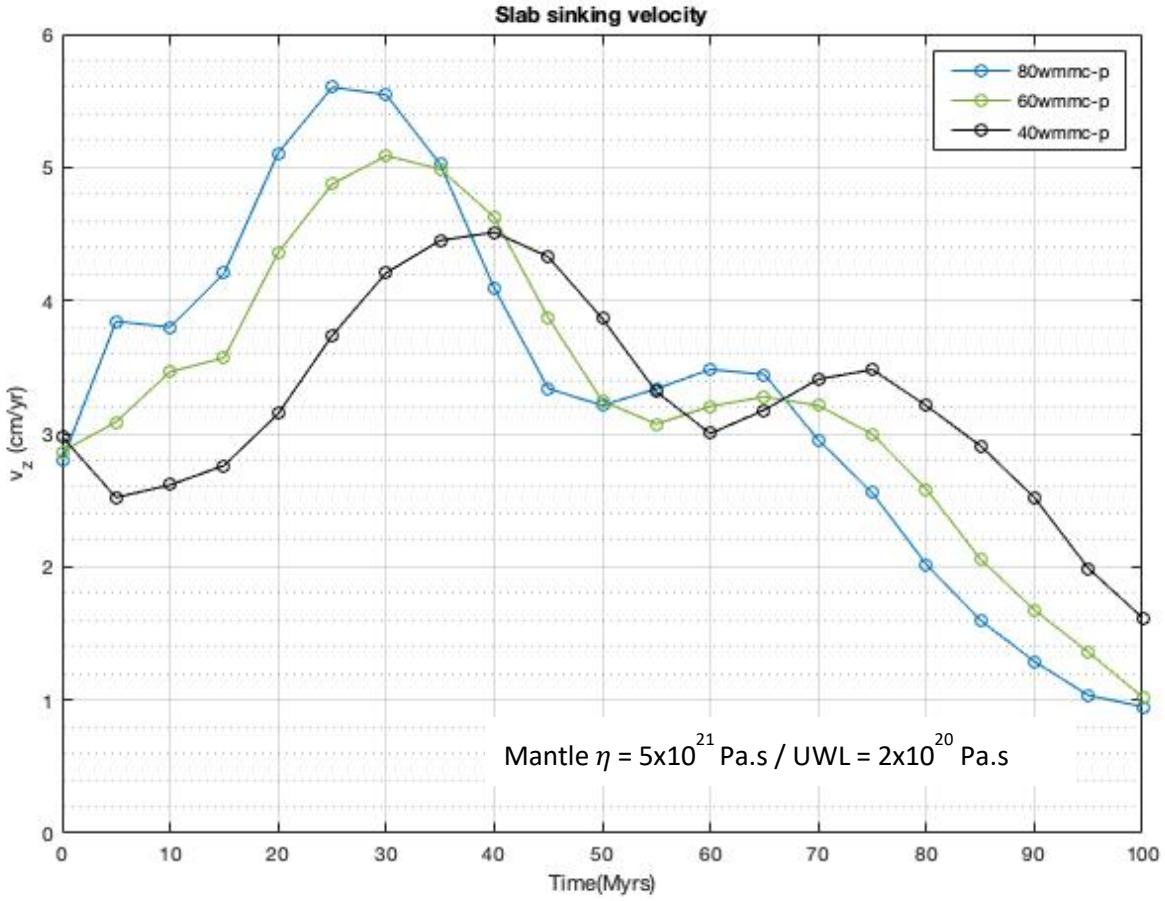

Fig. 3.9. Sinking velocity (cm/yr) of slabs with ages of 40, 60 and 80 Myr with same weak mantle configuration and UWL strength. Rapid sinking velocity at early stages highlights initial peak of OP compressive stress driven by increased slab age, where 40 Myr slabs exhibit 60 MPa, while 80 Myr models exhibit 88 MPa after 15 Myr (3.8). Low point at 50, 55 and 60 Myr for each model respectively indicates point at which slabs hit the bottom of the box, with each of the models exhibiting slab dip angles over 60˚ and curling forwards (as in Fig. 3.8.B.).

It is also possible for younger slabs to create higher rates of OP stress than older slabs by reducing mantle viscosity (Fig. 3.10.). The models suggest that the effect slab age has over the stresses generated remains a smaller factor when compared to a less viscous and hotter mantle.

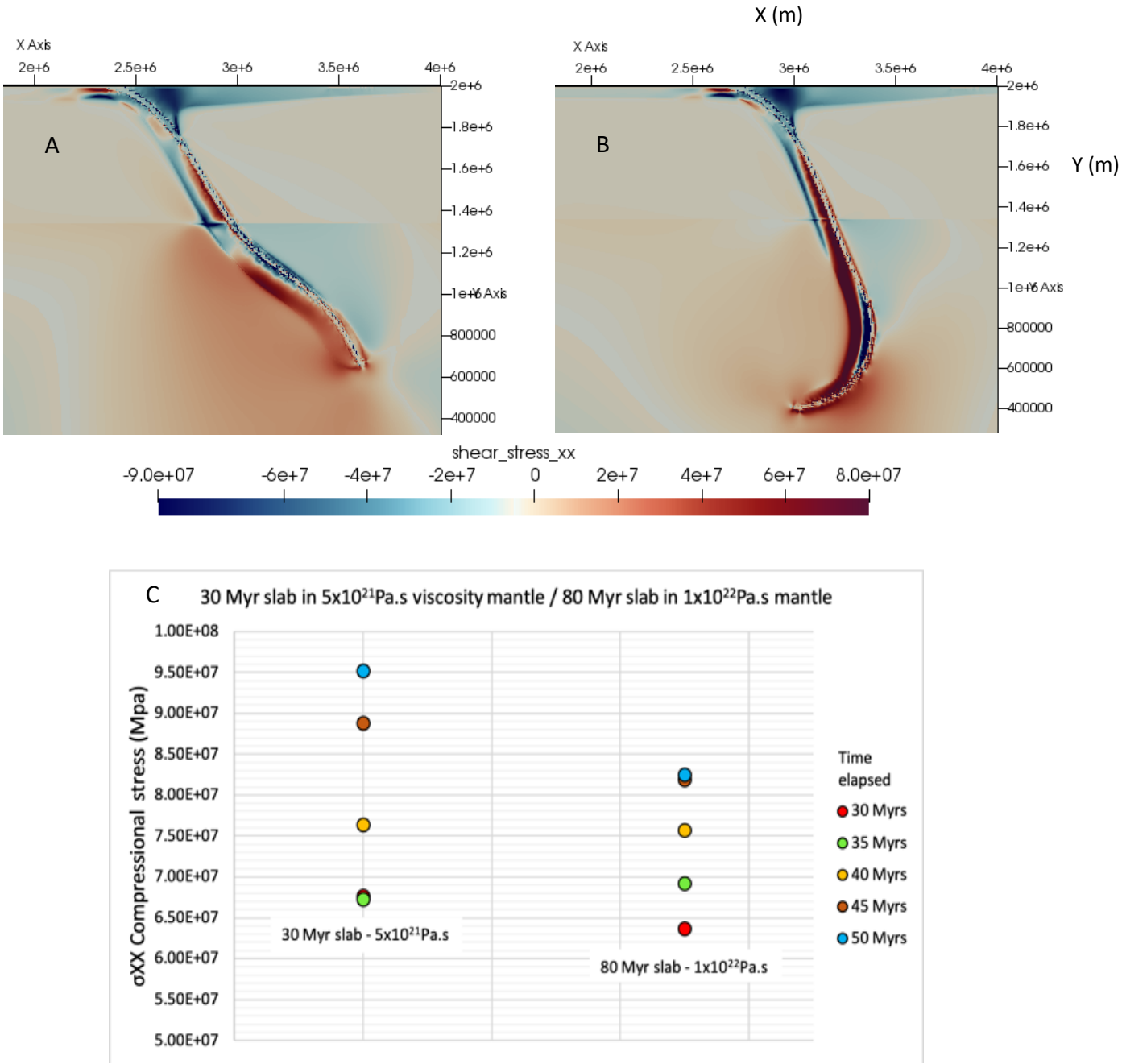

Fig. 3.10. Comparison between an 80 Myr old slab in a medium viscosity mantle (A) and a 30 Myr old slab in a low viscosity mantle (B), with comparison taken from profile at 20 km depth to show differences in compressive stress generated from this effect through time (C). Both models contain an upper weak layer of equal and medium strength (2x10^{20}Pa.s). Both images after 50 Myr of subduction (blue dots).

Maximum sinking velocities for each model here shows 4 cm/yr for the 30 Myr slab in a weak mantle at 45 Myr, with the 80 Myr medium viscosity model showing a reduced 3 cm/yr sinking velocity at 50 Myr. Medium viscosity mantle models show a gradual incline and reduction in sinking velocity, where the weak mantle models although showing a sharp peak early in subduction, also reduce their rate of sinking at a far faster rate.

The models indicate that a reduced viscosity mantle generates the highest compressive stress in the OP and by increasing slab age, the increased density of the slab sinks faster in the low viscosity mantle. This increase in descent creates subsequent compressive stress increase in the overriding plate.

3.2.2.2 Upper weak layer strength effects in different mantle viscosities

I imposed an upper weak layer (UWL) strength (Fig. 2.1) varying with a viscosity of $1x10^{20}$Pa.s (weak UWL), $2x10^{20}$Pa.s (medium UWL) or $4x10^{20}$Pa.s (strong UWL). Adjusting this UWL strength causes higher or lower friction at the trench, resulting in greater coupling with an UWL of increased strength, or reduced coupling if UWL strength is lowered. In this way, OP stress and slab morphology can be influenced and is shown in Fig. 3.11 (next page).

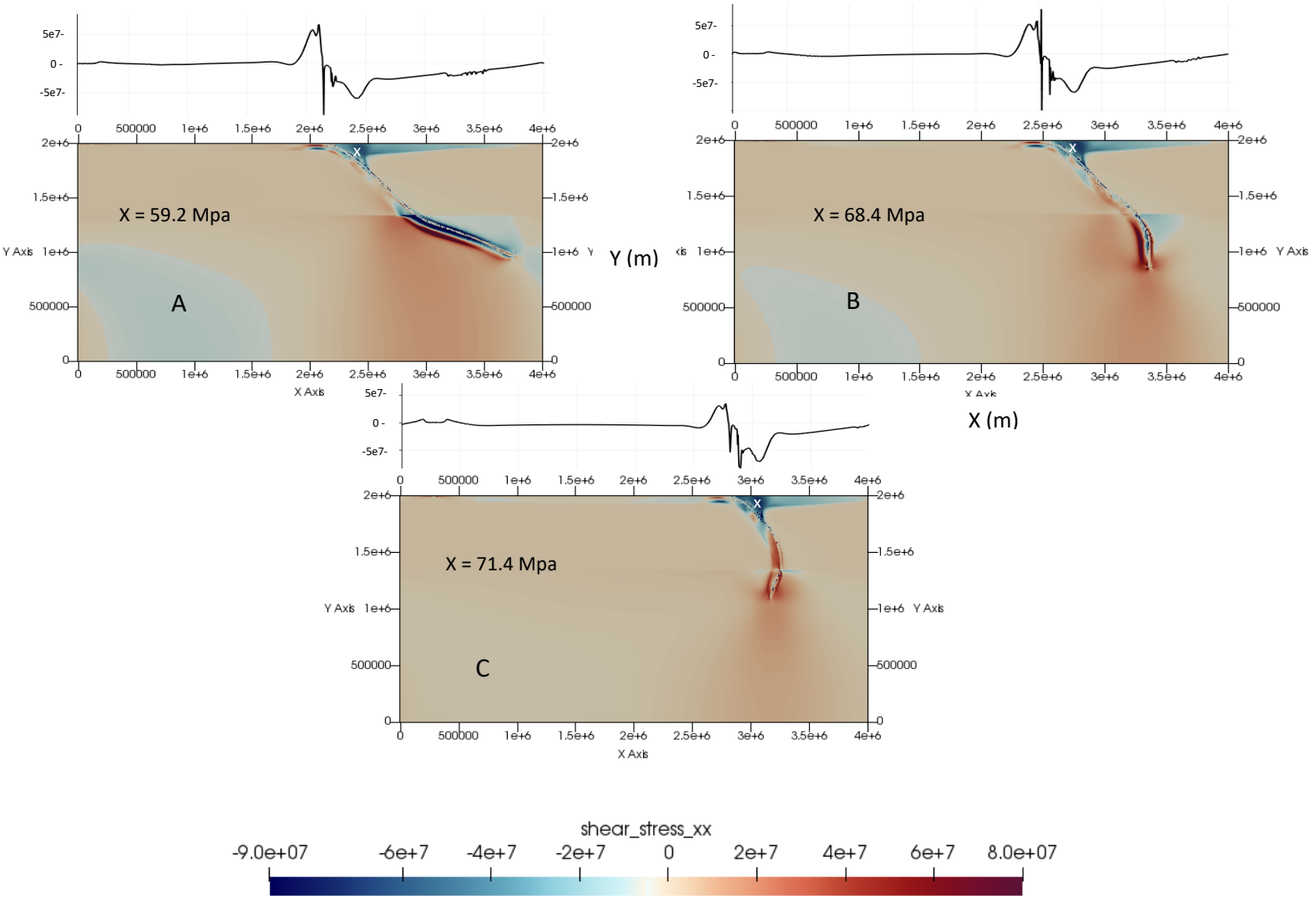

Fig. 3.11. Shows 3 different UWL strengths. Strength decreases from C to A (A<B<C). All models have 40 Myr old slab and set in a medium strength mantle profile (1x10^{22}Pa.s). Timestep taken from 50 Myr of subduction, with profile at 20 km depth. X displays point of maximum OP plate compressive stress, which increases with UWL strength and is the point at which data for orange lines in Fig. 3.12 were extracted from the model calculations.

When increasing UWL strength, coupling at the trench increases from higher friction and compressive stress in the OP generated by a 40 Myr old slab can almost reach 80 Mpa within the first 10 million years (Fig. 3.12). Slabs increase their dip angle up to ~70˚ and advance towards the overriding plate, which causes an initial increase in OP compressive stress from this coupling between the two plates.

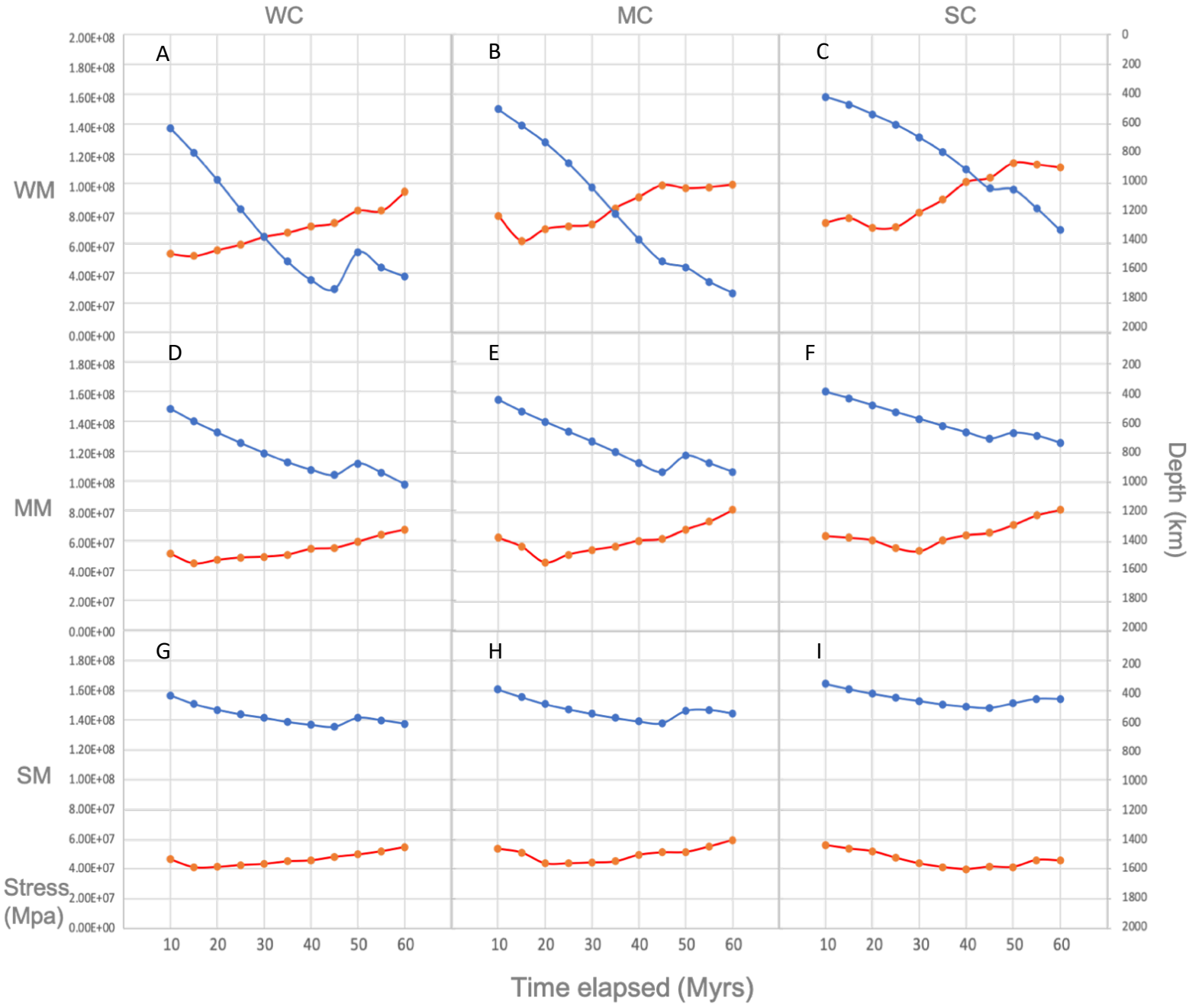

Fig. 3.12. Slab tip depth (blue with right axis in km) and compression in the overriding plate (orange with left axis in MPa) against time in Myr. WM, MM, SM = weak, medium and strong mantle; WC, MC, SC = weak, medium and strong crust (UWL) – see Table 3. Enables all combinations to be shown.

Overall, UWL strength exerts control the rate of slab descent into the mantle by inducing higher or lower friction at the trench. This is seen in the WM models (Fig. 3.12 A, B and C), where model wmwc displays slab descent up to 4.5cm/yr compared to wmsc, reaching 2cm/yr. Each model exerts up to 100 MPa of stress in the OP, with the sc model reaching this value after 40 Myr, the mc model at 45 Myr and the wc model after 60 Myr. Each model exhibits a marked increase in compressive stress in

the OP when the slab passes the 660 km MTZ. Model wmwc passes this point between 10-15 Myr, wmmc passing between 15-20 Myr and wmsc passing at ~30 Myr.

Models D, E and F (Fig. 3.12) in the medium viscosity mantle (mm) setting show similar increases in OP stresses upon passing the 660 km MTZ, occurring from left to right between 15-20Myr, between 20-25 Myr and between 35-40 Myr, with UWL strength also increasing from left to right. Model mmwc doesn't quite reach 75Mpa, where mmmc and mmsc both do within 60 Myr.

Both mmmc and mmsc models show increase in compressive stress from 55 to 85 Mpa between 30 and 60 Myr, but mmmc began a marked increase from 45 Mpa after 20 Myr. This is the point at which the slab tip descends past the 660 km MTZ.

Comparatively, the models in the strong mantle setting (G, H and I) never descend past the 660 km MTZ, and as such exhibit lower compressional values in the OP. Both the smwc and smmc reach 60 Mpa after 60 Myr, where model smsc exerts 60 Mpa of OP compressive stress within the first 10-20 Myr due to initial trench advance and slab dip angle steepening.

From the control over slab descent, these changeable UWL strengths contribution to plate velocities affects slab morphology. Slabs exhibiting values greater than 60-70 Mpa of OP compressive stress within 20-30 Myr of subduction may advance up to 100 km into the OP, and as such cause unlikely form to be generated.

3.2.3. Relationship between slab age and UWL strength

The friction at the trench as determined by the material at the margin exerts strong control over the slab dip angle upon descent. This plays an important role in the overall dynamics of the system, despite stronger parameters such as mantle viscosity having a more profound effect. By exploring the varying effects driven by altering the UWL strength in conjunction with slab age, we can further investigate the correlation between slab age and compressive stress in the overriding plate, enabling us to understand processes leading to crustal thickening.

I imposed the same weak, medium and strong UWL strengths as in section 3.2.2.2, use 30 – 80 Myr old slabs in a medium viscosity mantle (see Fig. 3.7) to investigate the amount of compressive stress at point x (Fig. 3.10) through time.

A

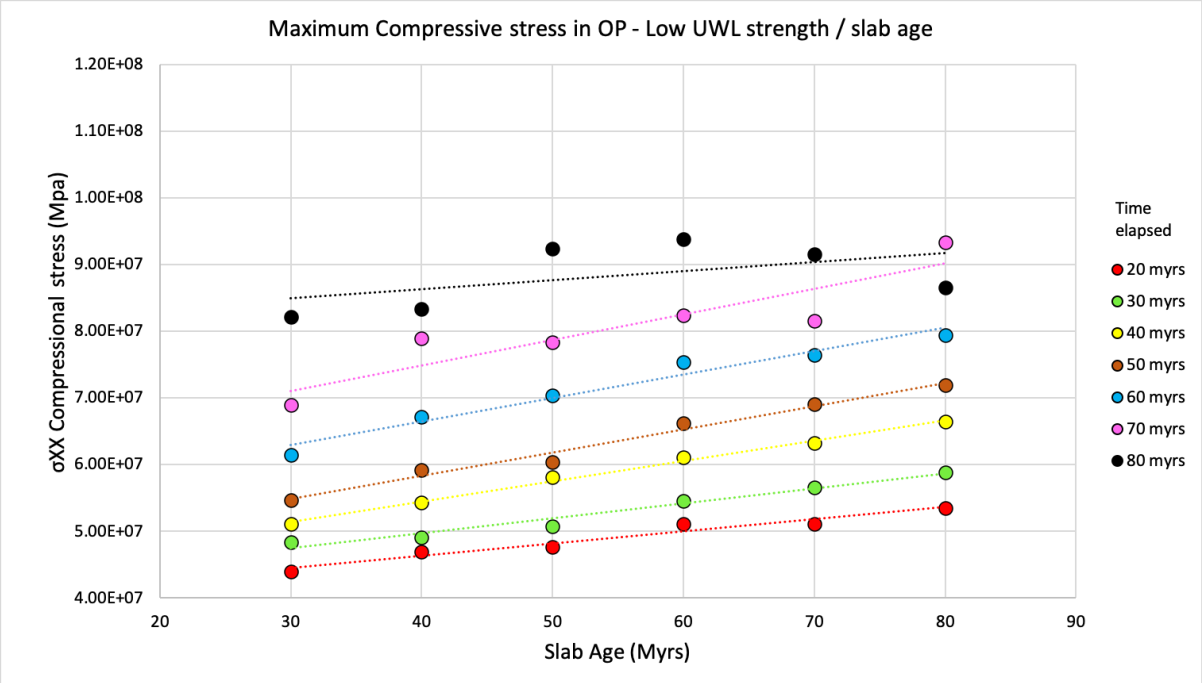
Maximum Compressive stress in OP - Low UWL strength / slab age
σXX Compressional stress (Mpa)
1.20E+08
1.10E+08
1.00E+08
9.00E+07
8.00E+07
7.00E+07
6.00E+07
5.00E+07
4.00E+07
20
30
40
50
60
70
80
90
Slab Age (Myrs)
Time elapsed
20 myrs
30 myrs
40 myrs
50 myrs
60 myrs
70 myrs
80 myrs

B

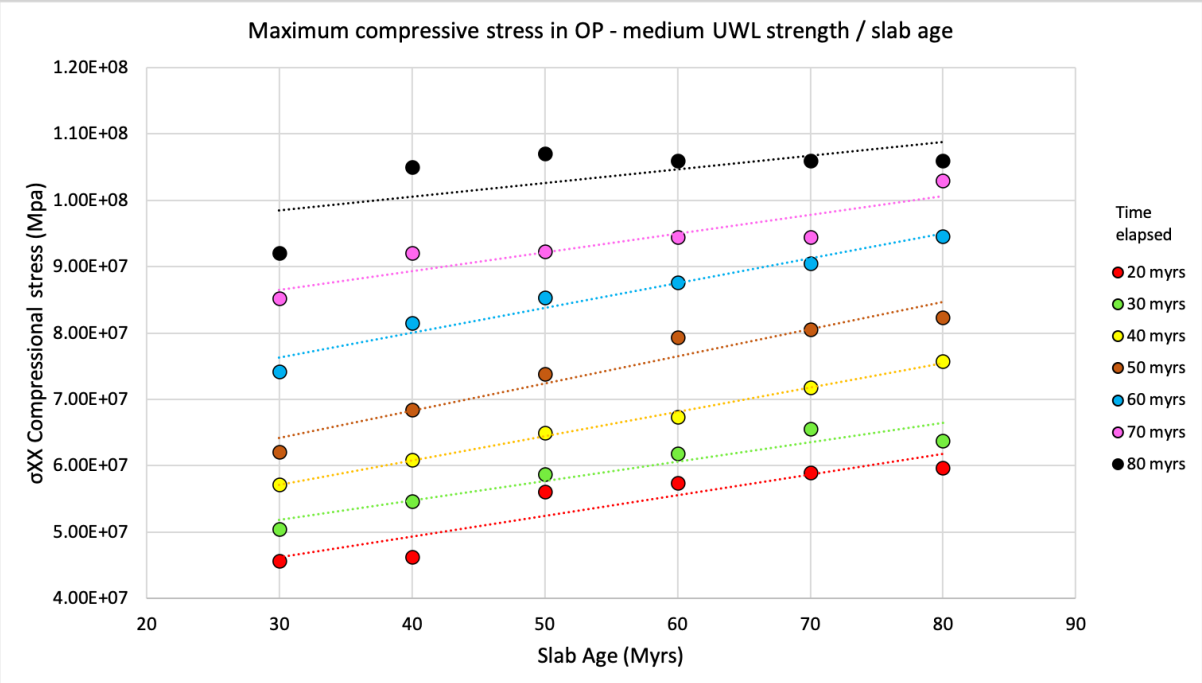
Maximum compressive stress in OP - medium UWL strength / slab age
σXX Compressional stress (Mpa)
1.20E+08
1.10E+08
1.00E+08
9.00E+07
8.00E+07
7.00E+07
6.00E+07
5.00E+07
4.00E+07
20
30
40
50
60
70
80
90
Slab Age (Myrs)
Time elapsed
20 myrs
30 myrs
40 myrs
50 myrs
60 myrs
70 myrs
80 myrs

C

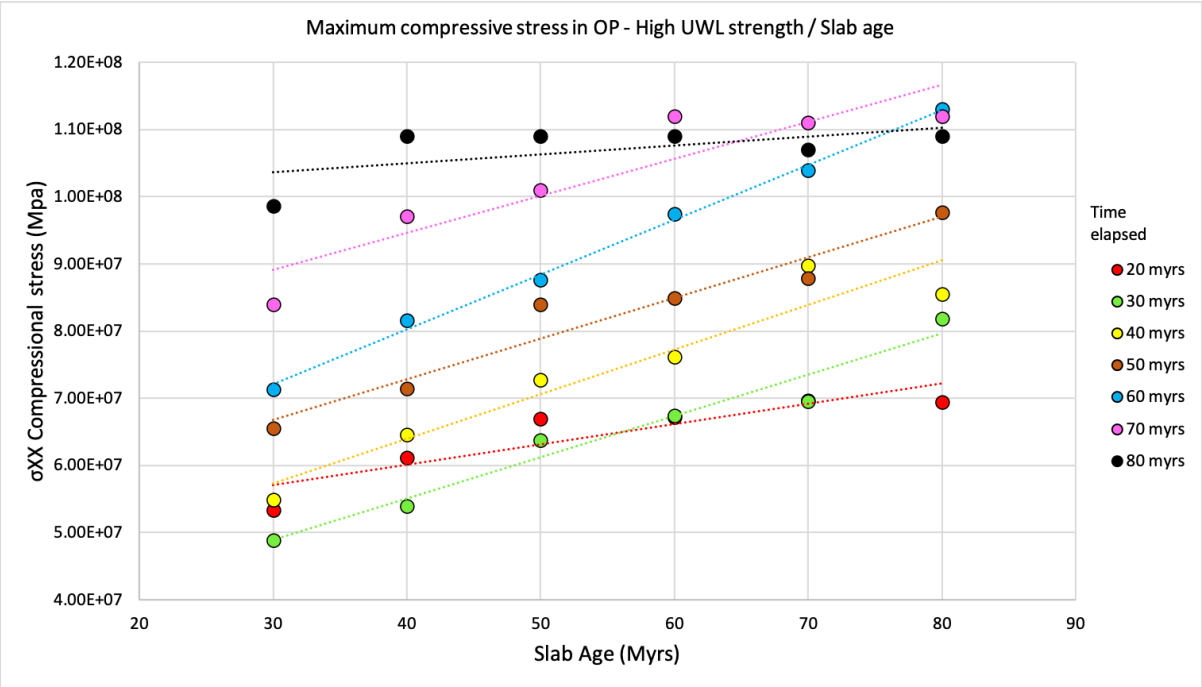

Fig. 3.13. Variable UWL strengths with compressive stress in the OP against slab age. Changing UWL and slab age through time shows the evolution of compressive stress in the OP, and the correlation between crustal thickening and slab age through compressive stress by proxy.

UWL strength variation changes OP stress values, with weak UWL accounting for low stress compared to higher values generated from increased UWL strength (section 3.2.2.2). Older slabs will typically rollback more rapidly given their increased density, where in this setting we would expect to see extension in the OP. In our models, we see increased OP stress and faster plate velocities with older slabs in the models.

As in section 3.2.1, OP compressive stress increases with older slabs, which, when combined with high UWL strength, increases further still, as highlighted by the linear trend lines. 80 Myr old slabs with a weak UWL ranges from 55 Mpa to 95 Mpa of OP compressive stress between 30 and 80 Myr, with a reduction between 70 and 80 Myr, possibly due to UWL material being of finite length (see methods section 2.4).

Using a medium UWL strength in an 80 Myr slab creates 60 Mpa to 105 MPa of OP compressive stress within the same time interval, but increasing the UWL strength further causes slabs to initially advance into the OP from greater friction at the trench, causing 70 Mpa of compressive stress after 30 Myr and reaching 110 MPa within 60 Myr.

The models also display a saturation at around 110 MPa of OP compressive stress with medium and strong UWL configurations, regardless of slab age. Slab dip angles reach above 70˚ with high UWL strength, which can result in 110 Mpa of OP compressive stress after 60 Myr for 80 Myr old slabs (blue dot Fig. 3.13 C), exhibiting a 2 – 2.3 cm/yr descent velocity until slowing to less than 2 cm/yr after 60 Myr. Younger slabs reach these OP stress values with slightly lower plate velocity between 1.9 – 2.2 cm/yr, but 10-20 Myr later.

In some cases, after 30 Myr of model time, a decrease in compressive stress can be observed in the strong UWL models. As mentioned, initial trench advance and between 55 – 65 Mpa of OP compressive stress is generated (Fig. 3.13 C), which eventually leads to rollback and subsequent reduction in stress in 30, 40 and 50 Myr old slabs, and those with a strong UWL can create issues surrounding slab morphology which will be discussed later.

3.2.4 Importance of the thickness of the overriding plate

In this section I altered the thickness of the OP from its initial value of 100 km thickness, to half that at 50 km thickness. The reason for doing so was to see if there was a way to vertically distribute the stresses within the plate, to see if this affected the potential stresses that could be created within it. By doing this, the density of the plate is also affected, which has an effect on its buoyancy. This was good reason to have an effect on the descent of the slab into the mantle, which from previous sections of this chapter have played such a significant role in OP compressive stress. Density of the OP has also been suggested to affect the stress state of the plate directly in Holt et al. (2015), so I generated results that would have the same effects

By varying the thickness of the overriding plate using these two values – 100 km and 50 km – the stresses did also change. Using slabs aged 30, 40, 50, 60, 70 and 80 Myr with both OP thicknesses in a medium viscosity mantle ($1x10^{22}$ Pa.s), I explored the stresses (Fig. 3.14.). No phase changes were incorporated.

Effect of overriding plate thickness

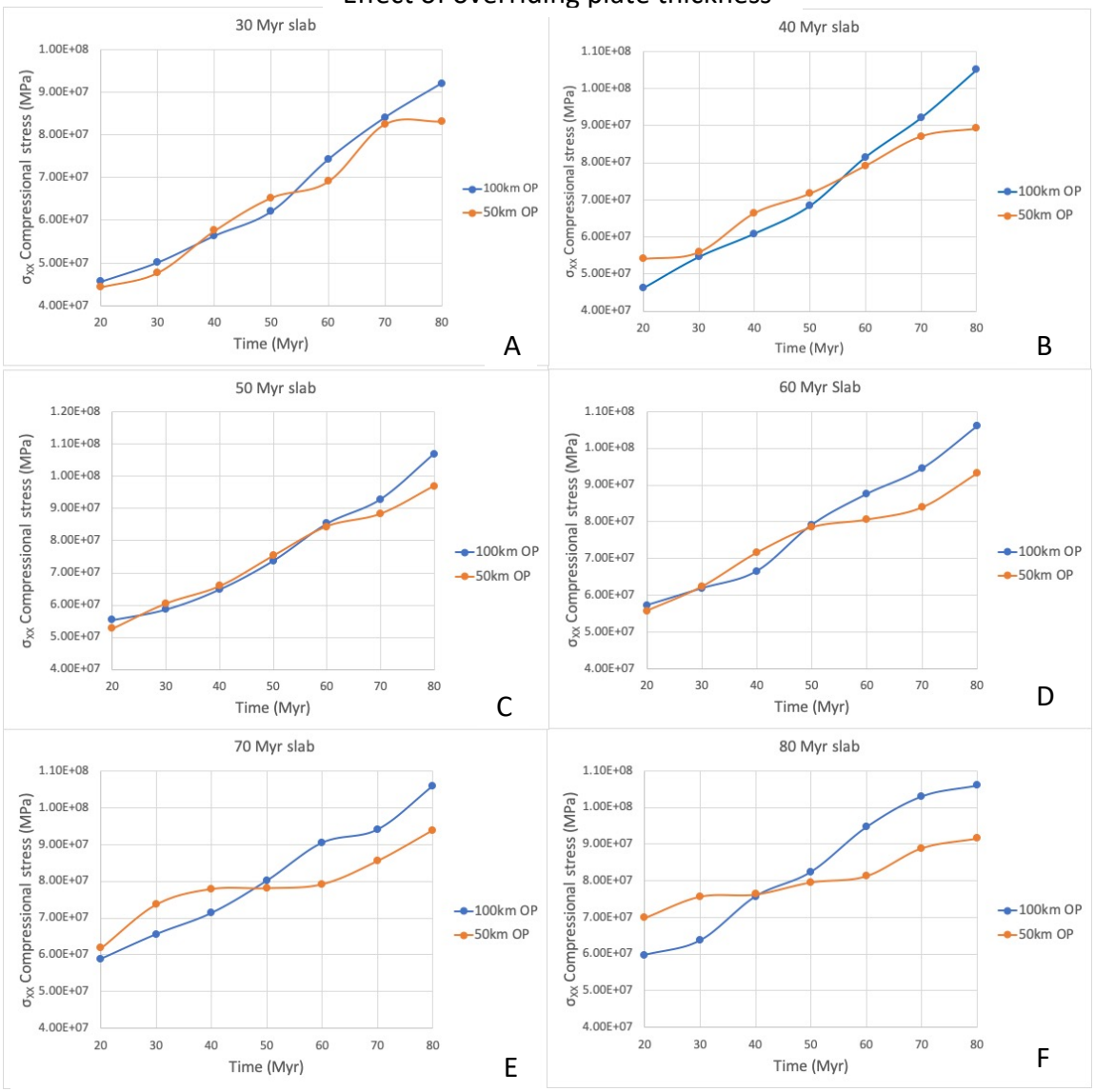

Fig. 3.14. Time (Myr) against compressive stress (MPa) for slab ages between 30 and 80 Myr, with curves to show changes in compressive stress in the overriding plate by altering thicknesses from 50 km to 100 km. Medium viscosity mantle.

Between 20 and 40 Myr of elapsed time, models containing an OP of 50 km thickness can exhibit compressive stresses up to 10 Mpa higher than those with an initial thickness of 100 km, particularly in older slabs. All variations of slab age models will display higher compressive stress in the early stages of subduction with a thinner OP, where a thicker plate has a tendency to display greater compressive stress at later stages, as a general rule.

Slab ages of 60 Myr and younger show very similar compressive stress through time, beginning at 50 Mpa for both OP thicknesses until 80 Myr from subduction initiation, where a difference of 10 Mpa is

observed and final OP compressive stress reaches 110 Mpa in a 100 km OP, and 100 Mpa in a 50 km OP model.

Slab descent velocities also vary with changing OP thickness, where doubling the OP thickness can decrease the velocity by 0.5 – 2 cm/yr, though this effect is more apparent in older slab models. For example, 80 Myr old slabs with an OP thickness of 50 km descend at 5.5 cm/yr, where 100 km of OP thickness allows for 3 cm/yr. 70 Myr old slabs with 50 km thickness display 3 cm/yr while a 100 km thick OP in the same configuration shows 2.5 cm/yr of slab descent velocity and so on. This is consistent across all model pairs but the offset between rates of descent gets smaller with reducing slab age, with velocities after ~50Myr (depending on the model) then descend at similar rates of between 1 – 3 cm/yr; the timing of which and actual velocity again varies with slab age.

We can conclude from the models that thickening the overriding plate generates the highest levels of compressive stress, exhibiting an increase of around 10 Mpa between models with a 50 km plate and those with a 100 km thick plate, and as such are important for the long-term development of orogeny. These results again express a supporting case for the correlation between slab age and resultant stresses, in that models with an 80Myr old slab and 100 km thick overriding plate displays over 100 Mpa of compressive stress at an earlier stage, while retaining high OP compressive stress for longer than any of the other models tested.

3.2.5 The effects of the 660 km mantle phase transition

I generated sets of models both including and excluding a phase transition at 660 km depth (Section 2.2, Eq. 2.3), created to determine their effects on OP stress and to see their contribution towards slab morphology. Initially, I explored the stresses in each of the models for comparison, but time allowed for a less in-depth analysis of this aspect. The stabilising effect of the phase transitions in reality is due to the endothermic mineral reactions taking place beneath 660km depth, meaning that heated buoyant material rises, counteracting slab descent into the lower mantle past this depth. There is an initial reaction occurring at 410km depth at the start of the mantle transition zone (MTZ) but this would have been too computationally expensive to have incorporated into the models of this study.

Subsequently, the major morphological features developed from the inclusion of a phase transition are included in this section (Fig. 3.15), while stress differences and slab descent rates are elaborated on in section 3.2.6.

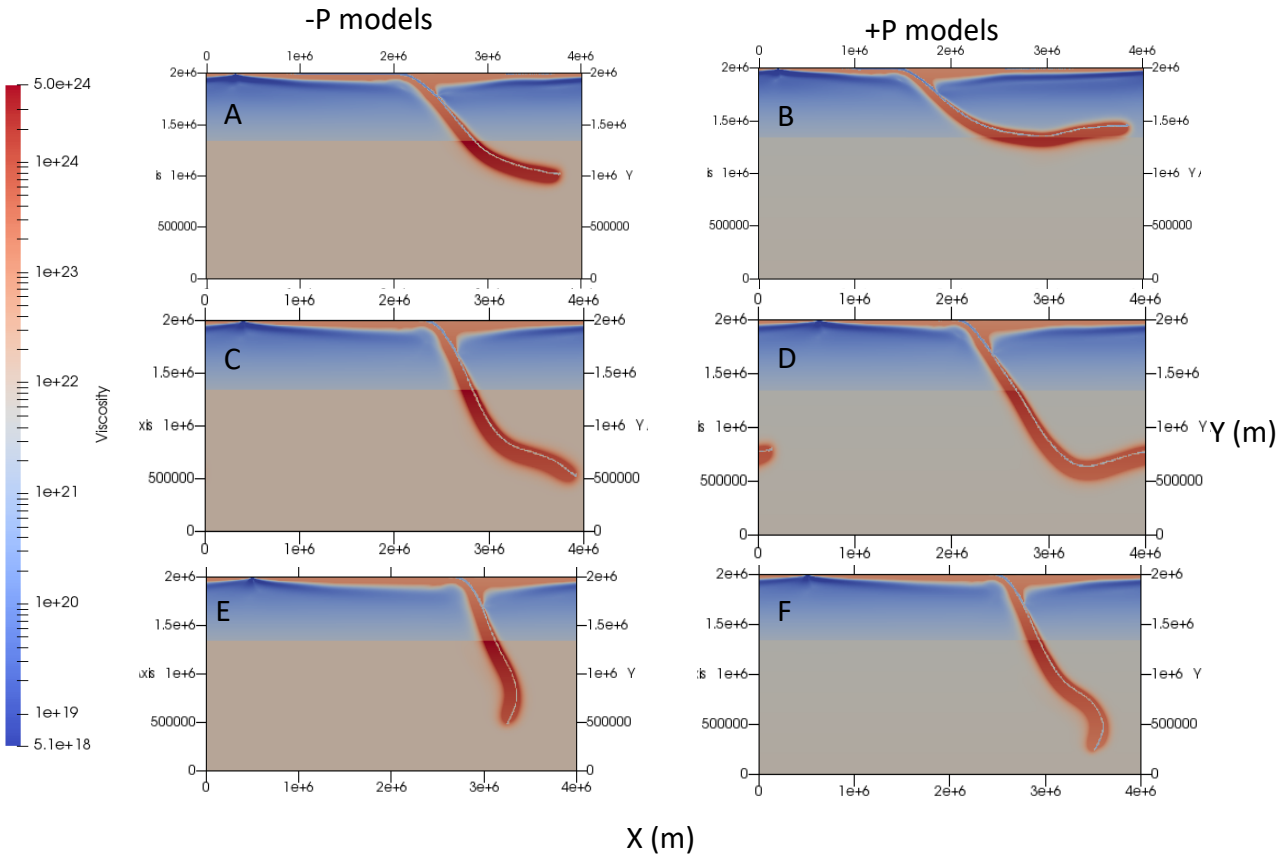

Fig. 3.15. 80Myr old slabs with rows depicting differing UWL strength (A<C<E) and columns marked either -P excluding phase changes, and +P including phase changes. Each model has run for 70Myr within the same medium viscosity mantle.

Plate velocities are increased with the inclusion of phase changes into the models. The model with a weak UWL and a phase change included (Fig. 3.14 B) at 40 Myr has a maximum plate velocity of 7 cm/yr, where the equivalent configuration without phase changes has a maximum velocity of 5.5 cm/yr, reflected in the trench positions being over 500 km to the left hand side of the model box with implemented phase changes. This is seen in each of the models throughout this study, all of which exhibit a difference of between 1 and 2 cm/yr in each case from Fig. 3.14. Further investigation in section 3.2.6 highlights a maximum of 10 Mpa difference in compressive OP stresses, which is consistent across the models (Fig. 3.18).

The implementation of mantle phase transitions into the models stabilises slabs as they descend, reducing their dip angle, in particular at the mantle transition zone at 660 km depth. This allows for slabs to rollback more or less efficiently dependent on this dip angle, where shallow dipping slabs have higher plate velocities, creating more roll back and vice versa (Fig. 3.14). With the increased stability

from phase transitions and shallower slab dip angle, rollback is promoted in all UWL strengths, mantle viscosities and slab ages.

The role of phase changes acting on slabs remains minimal in our models with regard to obtaining higher compressive stresses in the OP. Due to this, as well as a lack of time to fully explore the effect of phase changes in detail, I allowed for further analysis to be considered when implementing all parameters together in section 3.2.6, where stresses are explored.

Models that reach the highest values often obtain unrealistic morphology, which is where this fine control can be of use. Strong coupling and subsequent steep slab dip angles can be reduced when interpreting models with particular slab ages.

3.2.6 Model generating highest OP compressive stress with respect to morphology

All things considered, the model that exhibits the highest compressive stress in the OP contains an 80 Myr old slab (Fig. 3.3) This is the oldest – and densest – slab of all the models generated from this study. Results in this chapter have also highlighted the contribution to compressive stress in the OP by the mantle viscosity and the strength of the UWL. Reduced mantle viscosity in particular exhibits the highest compressive stress in the OP through sinking velocities of 80 Myr slabs at early stages, reaching up to 5.5 cm/yr and 110 MPa of OP compressive stress within 40 Myr (Fig. 3.9).

With respect to this, configuring mantle viscosity and UWL strength both to a medium setting (Sections 2.5 and 3.2.2.2 for values) satisfies these morphological issues, while generating over 100 MPa of OP compressive stress within 80 Myr (Fig. 3.15 B). Two models exhibit morphology that develops a strong convection cell with and without the 660 km phase transition included in the system are presented (denoted herein as '-p' without phase changes and '+p' with phase changes). These represent the parameter configuration with highest compressive stress in the overriding plate (fig. 3.16, Fig. 3.17).

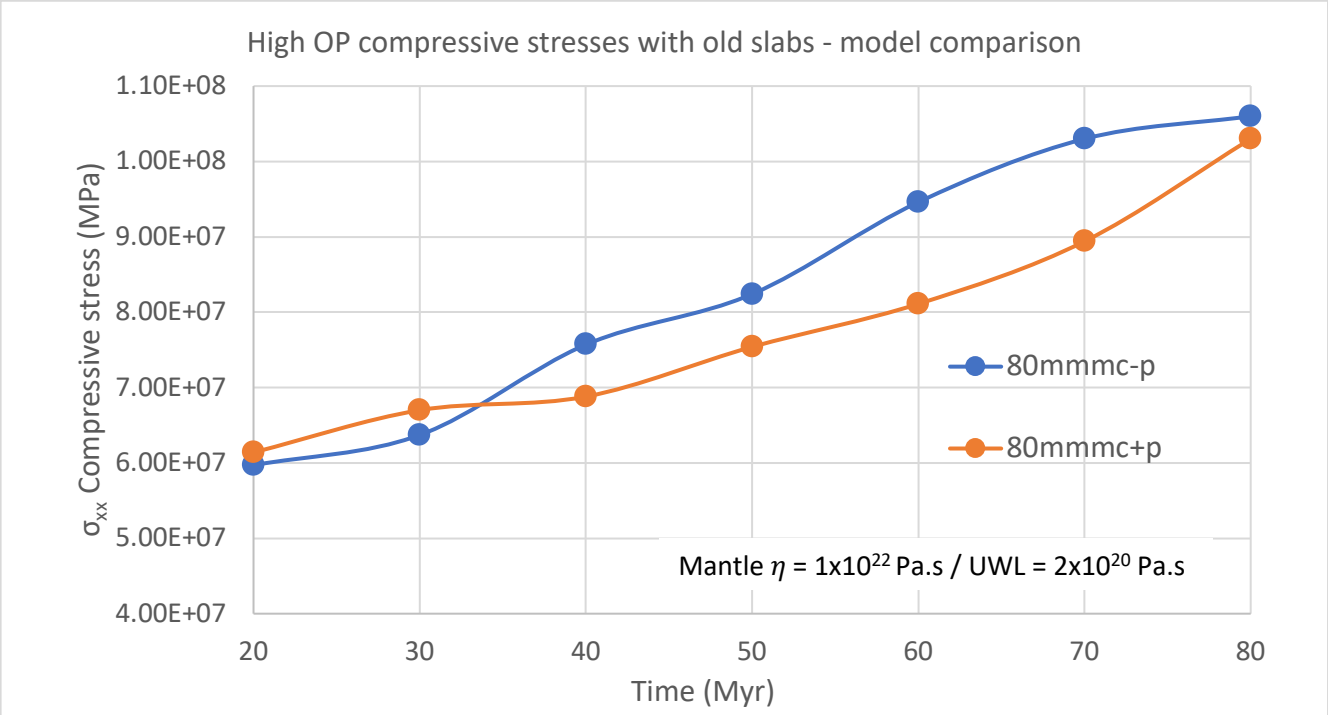

Fig. 3.16. Maximum OP compressive stress in MPa in models in medium mantle and UWL configuration through time. Blue indicates model without phase changes (-p) and orange for model including phase changes (+p).

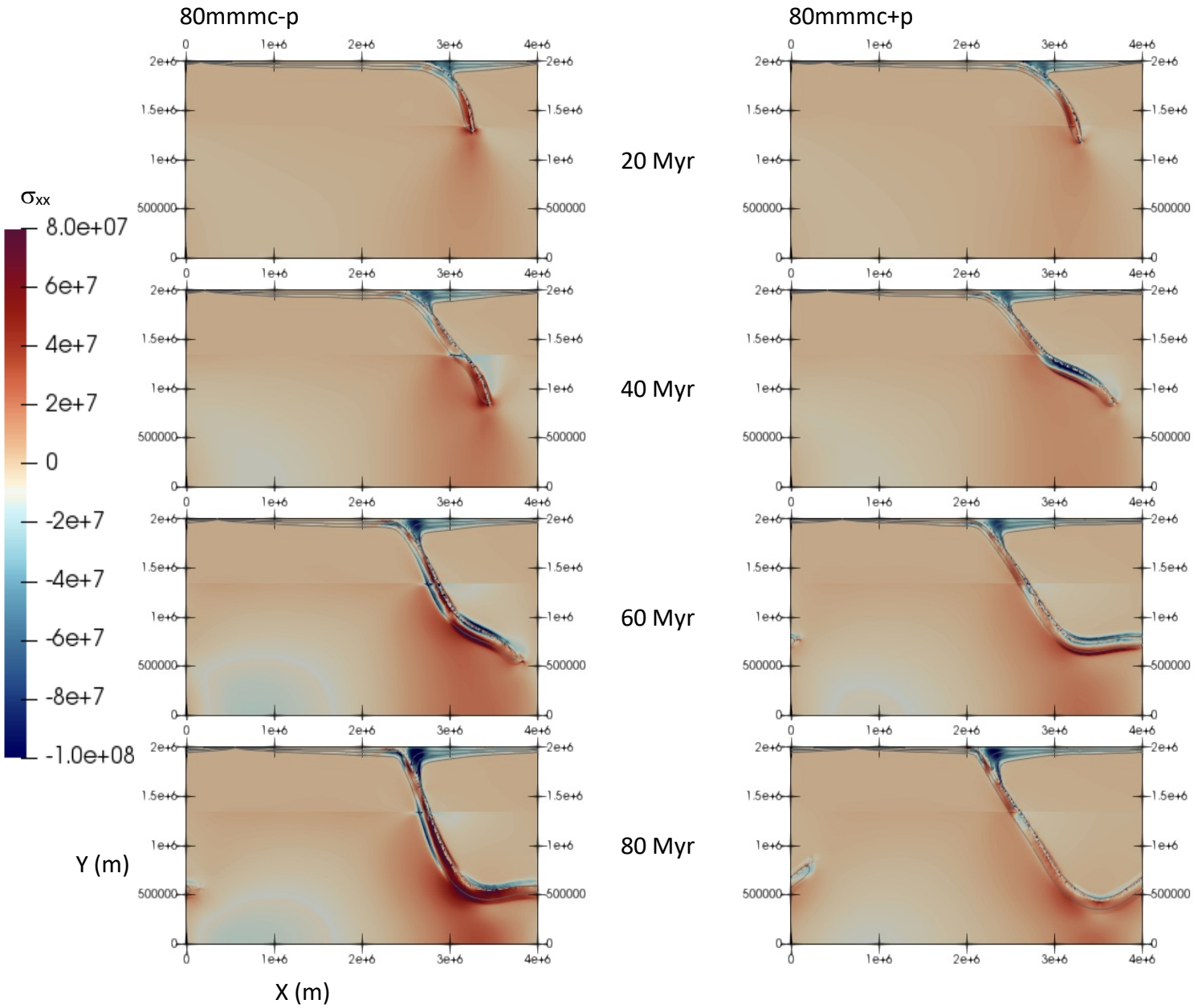

Fig. 3.17. Models from Fig. 3.18 containing a medium viscosity mantle and UWL strength, 80 Myr old slab without the incorporation of a 660 km phase change (-p left) and including phase change (+p right). 4 timesteps from 20 Myr since subduction initiation at 20 Myr intervals. Plotted using shear stress (see scale in MPa), with contour lines to indicate temperature gradient from 273˚ to 1623˚K (0˚ - 1350˚C).

Each of these models exhibits over 100 MPa of OP compressive stress, with -p model reaching this before 70 Myr from subduction initiation, where the +p model reaches it marginally later just less than 80 Myr from initiation (Figs 3.16, 3.17). The +p model shows initial higher OP compressive stress within the first 30 Myr, until the -p model overtakes this value for the remainder of the model run, with the only difference between the two configurations being the inclusion of the phase transition at 660 km (Fig. 3.17).

The morphology of these two models is similar, but with the +p model showing ~ 300 – 400 km more total rollback, given the eventual position of the trench (Fig. 3.17). This suggests greater slab sinking velocity into the mantle (Fig. 3.18), which at early stages can be seen in the first two images, where the +p model shows a depth of 800 km with the -p model only just approaching the 660 km transition (Fig. 3.17). More slab material has descended in the +p model past the 660 km MTZ on the right column through time, but the OP compressive stress seen in Fig. 3.17 exhibits higher values.

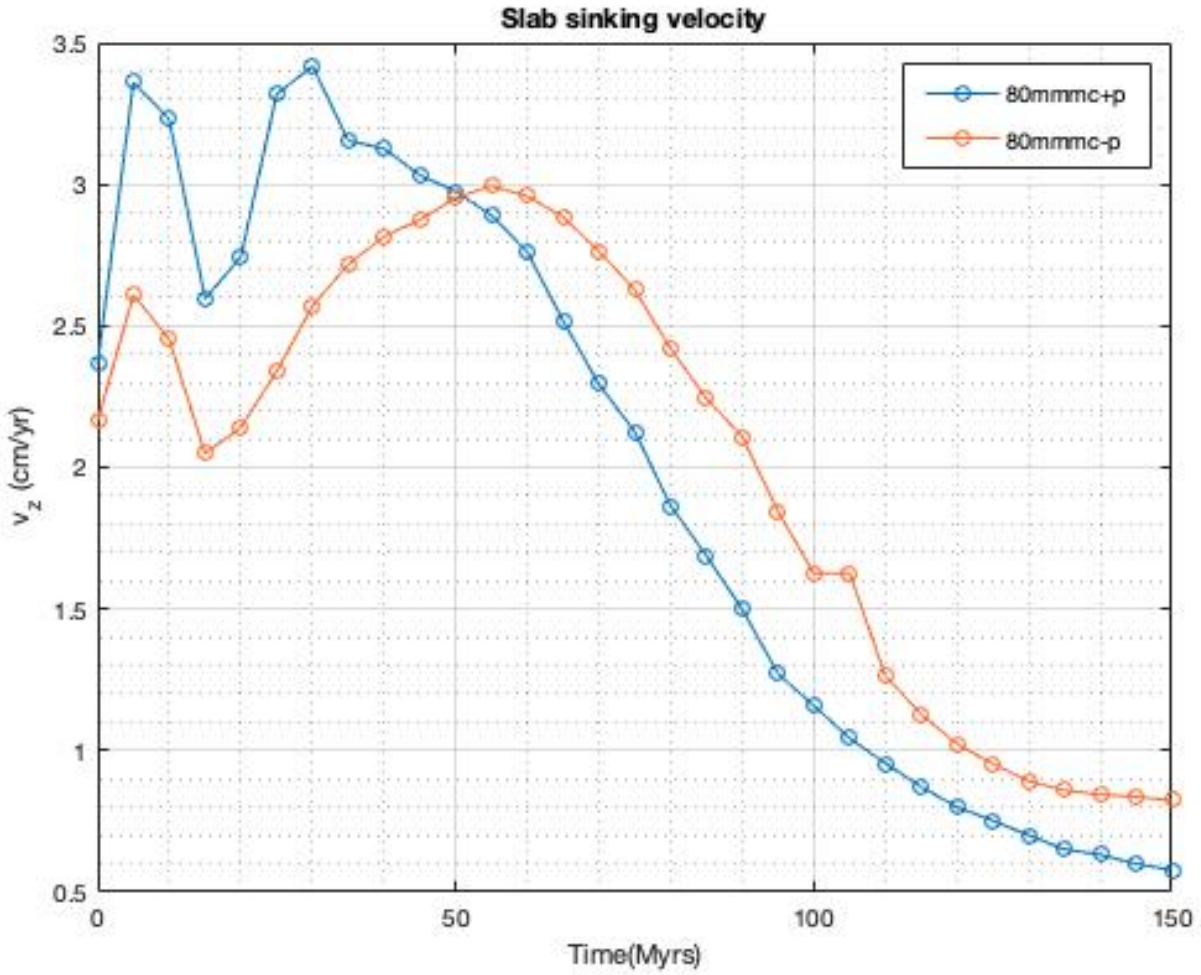

Fig. 3.18. Slab sinking velocity for models from 3.16 and 3.17 through time at 5 Myr intervals for each model iteration. Highlighting the difference in descent between the two with, +p exhibiting greater sinking velocity up to 50 Myr interval, where -p displays higher sinking velocity after this point.

From initiation up to 50 Myr, the +p model has a greater sinking velocity just below 3.5 cm/yr, with the -p model showing similar point of highs and lows at 5, 15 and 30 Myr intervals but at a changing rate of between 0.5 – 1 cm/yr less (Fig. 3.18). The -p shows a steady increase in velocity, where the +p model shows more of a fluctuation followed by an eventual decline at 35 Myr, where the -p model is still increasing from 2.75 cm/yr up to 3 cm/yr at 50 Myr. After 50 Myr, the -p model exhibits up to

1cm/yr greater sinking velocity than the +p model, with both showing a gradual yet similar decline. OP compressive stress is comparatively < 5 Mpa lower in the -p model within the first ~30 Myr, where the rate of slab descent is also up to 1 cm/yr lower – though the -p descending velocity is lower than the +p velocity until 50 Myr from initiation. However, the +p model reaches its maximum sinking velocity at 30 Myr and begins to descend, where at this point the -p model is still increasing and does so up to 50 Myr time since initiation, essentially reducing the deficit between the two.

The sinking velocities seen in figure 3.18 appear to correlate with increases of compressive stresses exhibited in figures 3.16 and 3.17, where slabs sinking faster at a given time interval exhibit higher stresses. This is especially true where -p models descend below the 660km MTZ, as the phase changing effect enabling the slabs to lie parallel to the mantle boundary is not implemented, allowing for slab dip angle to be higher (Fig. 3.17) thus leading to higher stresses.

3.3 Summary of results of parameter sensitivity

Slab behaviour and OP stresses are affected in a number of ways by varying parameter values, so in this section I will briefly summarise the results of each of the combinations explored. A schematic for these effects can be found in section 4.1 (Fig. 4.1).

Where slabs increase in age, this creates higher density meaning that slabs sink faster. This affects the compressive stress positively in the OP. An 80 Myr slab model can almost reach 100 Mpa of OP within 60 Myr, while a 30 Myr slab creates ~20 Mpa less over the same time period (Fig. 3.3).

Mantle viscosity also increases the rate of slab descent, where a reduction in viscosity means slabs sink faster (Fig. 3.7). The results show that this parameter has the strongest effect on creating high compressive stresses on the OP. A slab in a weak mantle profile compared to a strong mantle profile (Fig. 2.5) can effectively double the rate of OP compressive stress throughout time in the models (Fig. 3.6).

A combination of older/denser slabs in a weak viscosity mantle means slabs encounter less resistance to descent (Fig. 3.9). This has a positive effect on the OP compressive stress. The results show a consistent difference of ~30 Mpa through time between a 30 Myr and an 80 Myr slab model (Fig.3.8). It is also possible to create greater compressive stresses with a 30 Myr slab model in a weak mantle, compared with an 80 Myr slab model in a medium viscosity mantle (Fig. 3.10).

The strength of the UWL has a direct control over coupling and friction at the trench. This then has a clear effect on the OP stresses, as well as the amount of slab roll back (Fig. 3.11). Inducing greater coupling at the trench by strengthening the UWL hinders slab descent, but also causes up to 40 Mpa of OP compressive stresses at within 30 Myr. Slabs in this case roll forwards. Whereas less coupling from weakening the UWL reduces compressive stresses but allows for rapid descent. In this case, slabs rapidly roll back (Figs 3.11, 3.12). Both coupling and slab descent play a significant role in sustaining high OP compressive stresses. Slabs descending past the 660 km MTZ initiates an increase in OP compressive stress in all models (Fig. 3.11).

Older slab models display higher compressive stresses than younger slab models, regardless of UWL strength (Fig. 3.12 A, B and C). A stronger UWL will also cause higher OP compressive stresses than a weak UWL strength, but will exhibit unusual morphology by rolling forwards into the OP.

OP thickness was first modelled at 100 km thickness and was then halved to 50 km thickness. Initially, the 50 km OP models showed greater OP compression by 10 Mpa. A drop of 10 Mpa OP compressive stress was later observed in the models, with the thicker plate exerting more at later stages (Fig. 3.14).

Implementing a mantle phase transition at 660 km depth changed little in the way of OP compressive stresses – between 5 and 10 Mpa at a maximum value was observed – with time not permitting a full investigation of the stresses involved (Fig. 3.15). However, morphological controls were observed, and subsequently implemented for comparison with all parameters considered (Section 3.2.6).

These parameters were then explored together to generate a pair of models (Fig. 3.17) creating the highest compressive OP stresses, while retaining form that induced rapid descent (Fig. 3.18) and strong enough coupling to sustain high compressive stresses (Fig. 3.16). This was an attempt to keep high compressive stress while retain equilibrium in the model set up, allowing for balance to be achieved.

Once all parameter results had been compiled, several questions remained from the analysis. I have highlighted two which will be brought up in the next chapter:

From the previously held belief that older slabs lead to extension in the OP, what was causing the opposite compressive stress to occur in this setting? How did this then apply to what we see in reality at the Andean margin?

With the effects created from varying parameters in the models, was there a unifying feature that could link the results, other similar studies and reality? In other words, could another indirectly observable process – such as mantle convection – be driving compressive stresses?

Chapter 4. Discussion

In this chapter, I will be interpreting the model results and whether they are in line with supporting our aims and hypotheses, with a particular focus on the parameter sensitivity towards increasing compressive stresses in the overriding plate (OP).

By removing other factors for OP crustal thickening, the contribution of compression in the OP has been exclusively explored. First, the correlation between slab age and crustal thickness from Scott et al. (2018) (Fig. 1.7) is explored with respect to how the applied stresses exerted on the OP change with varying the age and resulting bulk density of the subducting slab. I will then move on to further discuss the parameters which contribute to increasing the amounts of stresses on the OP when varied, such as mantle viscosity and upper weak layer (UWL) strength, convection currents and thickness variations of the OP. I will also analyse the models that created the highest stresses while preserving morphologies that fit seismic observations. I will end this chapter with highlighting the key aspects.

4.1 Summary of parameters affecting compressive stress

The results of this study have been focused on the OP compressive stresses and how they can be varied by the altering of parameters. Throughout this thesis, we observe modelling phenomena that have created either more or less compressive stress, depending on the choice of certain physical model parameters. When combining these parameters in different combinations, further effects acting on the stress state of the OP have been observed.

Where slabs descend rapidly, or when mantle viscosity is reduced decreasing resistance to this descent, OP compressive stress has gone up. An increase in the friction at the trench also promotes

compressive stress. The same can be said for thickening of the OP, while the removal of the mantle phase transition at 660 km depth also increases this OP stress.

Scott et al. (2018) found a relationship between crustal thickening and the age of the subducting slab to be in a positive correlation (Fig. 1.7), where older slabs equate to thickening of the OP. While this has initially been thought to have induced more rollback and thus extension, this study has been able to develop 2D numerical models – possibly for the first time – to show strong supporting evidence for the correlation of Scott et al. (2018), while being applicable to global subduction zone systems.

The models predict the stresses exerted on the OP and have been used as a proxy for crustal thickening; specifically, the deviatoric compressive stresses in the x-direction (σ_{xx}) (Sections 2.4.3 and 2.4.4). While this can, on its own, be a substantial contribution to the process of crustal thickening (Schellart 2017, Holt et al. 2015), other processes have been suggested that affect the stress state of the OP. For this study, other potential sources for crustal thickening such as mantle melting and isostasy have been removed and the sole focus of OP compressive stress has been analysed. The effects that change the stress state of the OP have been simplified into a schematic for broad visualisation of parameter controls (Fig. 4.1).

Fig. 4.1 A and B show two slabs descending into the mantle over the same time period, but at different depths. This shows that older slabs sink more rapidly due to their density and create a larger convection cell. C and D exhibit the strength of the UWL and how this effects the coupling at the trench, with a strong UWL leading to greater coupling as indicated by the red line at the interface.

Fig. 4.1 E and F show the difference in slab descent as controlled by the mantle viscosity, where a weaker mantle allows for less resistance, with faster slab sinking and a larger convection cell. Next is the thickness of the OP in G and H, where a thinner OP enables greater slab descent, but less coupling at the trench. Both of these scenarios may induce a similar size convection cell. Finally, in panels I and J from Fig. 4.1 show the broad effects created by incorporating a mantle phase transition at 660 km depth. By removing the phase transition, slabs can descend more easily compared to the models that include a phase transition. Again, where slabs are able to descend more readily, a larger convection cell is generated.

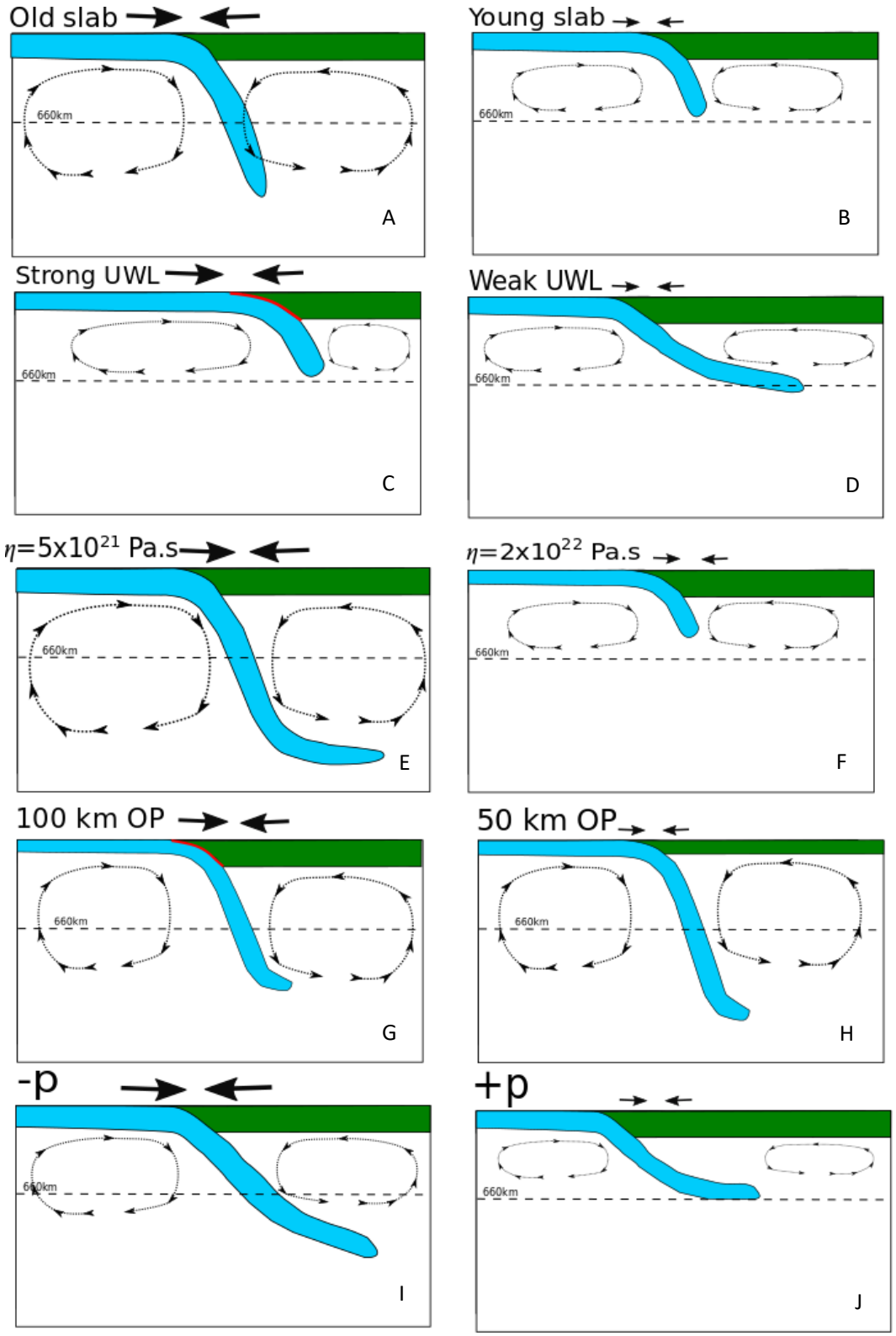

Fig. 4.1. Schematic for the effects of changing the 5 parameters used in this study. Blue to indicate slabs, green for the OP, with dotted line to indicate the 660km mantle phase transition. Larger converging arrows to indicate increase of compressive OP stress, with red lines at interface to denote the region at which an increase in coupling occurs from physical property variations. Circular dotted arrows for convecting currents. UWL represents the 'upper weak layer', while -p/+p denotes either the inclusion or exclusion of phase transitions.

Generally, the models of this study create high compressive stresses when a large enough convection cell is generated beneath the OP (Fig 4.1 A, E, G, I). This is developed when slabs reach depths beyond the mantle phase transition, which is in qualitative agreement with previous work (Holt et al. 2015, Faccenna et al. 2017). Coupling at the trench as highlighted in Fig. 4.1 (G, C) also contributes to the development of compressive stress without this effect of slab reaching deep into the mantle. When combined, slabs with enough coupling at the trench with slabs reaching the lower mantle create high OP stresses, suited to sustain topography seen in the Andes today. I will refer to the effects in Fig. 4.1 when furthering the discussion in more detail throughout this chapter.

4.2 Slab age and crustal thickness

Many studies indicate slab age as a strong controlling factor for a number of processes acting on subduction systems (Molnar and Atwater 1978, Holt et al. 2015, Scott 2018, Chen et al. 2019), particularly with the Andes as a case study. However, the relationship between increased crustal thickness and the age of the subducting slab has only recently been explored geochemically (Scott et al. 2018; Fig 1.4, Fig. 1.7), and not yet quantitatively explored through numerical modelling.

Given that older slabs have a higher bulk density, rapid descent is usually accepted to induce higher rollback and therefore extension (Turcotte and Schubert 2014). However, the models in this study have found that the increase of slab age and bulk density leads to higher compression in the OP, which is also marked by an increase in rollback; particularly upon reaching the 660km MTZ. Slabs initially show shallower dip angles when rolling back. Once penetrating through the MTZ, compression increases at an even more rapid rate (Fig. 3.12 A-F) as slabs begin to steepen their dip angle. Finally, rollback slows and slab depth increases.

This suggests why we see very high compression from the results generated in this study with a reduced viscosity mantle (5 x 10^{21} Pa.s), as the slab dip angle becomes very steep, very quickly (Fig. 3.8) and slabs descend rapidly into the lower mantle, where this high compression is reached earlier than models with a stiffer mantle. The depth at which slabs begin to bend instead of subduct further in the models exhibits the highest amount of OP compression, which in principle is similar to slab 'anchoring' (Faccenna et al. 2017), as slabs slow down and compression rapidly increases when this happens.

This is similar to slabs anchoring in the upper part of the lower mantle, suggesting that slabs remain stuck in the higher viscosity part of the mantle beyond 660km where they then stay fixed and increase

compressive stresses on the OP (Faccenna et al. 2017, Chen et al. 2019). However, in this previous work, anchored slabs do not allow for further trench motion while increasing compression (Chen et al. 2019. Fig. 1.5), as the system locks up and little movement is observed. My study, however, finds that slabs can still accumulate compressive stresses in the OP while rollback occurs, and that this rollback rate is higher in models containing older slabs. In essence, an increase in rollback seems symptomatic of models in a higher compressive stress state (Fig. 4.1 A and B).

While slabs sink rapidly through the upper mantle to the MTZ and into the lower mantle, local convective vigour in the upper mantle increases (Fig. 3.4, 3.5, 4.1 A and B). This creates shear drag on the OP, driving it towards the trench, increasing coupling and affecting the state of stress in which the plate is in. Upper mantle wedge directed flow increases with slab depth and appears to add to compressive stresses acting on the OP. Similar results have been suggested in previous work (Holt et al. 2015), where slab anchoring leads to whole mantle convection increase, dragging the OP towards the trench. It is this increasing convective vigour with rapid descent and anchoring that effectively causes the OP to move towards the trench faster than the slab is able to retreat, hence resulting in compression.

4.3 Parameter controls over sustaining high compressive stresses

With rapid slab sinking velocities instigating increased compression in the OP, this study finds two parameters that have first order control over the speed at which this happens. First, reducing mantle viscosity appears to have the greatest effect on increasing the compression (section 3.2.2, Fig.4.1 E and F).

Second is the strength of the UWL, which is adjusted in the models and the results of which can be seen in sections 3.2.2.2 and 3.2.3. This changes the coupling and also has a strong effect on descent, so the effects of the UWL strength will be discussed here together with mantle viscosity in exploring the highest rate of compression in the OP generated in this study.

4.3.1 Mantle viscosity and implications for OP compressive stresses

Mantle viscosity exerts strong control over the state of stress in the models. Within 40 Myr, the OP could experience up to 80 Mpa compressive stress if in a weak viscosity mantle setting (η_{LM} = 5 x 10^{21}Pa.s, Fig. 2.5), whereas increasing mantle viscosity by two orders of magnitude would reduce that rate by ~ 50% (Fig. 3.6).

Where reduced mantle viscosity allowed for plates to move faster, one of the dynamics that might change over shorter time scales is convection, which may create drag on the underside of the OP (Holt et al. 2015). This could account for the increased compressive stresses acting on the OP. The concept of convection adding to compression on the OP is missing from the widely accepted concept of old slabs equalling more rollback, and thus extension of the OP (Turcotte and Schubert 2014). This increase in trench directed mantle flow beneath the OP means slabs tend to anchor when in the lower mantle (Faccenna et al. 2017), having a notable increase on OP compression at early stages of subduction, and throughout time in the models. This effect may play a significant role in the development of compressive stresses in the South American plate, which sustain the high and wide plateaux in the Puna/Altiplano. When concerning the results, reduced mantle viscosity models containing slab ages > 60 Myr were able to descend more than 5 cm/year (Fig. 3.9), resulting in compressive stresses up to 100 Mpa, while slab age at 80 Myr in a medium viscosity mantle profile (η_{LM} = 1 x 10^{22} Pa.s) created similar stresses with the right coupling at the trench (Section 3.2.6).

From the results of this study, mantle viscosity has been observed to have the greatest effect on controlling OP compressive stresses (Fig. 4.1 E,F), since the mantle controls how easily descent occurs. When descending beyond the 660 km mantle phase transition, compressive stress surges are seen in other numerical modelling studies (Holt et al. 2015, Faccenna et al. 2017). Holt et al. (2015) found that in a similar mantle profile after ~15 Myr stresses could reach 40 Mpa with v_z = 5 cm/yr. The models from this thesis reflect this, though they exhibit higher stresses at earlier periods. The high stresses in my models also appear to be attributed to plate velocities similar to the study of Holt et al. (2015), where these velocities are also controlled by the viscosity of the mantle. The results that best reach morphologies consistent with these previous studies' estimates while reaching higher compression in the OP, are those containing a medium viscosity mantle profile (η_{LM} = 1 x 10^{22} Pa.s. Fig. 2.5) and with a medium UWL strength (2 x 10^{20} Pa.s.). These are seen in section 3.2.6.

While a reduced viscosity mantle promotes this behaviour, this variation in viscosity does not change over the 10's of Myr within which the Andes has seen periods of intense growth (Scott et al. 2018), so this concept is somewhat novel in terms of the formation of the Andes themselves. Mantle viscosity is typically mostly T-dependent, and T should not change much on 10s – 100s Myr timescale. One possibility is the effect of hot mantle upwelling from the superswell underneath Southern Africa, which could contribute both locally and temporally to the convective vigour acting on the underside of the plate (Garnero et al. 2016). This may give some changes to the mantle temperature seen

beneath the South American plate, and as such altering the convective vigour driving greater compressive stresses.

One further question from this study developed from the concept of reduced viscosity/ higher temperature early Earth mantle. Where temperature is thought to be between 150˚ - 300˚C hotter than today (Agrusta et al. 2018) whole mantle convection may have been more likely a convecting mechanism. This is backed up by calculations made suggesting a layered mantle convection system being inefficient to reach Earth's current mantle condition (Agrusta et al. 2018). The consequences of this being that plates would move faster.

Agrusta et al. (2018) found that in a hotter early Earth, plates produced at divergent plate margins were more buoyant and thicker due to the increased melting of hotter mantle material. Given their increased buoyancy and faster movement above a higher temperature yet weaker mantle, slabs would reach the trench quickly across a shorter distance between the ridge and the trench. This meant slabs subduct shortly after being extruded, resulting in a speed-up of the subduction process. This may have produced potential for comparable if not higher rates of OP compressive stress to what we see today (Agrusta et al. 2018). From this came the question: were ancient subduction zone orogens more intense, or in other words in a higher state of compressive OP stress? Suggestions made from other sources state that weaker tectonic plates would be unable to sustain topography >2500m given rheological instability encountered through higher mantle temperature (Rey and Coltice 2008), where high temperature rocks are also weaker. Rey and Coltice then suggest that during the Neoarchaen, a transition period caused by a cooling mantle marked a phase of intense crustal thickening. If mantle temperature was higher, plates were buoyant enough to move and sink rapidly, continental lithosphere was well developed and where mantle viscosity was lower than today that perhaps subduction orogenies were more 'intense', which matches the results of my study.

From reducing mantle viscosity, the increase in slab descent allows the implication for mantle convection inducing high compressive stresses to remain, which could be responsible for the sustaining of the topography seen today. The crucial aspect in generating the highest compressive stresses would therefore appear to be attributed to the rate of slab descent.

4.3.2 Upper weak layer strength

By reducing the UWL strength, slabs were able to subduct with ease, causing increased rollback and rapid descent into the mantle, but lower compression in the OP. Conversely, increasing the UWL strength hindered the descent with less rollback, but caused more coupling (Fig. 4.1 C and D). A reduction in sedimentation equates to higher compressive stresses on the OP, so is similar in principal to increasing the strength of the UWL.

The results suggest that coupling affects the state of stress in the OP, which is directly controlled by the strength of the UWL. There have been different amounts of coupling suggested for the South American subduction interface, which have a direct control over the rate of compression exerted between the plates (Lamb and Davis 2003). Coupling seen around the central Andes and in particular the Atacama Desert region is thought to be very high, where rainfall is extremely low and thus sedimentation is equally reduced. Here we encounter the thickest region of the cordillera (Scott et al. 2018), so to increase friction at the trench by adjusting this parameter, I explored surface processes that may be responsible for the state of stress at the margin today by simulating the strength of the UWL to see the effects. However, with respect to the study of Lamb and Davis (2003), Horton (2018) suggested that the increased coupling experienced at the trench due to reduced sedimentation is unlikely. This is due to the fact that the climatic conditions causing reduced sedimentation seen in the Atacama are predated by the current phase of Andean compression and uplift. Compressive stresses still however will have been increased given the stronger coupling, as suggested in the results of this thesis (Figs 3.12, 3.13).

The results also suggest that slabs with an increased UWL strength and a weak mantle should generate the highest compression in the OP, and initially they do with the increased coupling at the trench and rate of descent into the mantle. But models containing these parameter values advance into the OP, which results in morphologies that are not in line with seismic estimates (Chen et al. 2019, Agrusta et al. 2018) and the models rapidly become unusable. Slabs advancing into the OP continue to bend with the slab tip directed in a clockwise direction at depth, so this combination needed further adjustment. This can be seen in the erratic arrangement of compressive stress values in Fig. 3.13 C, and will be discussed further in the next chapter.

When adjusting the UWL strength to a medium viscosity (2 x 10^{20} Pa.s Table 3.), the amount of compression through time in the models goes down, but this reduction in compression is supported by the improvement in terms of morphology of the slab. Slabs in a weak mantle with this UWL setting do still roll forwards and cause morphology not consistent with Andean seismic estimates (Chen et al. 2019). Increasing the mantle viscosity coupled with the medium UWL setting creates models that have values that reach ~100 Mpa of OP compression and retain form, which is particularly true with slabs of increased age. Therefore, models with the 'mmmc' (Table 3) combination of parameters worked best in creating high compression and plausible form while matching the estimates used for instigating this study (Fig. 3.17).

Another notable feature from analysing the adjustment of the UWL strength, was that the correlation between slab age and crustal thickness associated with the Andes held true when adjusting to any UWL strength (Fig. 3.12). This was explored in a medium mantle viscosity (1 x 10^{22} Pa.s) so that adjusting the UWL strength was investigated individually. Models aligned into their maximum point of OP compression at a given time in age order, in particular where the UWL strength was at its 'medium' setting (Fig 3.12 B). This can be seen with the trend line increasing to the right of the plot. This matches the observations of the initial correlation between slab age and crustal thickness in the Andes (Scott et al. 2018), in that the older the slab, the higher the compression in the overriding plate.

The contribution of controls exerted by altering the UWL of the slab are profound in creating both higher rates of compression and plausible morphology, so better balance can yet be reached via fine tuning methods and implementing further manipulation of other parameters. Where sedimentation rates vary, slabs certainly behave in a different manner, while surface expression is also different. This can be seen in volcanic gaps or supposed flat/steep slab subduction, which could easily be better constrained so as to answer questions of previous work (Lamb and Davis 2003, Scott 2018).

4.4 Convection contributing to OP stresses

This study shows that more OP compressive stress occurs when slabs descend rapidly beyond the MTZ. This induces increased convective vigour (Fig. 3.5) while at the same time incurring more slab rollback and OP advance. This effect is controlled by combinations of parameters such as slab age and mantle viscosity, where the rate of descent is crucial for the movement of both an increase in roll back and OP motion.

This may be why the results of this study find the greatest control over OP compressive stresses is mantle viscosity (Fig. 4.1 E), especially when paired with an older slab. Both of these parameters incur an increase in convective vigour from promoting slab descent (Fig. 4.1 A, E). Substantial descent must occur in order to create enough of a mantle wedge to accommodate a larger convection cell, with slab rollback being symptomatic of this effect.

This increase in the size of the convection cell as generated by slab depth and a large enough mantle wedge is in agreement with the work of Holt et al. (2015), who show that the vigour and size of the convection cell contributes strongly to the state of stress of the OP. They note that variations in the amount of convection induced compression varies with altering the properties of the tectonic units; largely in varying viscosity contrasts between the mantle and the OP. They also found that when using a free OP and an upper/lower mantle viscosity contrast (their model viscosity values were η_{LM}/η_{UM} = 50) where slabs descended, rolled back and created a region large enough to increase convective vigour.

Rollback and convection however are not directly linked in increasing OP compressive stress. Simply by roll back going faster would not necessarily increase convective vigour beneath the OP and vice versa, so the intermediary process of slab sinking adjoins the two as this process increases both. The depth of the slab appears to generate a convection cell of greater size and therefore more intensity, contributing to a stronger compressive stress state in the OP (Fig. 4.1 A, E, G, H and I). In any case, where compressive OP stress is higher, this must mean that the OP is moving faster towards the trench than slabs are able to rollback in the same direction.

Convection contributing to compressive stress is also a better fit for the evidence seen in the Bolivian Orocline and the central Andes. 50 Myr slabs – the oldest at the margin – subduct beneath the thickest region of crust. Roll back may be reduced at this latitude from stronger coupling (Lamb and Davis 2003), but slabs are also steeper and reach greater depth than either north or south of this region. So, the addition of convection induced compressive stress may contribute to the sustaining of greater thickness we see at this part of the mountain belt.

From Holt et al. (2015) as well as my study, rapid slab descent therefore plays an important part in the rate of convection beneath the OP, as this affects both rollback and OP advance, ultimately leading to affecting the state of stress in the OP. If the OP is moving faster than slabs can roll back, then

convection currents beneath the OP may be playing a significant role in driving the compressive stresses.

4.5 OP thickness and the effect on compressive stresses

When adjusting the OP plate thickness in the models, stresses within them were different. An OP with 50 km thickness exhibited 10 Mpa greater compressive stress than models containing 100 km thickness. After 40 Myr, the stresses flipped, with the thicker plate exhibiting the greater stress (Fig. 3.15, D, E and F). This was the case for older slab models only. Models containing slabs of 40 and 30 Myr would have around the same amount of compressive stress throughout time, until finally diverging at later stages similarly to the rest of the models (Fig. 3.15 A, B and C). Initially, I expected the thicker plate to consistently exhibit the higher stresses since older/denser slabs want to converge and sink down, so when presented with these results I undertook further analysis to investigate what was happening.

A thicker plate has a larger overall strength and is therefore harder to stretch/shorten given the same amount of force available. This would mean that a thicker plate would be more difficult to deform; while retaining a higher capacity for stress when compared to a thinner plate. This is an observation conducted from the results of this study (Section 3.14 E and F), with no reference material available. The physical principle of stresses accumulating in something that is larger, therefore having greater capacity for higher stresses, or yield strength. This may be why the thicker OP models exhibit higher stresses eventually.

Thicker OP models would also give a larger surface area for coupling at the plate interface, which could add a marked increase in compressive stresses seen in the models (Fig. 4.1 G, H), similar to the effect of a stronger UWL (Section 4.3.2). Friction created is strong enough to drag the OP down into the upper mantle to greater depth as time increases (Fig. 3.17 where blue indicates higher compression and the OP material). This would only increase as time elapses, which is most likely responsible for the late development of increased compression seen in the models with enough strength to drag the OP down.

Rollback rate also goes up with increased slab descent rate in both models, allowing slabs to anchor into the lower mantle. This is controlled in a similar way by the thickness of the OP either aiding or hindering descent (Fig 4.1G, H). Again, this is most likely a feature of the increased coupling at the broader interface between the slab and the thicker OP.

Where and why the thickness variations appear in the Andes is well understood, so the differences in thickness I emplaced during this study are over-simplified by comparison. The trade-off between plate thickness and crustal thickness creating opposing bulk density effects and resulting isostatic variation significantly affects the entire system (Scott 2018). Continental slivers and embedded cratonic material (Horton 2018) at the margin make the OP thickness difficult to define.

In terms of this study however, where OP thickness is increased compressive stresses also go up. This is mostly controlled by the thicker plate being more difficult to deform, enabling higher stress accommodation as well as a broader subduction interface causing strong coupling. Both processes contribute to the stresses.

4.6 Relative importance of the model parameter contributions to Andean compression

When looking into the parameter contributions to stresses acting on the overriding plate, some varied over time scales that were relevant to the development of the Andean orogeny, where others did not. In this section, I will list the effects that apply to the Andes temporally. The parameter sensitivity explored in this study has been discussed with respect to generalised numerical modelling. When applying this to the Andean margin, it becomes clear that not all of the parameters vary over time scales in line with key stages of Andean evolution. This is important to feature as this study has sought to explain the correlation between crustal thickness and slab age found at the Andean margin, particularly in sustaining the high and wide central Andean plateau.

Where the results show that mantle viscosity variation creates strong control over OP compressive stresses, this feature does not vary over 10's of Myr periods. As explained and highlighted in previous work (Agrusta et al. 2018) mantle temperature may have varied by 150˚ - 300˚C over 3 Gyr. Subsequent viscosity changes would have taken place over such a long period of time, but this is not a relevant time scale for Andean growth that we are addressing in this study. MTZ behaviour would also not behave in a rapidly evolving way (Goes et al. 2017), so as to affect the state of stress in the OP over such short time scales. Furthermore, should the mantle have a reduced viscosity, then isostatic equilibrium from glacial rebound estimates (Schellart 2017) would be significantly affected as the OP may sit deeper into the upper mantle.

OP thickness is thought to vary latitudinally (Scott 2018), but the variations encountered in real world are difficult to match in the simplistic approach adopted by this study. Where this study finds that a greater OP thickness leads to an increase in compressive stress, this is a simple positive feedback loop. The processes excluded by this study such as melting should be included so as to initially generate the thickened OP, so as to more accurately reflect the temporal evolution of the OP and its thickness.

UWL strength variation resembles Lamb and Davis (2003) and their look at sediment-starved versus sediment-rich subduction zone segments in the Andes. An increase in UWL strength would simulate the conditions seen in the Atacama Desert, where some places have not seen rain in a century. But previous studies show that compressional deformation started earlier than the climate change and sediment starvation along the Andean margin, so their model does not match reality (Horton, 2018). This is a parameter that could vary within the same time frame but is not suited to the current surface expression.

That leaves slab age, as the only parameter that we know varied over time in reality, which produces a change in the OP in the models. Andean slabs entering the trench over the last ~190 Myr period have not exceeded 80 Myr, but the onset of compressional deformation is thought to have occurred at intervals where slabs at the trench become older than 40 Myr (Scott 2018). For this reason, an increase in slab age at the trench can be attributed to greater coupling, therefore higher compressive stresses. The models in my study reflect this, as the older slabs are in the models, the greater the compressive stresses.

Chapter 5. Model limitations and future work

When developing the models used in this project, there were a number of features that meant full exploration of the Andean subduction margin was not possible with the tools made available by ASPECT. This is despite it being a very useful and powerful code for many supporting arguments in geodynamic concepts. This left this study open for further exploration and future work, as well as highlighted some limitations in some aspects of the models. For instance, at the time of the start of this project until today, it was not possible to incorporate a 'free surface' (as opposed to a 'free-slip surface' this study uses) in models in combination with particles. These particles are essential for tracking dynamics of the UWL, as described in the thesis.

I had to remove other processes associated with crustal thickening such as melting, erosion and isostasy to look solely at horizontal compressive stresses as a proxy for crustal thickening (section 2.4.3). This was central to the investigations of this project, and though being insightful to processes at the margin, to be able to model the surface expression directly would be a powerful approach in understanding the tectonic development of The Andes. This would be more suited to future studies where processes attributed to OP crustal formation could be fully explored. It would also allow for the temporal evolution of crust at the margin to be modelled and perhaps better understood (section 4.6).

Another subject of future work was the periodic boundary conditions allow for a convecting current to leave the right-hand side (RHS) of the box, emerging on the left. This allows for the effects of the mantle flow's contribution to compressive stress to be increased and may be the main reason that all of our models from timestep 1-30 (or every 5myrs for each timestep) shows no extensional character during the subduction process; at most a lowering of compression is seen.

I started to address this issue in two ways, which time unfortunately didn't allow the continuation of, but preliminary results were developed. Initially I doubled the length of the box along the x-axis and made the OP thin so as to promote extension. This came close to reaching tensional stresses, but when adding a thin buoyant layer above the OP acting as an upper crust and increased the viscosity of the mantle, this allowed for extension to be spread across most of the plate, except for the region closest to the trench. The idea behind this was that if the thinner and weaker OP was buoyant enough and slabs couldn't descend rapidly but displayed increased rollback, the OP would remain at the surface of the box and want to spread out, thus generating extension.

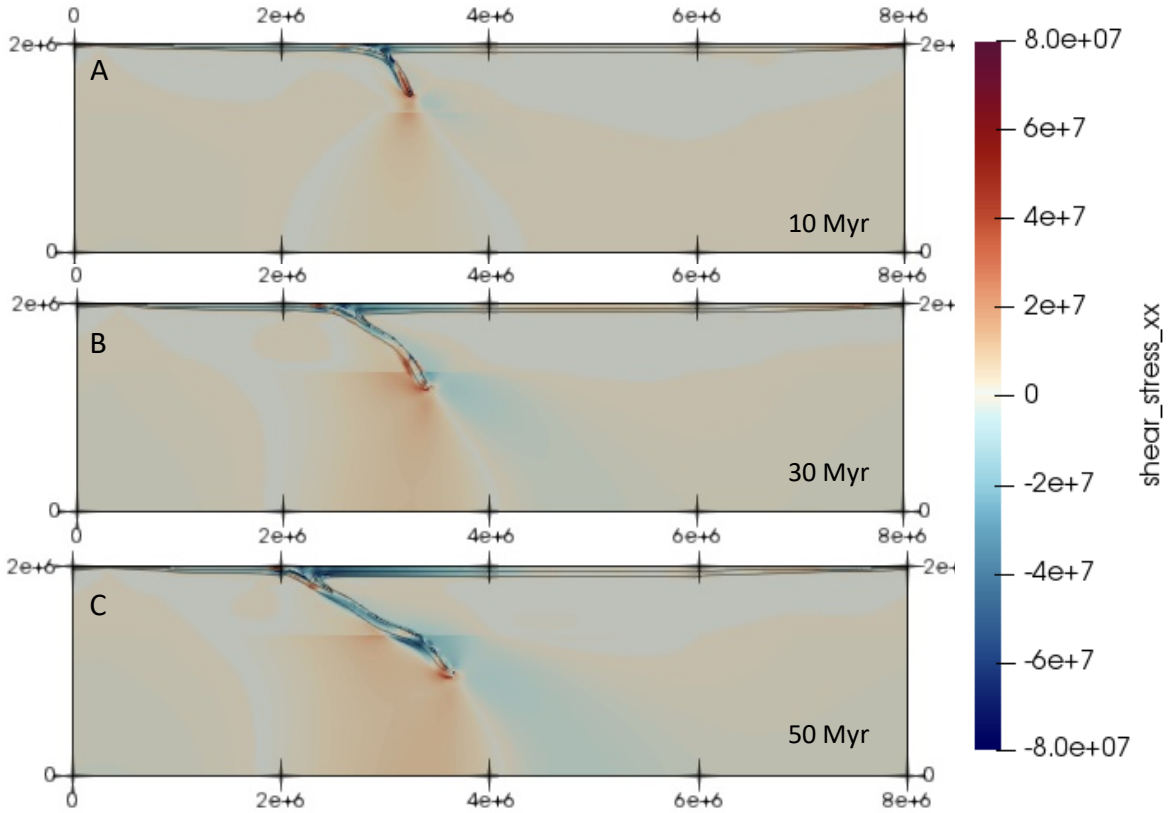

Fig. 5.1. Three stages of extension models showing very minor (5-10 MPa) of tensional stress in the OP. Isotherms to highlight slab morphology. As the slab descends, compression begins to overtake the tensional stresses as the model develops through time.

Further exploration of the default model setup from Fig. 5.1 would be insightful for investigating the evolution of the stress state of the Andes in more detail, as this is more in line with what is thought to occur in reality, as well as being in agreement with previous works' estimates (Holt et al. 2015). They were able to generate extension in the OP by either weakening the plate, or by sticking it to the RHS of the box while also continuing to use periodic boundary conditions. This was the second approach I adopted when trying to simulate widespread extension.

However, when attaching the plate to the RHS of the box, reducing the UWL so as to initiate rollback and extension using an old slab, the models rolled forwards and into the OP, causing high compressive stress due to increased coupling from trench advance. This left the results unusable for interpretation (Fig. 5.2). To test whether the boundary conditions are actually the cause of the difference in extension

between my models and those of Holt, we would need to get models with a closed side boundary to work. This is something to be done in the future.

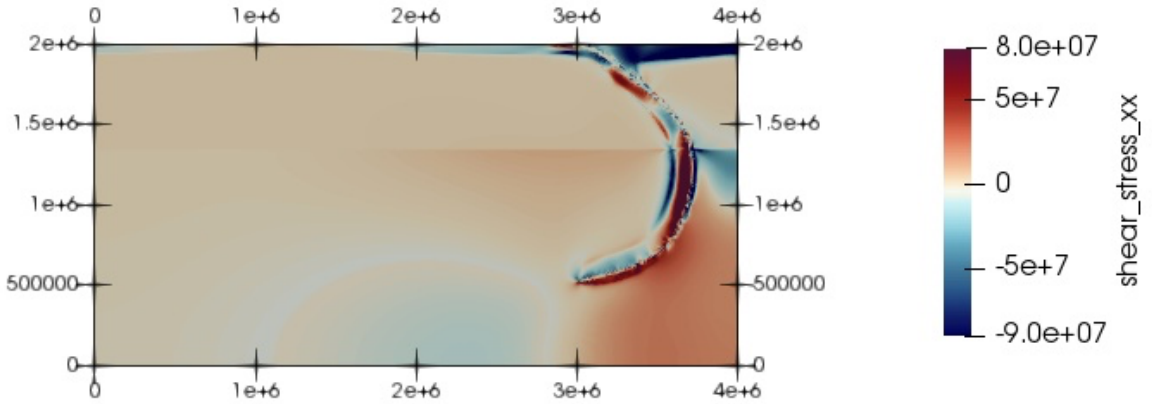

Fig. 5.2. Model containing a fixed OP attached to the RHS of the box after 50 Myr since subduction initiation. Default trench position between 2000 and 3000 km on x axis, marking an encroachment into the OP of almost 1000 km.

Similar issues were encountered when varying the strength of the UWL, particularly when increasing it. Instead of greater coupling at the trench generated from a lack of sediment simply creating higher compressive stresses (Lamb and Davis 2003), slabs advanced far into the OP, again making results unusable (Fig.4.1 C). The reduction of sedimentation into the trench was not able to be fully explored, despite discovering which values to avoid when trying to reach the highest compressive stresses with respect to morphology (section 4.3.2).

At t=0, the UWL is emplaced along the subducting plate, but is not renewed at the mid-ocean ridge (MOR) afterwards. This means that at different time intervals depending on the model, the part of the UWL that was at the MOR at t=0 reaches the trench. After that, the model runs out of UWL material. To resolve this, models either need a longer distance from MOR to trench, or the UWL needs to be created continuously at the MOR. Due to further time limitations, the latter option was not implemented. Once the UWL had run out in all of the models, the compression in the OP surged, with the entire system locking up and generating unusable results (Fig. 5.3).

Through the use of adding or removing sediment at the trench over time in the models would allow for better understanding of temporal evolution of friction at the trench to be explored, which may go some way in addressing the arguments proposed by Lamb and Davis (2003). Adding an unlimited UWL

resource would also be useful to fully explore this evolution, as this would be closer to subducting plate (SP) crust production in reality and another interesting avenue for future work.

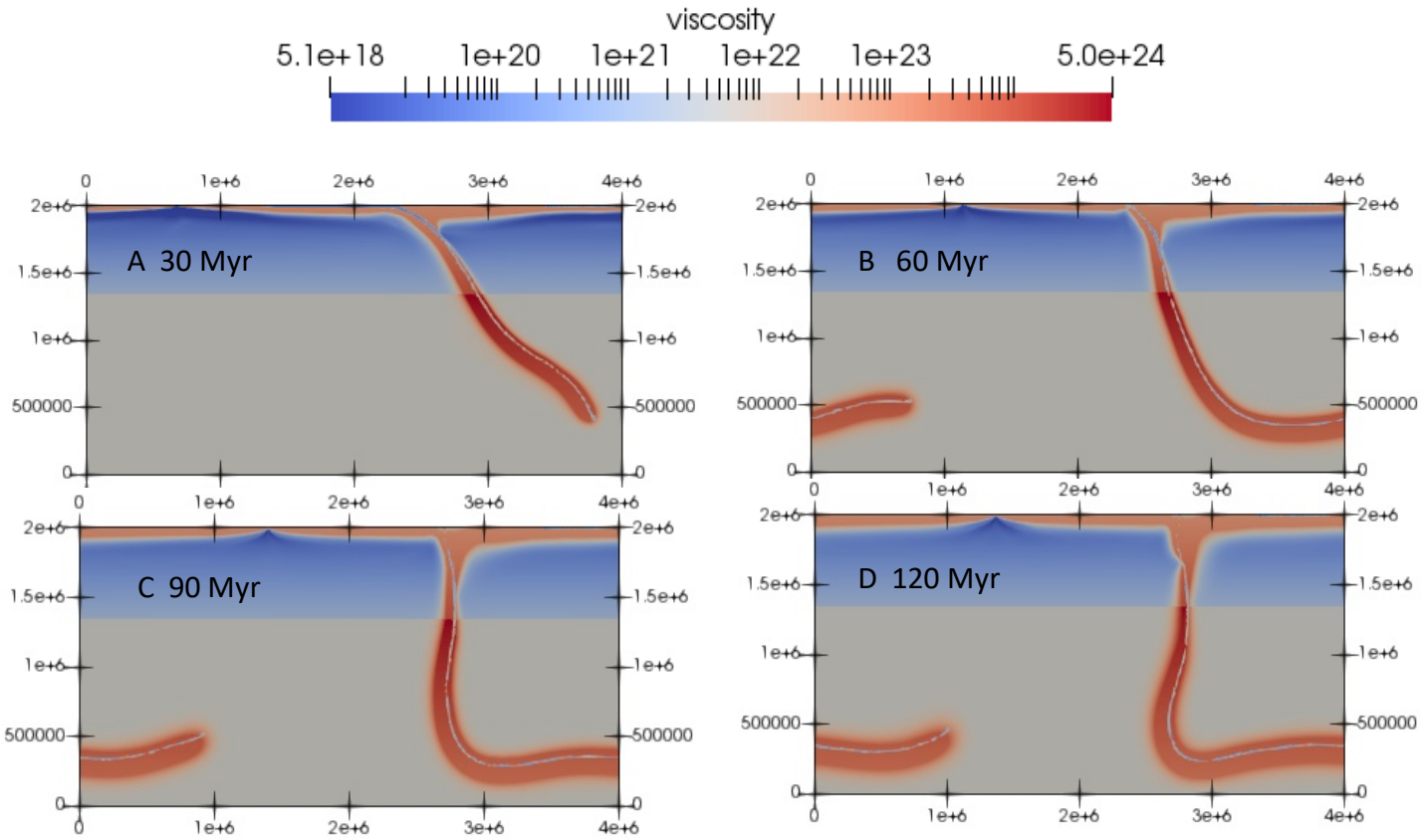

Fig. 5.3. Showing the resulting effect of UWL material running out, and the subsequent effect this has on slab morphology. UWL can be seen as the blue line through the slab profile. Four timesteps at 30, 60, 90 and 120 Myr time intervals. Curvature of the slab increases at a very early stage, with UWL material running out at B (60 Myr) and the model subsequently breaking down. Set in a weak mantle (5 x 10^{21}Pa.s) and a weak UWL (1 x 10^{20}Pa.s).

The Nazca plate varies in age and density latitudinally and has regularly monitored convergence velocities (Avg. V_z ~7.2 cm/yr. Scott et al. 2018, Faccenna et al. 2017, Holt et al. 2015) occurring at the same speed for the entire plate. It is not possible to model this in 2D, so 3D models would need to be generated in order to see if the compression within the OP responded in the same way, such as in the study conducted by Schellart (2017). A crucial argument for this thesis has been the rate at which slabs descend into the mantle leading to high compression, as this drives the convection increase contributing to OP stresses. This has been seen throughout this thesis and explored in previous studies (Holt et al. 2015).

By modelling one plate that varies in age at the trench, with another option to subduct the plate obliquely to the margin as it does in reality could then be incorporated. Regions with volcanic gaps

thought to be caused by flat slab subduction – or lack thereof – (Espurt et al. 2008, Faccenna et al. 2017) would also then be able to be investigated with respect to compression in the OP by modelling the margin in 3D. In order to explore the effects of the UWL on OP compressive stress fully, adjustable and localised sedimentation rates acting on a 3D slab in a subduction model would also be more appropriate in determining the true effects that this factor has on the margin. Features seen at the margin such as cratonic lithosphere or the subduction of buoyant ridges could be incorporated if using a 3D model set up, which gives a huge amount of potential for future work to be addressed based on the findings in my study.

In reality, the mantle wedge is composed of a low seismic velocity region of volatile rich melt from fluid drawn off slabs (Turcotte and Schubert 2014, Liu et al. 2016, Magni et al. 2017), this region itself would act as a lubricant for the down-going slab which would reduce friction and coupling. This effect was seen when varying the thickness of the OP in section 3.2.5 (discussed in section 4.5)

Previous studies have encountered similar issues in the effects created by dragging down the OP, with simple parameterisation being incorporated to reduce this regions effect on the state of stress and promoting a more realistic mantle setting. Hydrous mantle wedge weakening is introduced so as to reduce the effects of this increased coupling (van Hunen et al. 2002), which if elaborating on the set of models used in this study would be an appropriate feature for incorporation, as well as a viable outlet for future investigation.

Where these aspects have been applicable to the Andes, other such orogenies could use similar approaches in addressing the relationship between the parameters explored in this study. For instance, the intra plate formation during the Laramide orogeny in North America may be better understood, with this orogen taking place over 1000 km from the nearest trench region of the subduction zone. Other South American intra plate tectonics seen in the Neuquén basin could explain some of the complex structural features encountered there (Scott 2018, Chen et al. 2019). This could shed light on some of the aspects that move the system from tension to compressive stress in the OP (Fig. 1.6). Implementing some of the parameter variations used in this study may be useful in addressing this.

Chapter 6. Conclusions

In this study, I set out to explore the relationship between slab age and crustal thickness at the Andean Margin. I did this using the open source software tool ASPECT to make models that simulate overriding plate (OP) horizontal compressive stress as a contribution by proxy for crustal thickening. This is one of the proposed ways to form a thick continental crust, though others such as crust formation in the subduction zone itself are likely to be equally valid.

I then also used this to further interpret how to reach high compressive stresses in the OP by varying 5 main parameters: slab age, mantle viscosity, upper weak layer (UWL) strength, OP thickness and implementing mantle phase transitions. From these investigations, I am able to conclude the following.

Old subducting slabs cause more compression in the OP by having higher bulk density, which increases slab sinking velocity. This attracts the OP towards the trench more readily, and generates a convection cell beneath the OP. The models show that the vigour and size of the convection cell directly link positively with the length of the subducting slab. With an increase in trench directed mantle flow, shear drag is created beneath the OP adding to compressive stresses acting on the OP itself. This is in qualitative agreement with previous studies.

Where slabs are able to descend into the mantle with ease, convection subsequently increases, so parameters that directly affect the rate at which slabs descend profoundly affect the amount of compression acting on the OP. Reduction in mantle viscosity causes the strongest effect for increased compression, especially when combined with older and denser slabs.

There is a significant increase in OP compression when slabs descend beyond the 660 km mantle transition zone (MTZ). This initiates more slab rollback as well as convective vigour. In order to create compressive OP stresses, the OP must be moving at a greater velocity than slabs are able to rollback. The thickness and resultant strength of the OP itself also plays a significant role in the stress state in which the plate is in. In the default models, doubling the thickness of the OP leads to compressive stresses increasing by 10 Mpa, where doubling the length of the OP leads to tensional stresses being exerted on the plate.

The margin and the entire system requires equilibrium from balancing slab age, mantle viscosity, UWL strength and OP thickness in order to prolong high OP stresses. Subsequent slab morphology is

important in generating the additional compressive contribution from mantle convection. This morphology is however, affected by many different parameters. Implementing a mantle phase transition can support this but when doing so, a reduction in compressive stress is observed as a consequence. Slab descent and resulting depth is further cemented as a major driver for increasing compression, when considering the morphology of subducting slabs through time.

7. Bibliography

Agrusta, R., Van Hunen, J., & Goes, S. (2018). Strong plates enhance mantle mixing in early Earth. *Nature Communications*, *9*(1), 1–10. https://doi.org/10.1038/s41467-018-05194-5

Allmendinger, R. W., Jordan, T. E., Kay, S. M., & Isacks, B. L. (2002). The Evolution of the Altiplano-Puna Plateau of the Central Andes. *Annual Review of Earth and Planetary Sciences*, *25*(1), 139–174. https://doi.org/10.1146/annurev.earth.25.1.139

Bangerth, W et al. (2018). ASPECT – *Advanced Solver for Problems in Earth's ConvecTion User Manual*. doi: 10.5281/zenodo.1297145, url: https://doi.org/10.5281/zenodo.1297145

Capitanio, F. A., Faccenna, C., Zlotnik, S., & Stegman, D. R. (2011). Subduction dynamics and the origin of Andean orogeny and the Bolivian orocline. *Nature*, *480*(7375), 83–86. https://doi.org/10.1038/nature10596

Chen, Y. W., Wu, J., & Suppe, J. (2019). Southward propagation of Nazca subduction along the Andes. *Nature*, *565*(7740), 441–447. https://doi.org/10.1038/s41586-018-0860-1

Condie, K. C. (1998). Episodic continental growth and supercontinents: A mantle avalanche connection? *Earth and Planetary Science Letters*. https://doi.org/10.1016/S0012-821X(98)00178-2

Decelles, P. G., Ducea, M. N., Kapp, P., & Zandt, G. (2009). Cyclicity in Cordilleran orogenic systems. *Nature Geoscience*, *2*(4), 251–257. https://doi.org/10.1038/ngeo469

Espurt, N., Funiciello, F., Martinod, J., Guillaume, B., Regard, V., Faccenna, C., & Brusset, S. (2008). Flat subduction dynamics and deformation of the South American plate: Insights from analog 91ndean91ng. *Tectonics*, *27*(3), 1–19. https://doi.org/10.1029/2007TC002175

Faccenna, C., Oncken, O., Holt, A. F., & Becker, T. W. (2017). Initiation of the Andean orogeny by lower mantle subduction. *Earth and Planetary Science Letters*, *463*, 189–201. https://doi.org/10.1016/j.epsl.2017.01.041

Fraters, M.R.T. (2014), Thermo-mechanically coupled subduction modelling with ASPECT. Master's thesis, Utrecht University, Utrecht, Netherlands, http://dspace.library.uu.nl/handle/1874/297347

Garnero, E. J., McNamara, A. K., & Shim, S. H. (2016). Continent-sized anomalous zones with low seismic velocity at the base of Earth's mantle. *Nature Geoscience*, *9*(7), 481–489. https://doi.org/10.1038/ngeo2733

Goes, S., Agrusta, R., van Hunen, J., & Garel, F. (2017). Subduction-transition zone interaction: A review. *Geosphere*, *13*(3), 644–664. https://doi.org/10.1130/GES01476.1

Holt, A. F., Becker, T. W., & Buffett, B. A. (2015). Trench migration and overriding plate stress in dynamic subduction models. *Geophysical Journal International*, *201*(1), 172–192. https://doi.org/10.1093/gji/ggv011

Horton, B. K. (2018). Tectonic Regimes of the Central and Southern Andes: Responses to Variations in Plate Coupling During Subduction. *Tectonics*, *37*(2), 402–429. https://doi.org/10.1002/2017TC004624

Kaislaniemi, L., Hunen, J. van, Allen, M.B., and Neill, I., 2014, Sublithospheric small-scale convection—A mechanism for collision zone magmatism: Geology, v. 42, p. 291–294, doi:10.1130/G35193.1.

Kronbichler, M., Heister, T., & Bangerth, W. (2012). High accuracy mantle convection simulation through modern numerical methods. *Geophysical Journal International*, *191*(1), 12–29. https://doi.org/10.1111/j.1365-246X.2012.05609

Lamb, S., & Davis, P. (2003). Cenozoic climate change as a possible cause for the rise of the Andes. *Nature*, *425*(6960), 792–797. https://doi.org/10.1038/nature02049

Liu, X., & Zhao, D. (2016). P and S wave tomography of Japan subduction zone from joint inversions of local and teleseismic travel times and surface-wave data. *Physics of the Earth and Planetary Interiors*, *252*, 1–22. https://doi.org/10.1016/j.pepi.2016.01.002

Marquardt, H., & Miyagi, L. (2015). Slab stagnation in the shallow lower mantle linked to an increase in mantle viscosity. *Nature Geoscience*, *8*(4), 311–314. https://doi.org/10.1038/ngeo2393

Martinod, J., Husson, L., Roperch, P., Guillaume, B., & Espurt, N. (2010). Horizontal subduction zones, convergence velocity and the building of the Andes. *Earth and Planetary Science Letters*, *299*(3–4), 299–309. https://doi.org/10.1016/j.epsl.2010.09.010

Nocquet, J. M., Villegas-Lanza, J. C., Chlieh, M., Mothes, P. A., Rolandone, F., Jarrin, P., … Yepes, H. (2014). Motion of continental slivers and creeping subduction in the northern Andes. *Nature Geoscience*, *7*(4), 287–291. https://doi.org/10.1038/ngeo2099

Ramos, V. A., Zapata, T., Cristallini, E., & Introcaso, A. (2005). The 92Andean thrust system - Latitudinal variations in structural styles and orogenic shortening. *AAPG Memoir*, (82), 30–50.

Rey, P. F., & Coltice, N. (2008). Coupling of Earth' s geochemical reservoirs. *Geology*, *36*(8), 635–638. https://doi.org/10.1130/G25031A.1

Schellart, W. P. (2017). Andean mountain building and magmatic arc migration driven by subduction-induced whole mantle flow. *Nature Communications*, *8*(1), 1–13. https://doi.org/10.1038/s41467-017-01847-z

Scott, Erin Margaret (2019) Geochemical evolution of Andean arc volcanism and the uplift of the Andes, Durham theses, Durham University. Available at Durham E-Theses Online: http://etheses.dur.ac.uk/13135/

Scott, E. M., Allen, M. B., MacPherson, C. G., McCaffrey, K. J. W., Davidson, J. P., Saville, C., & Ducea, M. N. (2018). Andean surface uplift constrained by radiogenic isotopes of arc lavas. *Nature Communications*, *9*(1). https://doi.org/10.1038/s41467-018-03173-4

Sobolev and Babeyko, S. V., & Babeyko, A. Y. (2005). What drives orogeny in the Andes? *Geology*, *33*(8), 617–620. https://doi.org/10.1130/G21557.1

Sundell, K. E., Saylor, J. E., Lapen, T. J., Styron, R. H., Villarreal, D. P., Usnayo, P., & Cárdenas, J. (2018). Peruvian Altiplano Stratigraphy Highlights Along-Strike Variability in Foreland Basin Evolution of the Cenozoic Central Andes. *Tectonics*, *37*(6), 1876–1904. https://doi.org/10.1029/2017TC004775

Tassara, A., & Echaurren, A. (2012). Anatomy of the Andean subduction zone: Three-dimensional density model upgraded and compared against global-scale models. *Geophysical Journal International*, *189*(1), 161–168. https://doi.org/10.1111/j.1365-246X.2012.05397.x

Trubitsyn, V. P., Evseev, A. N., Baranov, A. A., & Trubitsyn, A. P. (2008). Convection in the mantle with an endothermic phase transition. *Izvestiya, Physics of the Solid Earth*, *43*(12), 981–991. https://doi.org/10.1134/s1069351307120014

Turcotte, D. L., & Schubert, G. (2002). *Geodynamics*. 2nd Edition. Cambridge University Press. https://doi.org/10.1017/CBO9780511807442

Turcotte, D., & Schubert, G. (2014). *Geodynamics 3rd Edition*. Cambridge University Press. https://doi.org/10.1017/CBO9780511843877

van Hunen, J., & Allen, M. B. (2011). Continental collision and slab break-off: A comparison of 3-D numerical models with observations. *Earth and Planetary Science Letters*, *302*(1–2), 27–37. https://doi.org/10.1016/j.epsl.2010.11.035

Van Hunen, J., Van Den Berg, A. P., & Vlaar, N. J. (2002). The impact of the South-American plate motion and the Nazca Ridge subduction on the flat subduction below South Peru. *Geophysical Research Letters*, *29*(14), 2–5. https://doi.org/10.1029/2001GL014004

Weinberg, R. F., Becchio, R., Farias, P., Suzaño, N., & Sola, A. (2018). Early Paleozoic accretionary orogenies in NW Argentina: Growth of West Gondwana. *Earth-Science Reviews*, *187*(May), 219–247. https://doi.org/10.1016/j.earscirev.2018.10.001

Wolstencroft, M., & Davies, J. H. (2011). Influence of the Ringwoodite-Perovskite transition on mantle convection in spherical geometry as a function of Clapeyron slope and Rayleigh number. *Solid Earth*, *2*(2), 315–326. https://doi.org/10.5194/se-2-315-2011